Study of interplay between structure and flow in embedded-atom systems

vorgelegt von
Dipl.-Ing. Dipl.-Phys.
Igor Stanković

ii

Zusammenfassung

Wir benutzen ein einfaches Embedded-Atom-Potential, um das mechanische Verhalten, den Verschleiß und strukturelle Veränderungen an Grenzflächen von Modell-Metallen zu untersuchen. Die Embedded-Atom-Methode wird „EAM" bezeichnet, und hier verwendete generische Modell mit „GEAM". Die Zustandsgrößen realer Metalle - wie etwa Bindungsenergie, Elastizitätskonstanten und Lösungswärme - werden durch einige wenige Modellparameter wiedergegeben. Das Modellmetall wird mit Molekulardynamik-Computer-Simulationen (MD) untersucht und in Nichtgleichgewichts-Molekulardynamik-Computer-Simulationen (NEMD) einer Scherdeformation ausgesetzt. Voraussagen für mechanische und strukturelle Eigenschaften werden mit Resultaten für spezifische Metalle verglichen. Dieser Vergleich lässt Rückschlüsse über den Einfluss der Modellparameter auf die beobachtete Größen zu. Die Mechanismen, die zu mechanischer Legierung führen, werden beobachtet und diskutiert. Informationen über die Kristallstruktur innerhalb der NEMD-Konfigurationen erhalten wir mittels Durchführung einer Analyse der gemeinsamen Nachbarn, die auf ebenen Graphen basiert. Die Methode für nicht volumeneingeschränkte Metalle wird dahingehend verändert, dass mit ihr auch Strukturen in porösen Metallen untersucht werden können. Diese Veränderung besteht in einem kontrollierten Versatz zwischen allgemeiner Teilchenzahldichte und der bevorzugten Einbettungsdichte. Der Phasenübergang der EAM-Teilchen von einer homogenen Konfiguration zur porösen Struktur wird mithilfe von MD Simulationen nachvollzogen. Die zeitliche Entwicklung dieser Strukturen wird mithilfe von Schnappschüssen der Konfiguration sowie von Volumen- und Oberflächenanalysen untersucht. Die EAM-Strukturen werden benutzt, um die Diffusion eines Gases aus kurzreichweitig attraktiven bzw. repulsiven Teilchen in einem porösen Medium zu simulieren. Des weiteren präsentieren wir Simulationen zu Zeitentwicklung und Materialfluss von EAM-Teilchen in einer freistehenden Wand.

iv

Acknowledgments

I am deeply indebted to Prof. Dr. Siegfried Hess and PD Dr. Martin Kröger, who supervised this work and had the patience to let me explore the unknown. Without their support this thesis would have been very difficult to accomplish.

Thanks go to my colleagues Dr. Götz Rienäcker, Dr. Patrick Ilg, Dr. José Ginés Hernández Cifre, Gunnar Linke, Nana Sadowsky, Dr. Marco Ellero, and especially to Dr. Haiko Steuer for many helpful discussions, advices and hints. Several dear friends have helped me persevere through difficult times, especially Rajkov Family, Frederike and Holger Seibert, Nilufer Baba, Sanja Danilović, and Dirk Mitze.

Last but not least, my heartfelt appreciation goes to to my sister Ivana and parents Emilijan and Slavica Stanković. Without their consistent support, I could not have come this far.

Contents

Chapter 1

Introduction

Atoms in solids at room temperature are almost completely lacking mobility. Their thermal motion is reduced to the vibrations about an equilibrium position and individual atoms can move from their positions only with great difficulty. This gives solids their most characteristic property - they maintain shape they are given. Yet under strong shear forces even solids flow. In the present work, the flow behavior and the structural changes in metals are studied.

There are two main types of solids: *crystalline* and *amorphous*. The main characteristics of *crystalline* solids is existence of long range order: an ideal crystal is composed of atoms belonging to a basic cell identically positioned at a lattice defined by three fundamental translation vectors. In the case of a large single crystal, the lattice can extend over an enormous number of atoms and molecules. The choice of translation vectors and basic cell determines the type of crystal structure. The face centered cubic (fcc) structure is the common structure of most metals such as aluminium, nickel, copper, gold and silver and most of the inert gases. The hexagonal close packed (hcp) structure, as realized in cadmium and zinc, is very similar to the face centered cubic structure. Both structures have 12 nearest neighbors and a packing density of 74%. The difference between the two structures is the stacking order of the densely packed hexagonal layers. A slightly less densely packed crystal structure, is the body centered structure (bcc). The packing density in this structure is 68% and each atom has 8 nearest neighbors plus 6 almost nearest neighbors. The alkali metals, α-iron, and number of transition metals are examples for this structure. Further, there are tetragonally expanded types of these structures. Alloys and chemical elements with directed bonds build other types of crystal structures, such as diamond or simple cubic.

In metals valence electrons are not localized around nuclei. The dislocation of electrons from nuclei yields the strong decrease of kinetic energy and subsequently the increase of the binding energy in the metals. The interaction between atoms in metals is strong but depends little or not at all on the direction. Thus, metals tend to form one of the three above mentioned densely packed structures (fcc, bcc or hcp).

In the *amorphous* solids the atoms are ordered over a short length scales, i.e., over two to three interparticle distances, but there is no long-range order. The short-range order present in glasses is at the boundary between perfect order in crystals and total disorder in gases: the positions are neither fixed by some precise periodic rule, nor random as

in gases. Solids can also exist in the amorphous (glassy) state if they are quenched fast enough from the the liquid state or parts of the system can go through intermediate amorphous phase during transformation of the system during steady shear. In metallic glasses, the number of the nearest neighbors is around 12 and the nearest neighbor distance is similar to the case of densely packed structures (fcc and hcp). Even more interesting is the observation, that in average two neighboring atoms have five common neighbors. It is not possible to fill the three dimensional space with five-fold pattern without leaving gaps nor to form a periodic pattern. In the icosahedral (ico) structure the five fold symmetry is partially fulfilled, but the distances between atoms are not regular and it is not possible to propagate it in a periodic fashion.

Solid materials, crystalline or amorphous, deform when subjected to stress. Mechanical response of the system to a deformation is described by the elastic modulus and pressure (stress) tensors. If the applied deformation reaches a yield point, the material will not return in its original shape when relieving external forces. The plastic effects which give rise to a yield are due to the structural rearrangements. The extent of structural changes following yield will depend on the magnitude of deformation. For small and slow deformations the cooperative motion of atoms, by relative displacement of full layers, is expected. If a high steady shear rate is applied the system will undergo significant structural transformations.

1.1   Motivation

The dry sliding friction between atomically flat commensurate or incommensurate surfaces is a fundamental type of friction in tribology. When two unpolished solid surfaces touch or are pressed together with not too excessive forces, they actually touch only over a small fraction, typically 0.1% of the visible area of the contact. This load-bearing area consists of a number of asperities since microscopic roughness is unavoidable. The asperities are the spots, in which friction forces are thought to build up [1, 2, 3] and where everything of interest in dry solid friction and adhesive wear happens. Low energy electron diffraction experiments proved the existence of crystal structures at the sliding surfaces that are aligned with the shear direction in abraded material [4]. The observed structural changes, originated by large relative speeds in the surface layers – at a moderate overall speed – may propagate over several thousand crystal lattice constants [4, 5, 6, 7]. Thus, the frictional force – the shear stress integrated over the volume of the asperities – must be considered as inhomogeneous with respect to density, velocity, and temperature fields. An understanding of the physical mechanisms in the mentioned strong non-equilibrium situations is relevant for several phenomena including the processes inside the earth's crust [8], high velocity deformations, and breaking of metals at high velocities and impacts [9, 10]. Yet, a variety of processes taking place at friction surfaces (such as inhomogeneous plastic deformation of subsurface layer, phase transformations, material transfer, mechanical alloying, etc.) makes it difficult to develop a general approach for describing the microscopic structure, dynamics and wear in the course of rubbing [5, 11, 12, 13].

One of the important results of experiments and non-equilibrium molecular dynamics

(NEMD) studies on colloidal crystals is that polycrystalline samples become aligned when subjected to shear [14, 15], and two-dimensional hexagonal closed packed layers are formed – oriented to minimize resistance against flow. The sizes of the colloidal particles and their separations are of the order of microns, yielding elastic moduli 10^{12} times weaker when compared with those of the ordinary solids. Colloidal systems behave much like atomic matter, while exhibiting a range of phases, e.g., face centered cubic (fcc), base centered cubic (bcc) and fluid phases [16], but many body interactions, which play an important role in solids, are not considered in these studies. Also, phase transitions in solid part of the nonequilibrium phase diagram are assumed to exist in colloidal crystals [15, 16]. In metals, changes of temperature, pressure or density can trigger structural changes. *Ab initio* calculations of solid phases in transition metals [17, 18, 19] suggest that the observed high temperature bcc structure might be stabilized by a lattice vibrational entropy contribution to the free energy. Molecular dynamics simulations were recently used [20, 21, 22] to determine the vibrational entropy.

With atomic force microscopy (AFM) tribology has approached the friction in metals at the microscopic level [23, 24, 25, 26, 27], but AFM does not operate at the high speeds needed to investigate a strong flow regime which will be also investigated in this work. Also, AFM is restricted to very sharp tips. Along with its bulk properties, metals reveal still incompletely resolved surface phenomena, e.g., during dry solid friction, wear, and abrasion [5, 6, 7]. This explains the interest for numerical simulations of friction. Recent theoretical studies using atomistic models and molecular dynamics simulations have provided a better insight into friction on the nano-scale. Such studies offer detailed information about the influence of solid and fluid thin films on static friction, phonon dynamics and the transition from stick slip to smooth sliding [27, 28, 29, 30]. A rather complete picture about dynamical dissipation during slip-stick motion and the solid sliding regime emerged [26, 27, 31]. On the other hand, the relationship between material properties, long range elastic deformations, intermediate structure and material transfer at the interface between identical and different metals is less well understood [32].

The present study focuses on the effect of the choice of interfacial parameters on the microscopic dynamics and structure in order to characterize a simple embedded atoms model for metals, and to explore its range of applicability. To this end a stationary shear deformation between metals sliding past each other with large relative speeds is considered. This study is restricted to the study of metal-metal contacts, where the effect of the interfacial parameter is most transparent although the choice of parameters does not reflect any particular chosen "real" situation (we will come back to this point in Sec. 2.3). The results help to predict the microscopic behaviors when two blocks of metal with similar lattice constants but different structural and mechanical properties come in direct solid contact. The present study focuses on the role of dislocations, created under steady shear deformation, for the flow profile, local structure, and pressure tensor. It is thus complementary to recent large-scale simulations of nanocrystalline metals where for small strains (small time windows) the generation and dynamics of dislocations had been studied in detail, see Ref. [33, 34, 35, 36].

Recent work [37, 38, 39] on friction between a rolling wheel and a rail combines plastic deformation, friction, and heat generation effects with Hertzian calculations of stress

distribution. Two also recently developed grid-free computer simulation techniques, smooth particle applied mechanics [40, 41, 42] and dissipative particle dynamics [43], offer the potential for modelling metals on a micrometer scale ("mesoscale"). These methods allow us to study the impacts, high velocity deformations, formation of contact zones, and processes inside contact zones during dry friction of two metal blocks. However, they rely on expressions for thermomechanical properties of model metals as input. One of the goals of this work is to provide these expressions based on a generic, yet *ab initio* motivated model.

In this work it is further demonstrated that and how the proposed model for a bulk metal can be used to study metal sponges and porous metal structures. Metal sponges and foams show some potential for being produced with controlled spatial variations in their density [44, 45, 46, 47, 48, 49]. This suggests employing them as graded materials in space filling lightweight structures in analogy to cortical bone, a natural cellular material in space filling lightweight structures in analogy to cortical bone, a natural cellular materia that displays increased density in regions of high load [50]. Most mechanical and physical properties are affected by the size of the pores and at the same time by the thickness of the cell walls of metal foams. The past few years have seen increasing interest in porous metallic materials, especially in foams made of aluminium and aluminium alloys. The stimulus for this lies in recent process developments which promise materials with better quality and lower costs. The foam evolution is accompanied by a film rupture process which leads to coalescence of bubbles in the foam [51, 52]. Analogies between aqueous and metal foams are frequently made. Indeed, in both cases drainage leads to a steady removal of liquid from the foam walls even in microgravity experiments. The drainage leads to spontaneous rupture of films separating bubbles. Opposite to aqueous foams, in liquid metals there are no surfactants acting via electrostatic force to stabilize foam walls. Responsible for stability of metal foams are finely dispersed non-metallic particles in the melted metal. There were several attempts made until now to explain the mechanism of their action [51, 52].

The porous structures created with the proposed model are used to study the diffusion of gases of short range attractive and repulsive particles in confined geometries. The model for bulk metals introduced in this work, turns out also to be able to reproduce the structure of natural heterogeneous porous media. If there is a mismatch between overall number and from model desired density in initial configuration, the surface tension will try to reduce the surface of the sponge keeping at the same time the sponge walls connected. In this way, a set of sponges with continuously changing structural properties (surface, volume, connectivity) is created. The model porous structures introduced here, provide an ideal matrix to be filled with a gas, and to study, how transport and diffusion coefficients depend on the structure of porous materials. The prediction of effective transport properties of heterogeneous systems such as porous media is of considerable interest [53, 54, 55, 56, 57]. In many cases, classical theories of transport valid for homogeneous systems, do not apply if heterogeneities are strong and broad enough. The classical laws of transport, such as Fick's law of diffusion with a constant diffusion coefficient might not be valid in this case [57, 58]. Instead one needs time dependent transport coefficients. The studies of colloidal particle diffusion through

porous silica glasses provided an insight into a diffusion through heterogenous media. Still recent numerical studies of transport through porous media have been primely concerned with transport through highly idealized geometries (i.e., the fluids confined in slit, cylindrical and spherical pores). However, little attention has been given to studies of molecules and colloidal particle transport through complex microstructures such as silica gels, pore glasses, or in biological systems [57].

1.2   Outline of the thesis

This work is organized as follows:

Chapter 2 deals with the embedded-atom method [9, 59, 60, 61], adopted to model metals and used to investigate microscopic origins of the observed macroscopic behavior via non-equilibrium molecular dynamics computer simulations (NEMD). This method takes into account that the energy of atoms in metals depends on the local electron density, resulting in forces that are many body in character. Simulation provides us with the time-dependent positions and momenta of atoms in the system and thus allows for a detailed structure-pressure tensor relationship analysis (for example, by using planar graphs). A particularly simple choice of model, the "generic embedded-atom model" (GEAM), will be shown to reproduce the main zero-temperature constitutive properties of real metal by varying a set of basic model parameters. The model is characterized by a few parameters, the strength of the embedding function, the position of the minimum, and the cutoff radius of an interatomic binary potential, thus allowing for a systematic analysis of the influence of constitutive properties on the structure and mechanical behavior of metals. The parameters independently affect several constitutive properties (elastic coefficients, vacancy formation, and cohesive energy) such that the constitutive properties can be adjusted through analyzing corresponding properties of real metals. In particular, only the "quadratic term" in the embedding functional contributes to the components of elastic modulus tensor, which include response to volume changing deformation (i.e., C_{11} and C_{12}) since they depend on the second derivative of the cohesive energy.

Chapter 3 provides the details of implementation of the simulation method. The equations of motion are integrated with a velocity-Verlet algorithm. A cubic simulation box with constant volume and Lees-Edwards periodic boundary conditions are used to simulate shear deformation. The profile unbiased thermostat with rescaling of the velocities (which corresponds to Gaussian constraint) is used to control the temperature.

Chapter 4 introduces a method for obtaining information about the ideal and non-ideal local order existing in mono-atomic model solids or real materials from their atomistic configurations. An efficient algorithmic implementation is provided. The shape of the polyhedra formed by 'relevant' neighbors of each atom enter a pattern recognition method to resolve information about the type of the (usually non-ideal) crystal structure to which atoms surrounded by their relevant neighbors belong: hexagonal close-packed, face-centered cubic or body-centered cubic. Further, this approach allows the analysis of icosahedral structure which preferably occurs in amorphous solids. Results of a molecular dynamics computer simulation illustrate how this method can be applied to improve

the understanding of the mechanical and structural properties of solids i) undergoing a steady shear stress and ii) upon increasing temperature.

Chapter 5 presents simulations of the shear flow of the model metal within a single asperity, at a length scale where local properties, e.g., temperature and density of the macroscopic body can be considered gradient-free. For the case of sliding friction a contact zone at a relative motion in x direction, with a load and shear gradient in y direction is studied. The value of the penetration hardness is a good estimate for the typical pressure in the contact area, for the case of rough surfaces and moderate loads. The evolution of isotropic pressure is described, as well as the bulk and the shear moduli with temperature for different densities. A simple approximate expression for the isotropic pressure is obtained. The study reveals information about the feedback effects of temperature on shear stress and shear on structure, neither of which are included in the aforementioned work on rolling friction. The simulation allows to measure the influence of the initial crystal orientation on transient flow behaviors, the formation of shear bands and dislocations, and the general rate dependence of metal flow behavior in its viscoplastic (strong) flow regime. The dependence of the type of crystal structure on the temperature and density is observed. The semianalytic calculations of the phase diagram are presented. Further, the shear stress of the systems with fcc, bcc, and fluid (molten state) stationary configurations is studied and related with the effect of temperature on the structural behavior. A natural extension of GEAM is proposed and applied to characterize the microscopic structure, dynamics and wear at clean commensurate metal$_A$-metal$_A$ and metal$_A$-metal$_B$ sliding contacts (interfaces). The simulations, reveal that the dynamics of dislocations, crystalline domains, and related flow behaviors (stress tensor, shear moduli) are coupled. The rotation of crystal domains is detected as a source of the material mixing at the interface in early stages of sliding. In inhomogeneous metal interfaces the dependence of structural changes on model parameters is studied. A relation is established between shear moduli, effective shear rate and shear stress across the interface.

Chapter 6 investigates drainage and rupture in GEAM metal wall in an attempt to characterize effects of the material properties. The evolution of the model metal wall with time is described for different values of temperature, surface and cohesive energy. Also, the influence of the wall thickness and presence of the additional particles on the slowing of the wall rupture is explored. In this chapter it is further demonstrated that a modification of the embedded atom model can be used to create heterogenous porous structures (sponges) with continuously changing pore geometry. The modification concerns controlled mismatch between preferred global and local number density. The volume and surface of the GEAM porous structures are calculated by Monte Carlo integration. Further, the pores are filled with gases of short range attractive (SHRAT) and repulsive (SHREP) particles in order to study the diffusion. For SHRAT particles pore condensation which led to deviation from the Fick's law of diffusion is observed. The diffusion coefficient is found depending on both the pore's size and density of gas particles.

Chapter 2

The embedded-atom method

In this work, a model metal composed of N atoms is considered. Atoms are at thermal equilibrium at temperature T located at positions $\mathbf{r}^i$, $i = 1, 2, \ldots, N$ contained in a volume V. The potential is the sum of two contributions to the total potential energy E: a conventional binary interaction term through a two-body interaction potential $\mathcal{U}$ and a term stemming from an embedding functional $\mathcal{F}$, which models the effect of the electronic "glue" between atoms [59, 60, 61]:

$$E = \sum_{i=1}^{N}(\mathcal{F}(\rho_i) + \sum_{j>i}^{N}\mathcal{U}(r^{ij})), \qquad (2.1)$$

where r^{ij} denotes the norm of the relative vector $\mathbf{r}^{ij} = \mathbf{r_i} - \mathbf{r}_j$ between atoms i and j. The embedding functional $\mathcal{F}$ has to be a nonlinear function of the (local) embedding densities ρ_i of atoms $i = 1, .., N$. The local embedding density ρ_i is constructed from the radial coordinates of surrounding atoms and requires the choice of a weighting function $w(r)$,

$$\rho_i = \sum_{j \neq i} w(r^{ij}) + w(0). \qquad (2.2)$$

Here, $w(0)$ is the local embedding density of a solitary atom. The (effectively many-body) model potentials introduced above serve to model a variety of metal properties. The potential contributions to the pressure tensor and the elastic moduli can be obtained from the terms of first and second-order in the expansion of the configurational free energy with respect to the Lagrangian strain tensor $s_{\mu\nu}$, defined through particle displacement written as $r_\nu^i \rightarrow r_\nu^i + r_\mu^i s_{\mu\nu}$. The Greek subscripts μ, ν stand for Cartesian components associated with the x, y, z directions. This expansion is obtained from the standard expression for the configurational Helmholtz free energy $\beta F^{\mathrm{pot}} = -\ln \int \exp(-\beta E) \, d\mathbf{r}^N$ with $\beta \equiv 1/(k_{\mathrm{B}}T)$.

2.1   Pressure and elastic modulus tensors

The total pressure tensor is a sum of kinetic and potential contributions. The potential part of the pressure is evaluated as a N-particle average according to [62]:

$$V p_{\mu\nu}^{\text{pot}} = \langle \Phi_{\mu\nu} \rangle, \quad \Phi_{\mu\nu} = \sum_{i \neq j} \phi_{\mu\nu}^i(\mathbf{r}^{ij}). \tag{2.3}$$

The symbol $\sum_{i \neq j}$ denotes a double summation over pairs ij of (different) particles, the angular brackets indicate an ensemble or time average, and the second rank tensor ϕ^i ($i \in 1, \ldots, N$) is given by

$$\phi_{\mu\nu}^i(\mathbf{r}^{ij}) = r_\mu^{ij} \left(\frac{1}{2} \nabla_\nu \mathcal{U}(\mathbf{r}^{ij}) + \frac{\partial \mathcal{F}(\rho)}{\partial \rho} \Big|_i \nabla_\nu w(\mathbf{r}^{ij}) \right), \tag{2.4}$$

where $\nabla_\nu w(\mathbf{r}) = r^{-1} r_\nu \, \partial w(r)/\partial r$ as for any function with spherical symmetry, i.e., when $w(\mathbf{r}) = w(r)$.

The kinetic part of the pressure p^{kin} is obtained from peculiar velocity of particles, $\mathbf{c}^i = \dot{\mathbf{r}}^i - \mathbf{v}(\mathbf{r}^i)$, where $\mathbf{v}(\mathbf{r}^i)$ denotes the (macroscopic) flow velocity on position of particle i,

$$V p_{\mu\nu}^{\text{kin}} = \left\langle \sum_i m c_\mu^i c_\nu^i \right\rangle. \tag{2.5}$$

The scalar (isotropic) pressure p^{iso} is the trace of the total pressure tensor divided by the spatial dimension, $p^{\text{iso}} = p_{\mu\mu}/3$. The symmetric traceless part of $p_{\mu\nu}$ is associated with the shear stress and normal stress differences. The antisymmetric part of the pressure tensor vanishes for structure-less particles with spherical interaction.

The response of the material to deformation $s_{\mu\nu}$ is characterized by the elastic modulus tensor $G_{\lambda\kappa,\mu\nu}$, defined by linear relation $\sigma_{\lambda\kappa} = G_{\lambda\kappa,\mu\nu} s_{\mu\nu}$, where $\sigma_{\lambda\kappa} = -(p_{\lambda\kappa}^{\text{pot,def}} - p_{\lambda\kappa}^{\text{pot,0}})$ is the negative difference between the potential contribution to the pressure tensor in the deformed state $p_{\lambda\kappa}^{\text{pot,def}}$ and its corresponding value $p_{\lambda\kappa}^{\text{pot,0}}$ in the undeformed state. The elastic modulus tensor can be decomposed into Born-Green and fluctuation contributions, $G_{\lambda\kappa,\mu\nu} = G_{\lambda\kappa,\mu\nu}^{\text{BG}} + G_{\lambda\kappa,\mu\nu}^{\text{flct}}$ [62, 63], with

$$V G_{\lambda\kappa,\mu\nu}^{\text{BG}} = \left\langle \sum_{i \neq j} \phi_{\lambda\kappa,\mu\nu}^i(\mathbf{r}^{ij}) \right\rangle_0 + \frac{1}{3} \langle \Phi_{\mu\mu} \rangle_0 \delta_{\lambda\kappa} \delta_{\mu\nu}, \tag{2.6}$$

$$V G_{\lambda\kappa,\mu\nu}^{\text{flct}} = -\beta[\langle \Phi_{\lambda\kappa} \Phi_{\mu\nu} \rangle_0 - \langle \Phi_{\lambda\kappa} \rangle_0 \langle \Phi_{\mu\nu} \rangle_0]. \tag{2.7}$$

In Eq. (2.6) the abbreviation is used, $\phi_{\lambda\kappa,\mu\nu}^i(\mathbf{r}) = r_\lambda \nabla_\kappa \phi_{\mu\nu}^i(\mathbf{r})$. The subscript "0" in $\langle \cdots \rangle_0$ indicates a configurational average to be evaluated in the unstrained state. Later, these expressions are evaluated for ideal fcc and bcc lattices. In the conventional "Voigt notation" the four indices (range 1-3) are replaced by two indices (range 1-6). In this notation one denotes elastic moduli of cubic crystals and of the model with central interactions: $C_{11} \equiv G_{xx,xx}$, $C_{12} \equiv G_{xx,yy}$, and $C_{44} \equiv G_{xy,xy}$. The conventional symmetrization according to $C_{44} \equiv (G_{yx,yx} + G_{yx,xy} + G_{xy,yx} + G_{xy,xy})/4$ is not essential in this case. In this work, the axes x, y, z correspond to the directions [100], [010], [001]

in the cubic crystal, i.e., to the deformation direction, its gradient direction and the direction normal to the shear deformation plane, respectively. In systems with cubic symmetry, spatial anisotropy is reflected by the existence of a minimum and a maximum of the shear modulus. The modulus C_{44} is associated with a displacement in the [100] direction and a (010) shear plane in a cubic crystal. This modulus stands for a maximum resistance the system with fcc or bcc structure can offer to shear. The same systems, with a displacement applied along the [1$\bar{1}$0] direction and the (111) shear plane of the crystal, have minimum shear modulus associated with the modulus $\widetilde{C}_{44} = (C_{11} - C_{12})/2$. For an isotropic system, C_{44} equals the orientationally averaged shear modulus G. As a component of the elastic modulus tensor, the shear modulus can be written as a sum of a Born-Green (usually positive) and a fluctuation (usually negative) contribution, $G = G^{\mathrm{BG}} + G^{\mathrm{flct}}$. The Born-Green contribution is written as a linear combination of the extremal contributions to the shear modulus, precisely,

$$G^{\mathrm{BG}} \equiv \frac{3C_{44} + 2\widetilde{C}_{44}}{5}. \qquad (2.8)$$

The fluctuation contribution to the average shear modulus becomes

$$VG^{\mathrm{flct}} = -\frac{\beta}{10}[6\langle\Phi_{xy}^2\rangle_0 + \langle(\Phi_{xx} - \Phi_{yy})^2\rangle_0]. \qquad (2.9)$$

The response to a volume changing deformation of an isotropic solid can be inferred from the (isothermal) bulk modulus or compression modulus $B \equiv n(\partial p^{\mathrm{iso,pot}}/\partial n)_T$, where $n = N/V$ is number density. The Born-Green components of the bulk and shear moduli are related in cubic crystals [64, 65] via a modified Cauchy relation valid for the embedded-atom method of the form Eq.(2.1) through

$$B^{\mathrm{BG}} = \frac{5}{3}G^{\mathrm{BG}} + 2p^{\mathrm{pot}} + \frac{1}{9V}\left\langle \sum_i \frac{\partial^2 \mathcal{F}}{\partial \rho^2}\Big|_i \left(\sum_{j \neq i} r^{ij}\frac{\partial w}{\partial r}\Big|_{ij}\right)^2 \right\rangle_0. \qquad (2.10)$$

The fluctuation contribution to the bulk modulus is

$$VB^{\mathrm{flct}} = -\frac{\beta}{9}\left[\langle\Phi_{\mu\mu}\Phi_{\mu\mu}\rangle_0 - \langle\Phi_{\mu\mu}\rangle_0^2\right], \qquad (2.11)$$

and the total bulk modulus is $B = B^{\mathrm{BG}} + B^{\mathrm{flct}}$.

2.2 The "GEAM" model potentials

For the binary potential function $\mathcal{U}$ a radially symmetric short ranged attractive (SHRAT) potential is used [66]:

$$\mathcal{U}(r) = \phi_0 r_0^{-4}\left[3(r_{\mathrm{cut}} - r)^4 - 4(r_{\mathrm{cut}} - r_{\mathrm{min}})(r_{\mathrm{cut}} - r)^3\right], \qquad (2.12)$$

for $r \leq r_{\mathrm{cut}}$, and $\mathcal{U}(r) = 0$ otherwise, with an energy scale ϕ_0, a length scale r_0, an interaction range r_{min}, and a cutoff radius r_{cut}. The well depth of the two-particle (binary

interaction) potential $\mathcal{U}$ is $-\mathcal{U}(r_{\min}) = \phi_0 r_0^{-4}(r_{\text{cut}} - r_{\min})^4$. This format of the potential has been recently used as the effective two-particle interaction in the embedded-atom model metal [67, 68], and to model thermophysical properties of fluids and solids [66]. The SHRAT potential has a finite value at $r = 0$, i.e., $\mathcal{U}(0) = \phi_0 r_0^{-4} r_{\text{cut}}^3 (4r_{\min} - r_{\text{cut}})$. For temperatures below $0.1\phi_0/k_{\text{B}}$ – due to the Boltzmann factor $\exp[-\mathcal{U}(0)/k_{\text{B}}T]$ – the fraction of particles that reach zero distance is smaller than 10^{-51} for the choice $r_{\text{cut}} = 1.6\,r_0$, $r_{\min} = 2^{1/6}r_0$. The normalized Lucy's weight function in the definition of the embedding density is chosen for reasons discussed in Ref. [67], i.e.,

$$w(r) = w_0 \left(1 + 3\,\frac{r}{r_{\text{cut}}} \right) \left(1 - \frac{r}{r_{\text{cut}}} \right)^3, \tag{2.13}$$

for $r \leq r_{\text{cut}}$, and $w = 0$ otherwise, with a prefactor obtained by normalizing the weight function, $w_0 = w(0) = 105/(16\pi r_{\text{cut}}^3)$. The embedding potential in polynomial form is

$$\mathcal{F}(\rho) = \phi_0 \sum_{k=2,4,\ldots} F_k \left((\rho - \rho_{\text{des}})^k - (w_0 - \rho_{\text{des}})^k \right) r_0^{3k}, \tag{2.14}$$

where ρ_{des} is the desired embedding number density and F_k are embedding strengths, being part of the model. Odd terms in the sum are excluded since their contribution would be always repulsive in nature, the linear term ($k = 1$) could be adsorbed in a modified pair potential $\mathcal{U}$. The desired density in this model equals roughly $\rho_{\text{des}} = r_0^{-3}$ the embedding density and particle number density $n \equiv N/V = r_0^{-3}$. Polynomial format of embedding functional is computationally less expensive than standard logarithmic form [9, 59, 60]. Also, the ratio between cohesive energy E_{coh} (or energy per particle) and B can be systematically changed without influence on values of other constitutive properties, see Table 2.1. In following section (Sec. 2.2.1) a property of polynomial format, to give simple analytical expressions for many constitutive properties, will be used to explain origins of well know properties of embedded-atom potential [60].

A generic embedded-atom model metal is investigated, with a minimum of the binary potential located at the distance $r = r_{\min} = 2^{1/6}\,r_0 \approx 1.12\,r_0$ as for the Lennard-Jones potential, with a cutoff distance $r_{\text{cut}} = 1.6\,r_0$, and $F_2 = 1$, and $F_k = 0$ for $k > 2$. The hereby specified metal will be denoted as GEAM. For GEAM, the well depth of the two-particle potential $\mathcal{U}$ is therefore $-\mathcal{U}(r_{\min}) \approx 0.05\,\phi_0$. Model parameters for Cu, Ni, Ag, Au, Fe, and the GEAM model metal are given in Table 2.1; parameters for the real metals are obtained by linear optimization using experimental data (ratios of the constitutive properties) also given in the table.

Metal	F_2	F_4	r_{cut}	$\frac{r_{\min}}{2^{1/6}}$	n	E_{coh}	B	G	$\frac{nE_{\text{coh}}}{B}$	$\frac{E_{\text{v1}}}{E_{\text{coh}}}$	$\frac{G}{B}$	A
Cu					85.9nm^{-3}	3.50eV	142GPa	59.3GPa	0.339	0.366	0.418	3.19
(fcc)	0.42	0.	1.010	1.00	0.997	0.419	2.889	1.158	0.145	0.897	0.401	3.35
	0.42	8.5	1.010	1.00	0.997	0.972	2.909	1.158	0.333	0.412	0.398	3.35
Ni					84.6nm^{-3}	4.45eV	183GPa	94.3GPa	0.329	0.360	0.513	2.45
(fcc)	0.2	0.	1.017	1.02	0.957	0.366	2.408	1.202	0.145	1.034	0.499	2.95
	0.2	6.5	1.017	1.02	0.957	0.839	2.468	1.203	0.325	0.838	0.487	2.96
Ag					58.0nm^{-3}	2.95eV	101GPa	33.5GPa	0.271	0.373	0.331	2.88
(fcc)	0.7	0.	1.006	1.00	0.994	0.486	3.609	1.214	0.134	0.793	0.336	2.85
	0.7	8.	1.006	1.00	0.994	0.982	3.621	1.214	0.270	0.415	0.335	2.85
Au					58.1nm^{-3}	3.81eV	174GPa	30.7GPa	0.204	0.236	0.177	2.85
(fcc)	1.3	0.	0.988	0.94	1.052	0.281	4.890	0.842	0.125	0.514	0.172	2.92
	1.3	10.2	0.988	0.94	1.052	1.083	5.562	0.841	0.204	0.295	0.151	2.83
Fe					84.6nm^{-3}	4.29eV	169GPa	86.8GPa	0.344	0.417	0.515	2.70
(bcc)	0.2	0.	1.17	1.08	0.868	0.417	1.572	0.772	0.252	1.091	0.491	2.97
	0.2	1.1	1.17	1.08	0.868	0.417	1.667	0.768	0.342	0.724	0.491	2.97
GEAM					72.0nm^{-3}	1.91eV	179GPa	52.7GPa				
(fcc)	1.0	0.	1.00	1.00	0.993	0.552	4.442	1.309	0.123	0.718	0.295	2.34

Table 2.1: The values of constitutive properties and their ratios for Cu, Ni, Ag, Au, Fe, and the model metal GEAM (ρ_{des}, F_2 are equal to unity and all other parameters are zero). The top values are experimental data from Refs. [69, 70, 71, 72], and the two lower values are calculated for input parameters in the first four columns. The model parameters for the metals are obtained by linear optimization of ratios of constitutive properties using experimental data.

2.2.1   Basic properties

For a system made of particles occupying ideal lattice sites (or any other configuration) the cohesive energy, or energy per particle, $E_c = E/N$ is calculated from Eq. (2.1). The resulting curves are displayed in Fig. 2.1 for GEAM with ($F_2 = 1$) and also without ($F_2 = 0$) the embedding contribution. The dependence of energy per particle from density is presented, the dashed curves show results for particles placed on body centered cubic lattice (bcc) sites and solid curves show results for particles placed on face centered cubic lattice (fcc) sites.
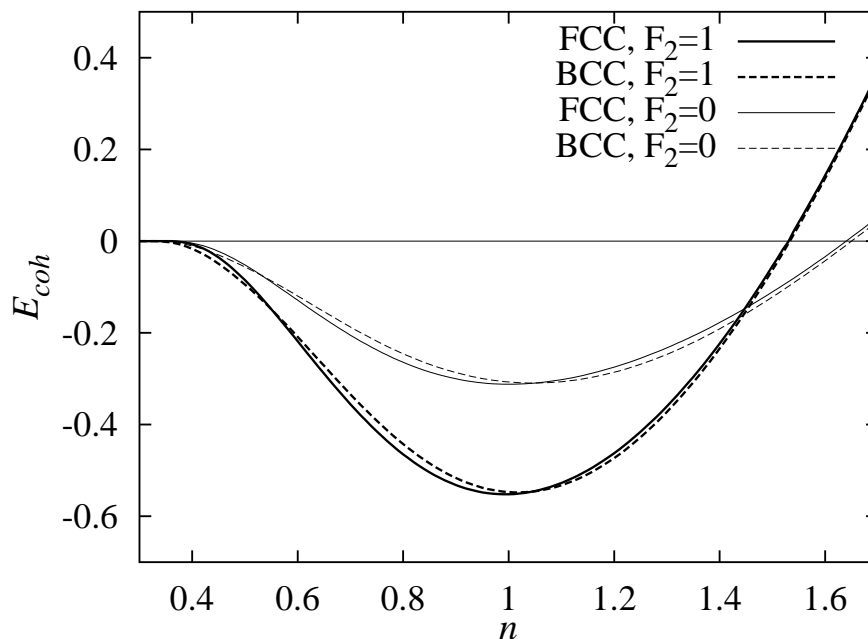

Figure 2.1: Cohesive energy or energy per particle vs density (both in LJ units) at $r_{\text{cut}} = 1.6r_0, r_{min} = 2^{1/6}r_0$ (generic embedded-atom model GEAM) for ideal fcc and bcc lattices with ($F_2 = 1$) and also without ($F_2 = 0$) the embedding functional.

The variation of this energy subject to a uniaxial volume conserving deformation referred to as Bain deformation [17, 73], parameterized by the ratio $a_{[100]}/a_{[010]}$ between sides of a conventional bcc cubic cell [74], is presented in Fig. 2.2. Under Bain transformation the system transforms from a bcc structure $a_{[100]}/a_{[010]} = 1$ into an fcc structure at $a_{[100]}/a_{[010]} \approx 1.414$. Both fcc and bcc structures correspond to local minima of the cohesive energy with respect to this ratio. During Bain transformation the bcc structure contracts along [010] and [001] directions by $\approx -11\%$ and expands along the [100] direction by about 21%, so that these axes transform to [01$\bar{1}$], [011], and [100] axes of the fcc structure. Burgers [75] suggested a mechanism for the bcc to hcp transformation that can be also applied to the transformation of bcc into fcc structure. For this transformation mechanism the original bcc structure is deformed along the [01$\bar{1}$], [011], and [100] directions for $\approx 9\%$, 3%, and -11%, respectively, and subsequently sheared (with $\gamma = 1/3$) in shear direction [01$\bar{1}$]/gradient direction [011], see Fig. 2.3. Unexpected at first glance, the energy barrier between fcc and bcc structures is similar for both structure transformation mechanisms, cf. Figs. 2.2 and 2.3. Yet the Bain deformation

induces a relative shift of layers of atoms in the crystal, similar to the shear in the Burgers mechanism and therefore the degrees involved in transformation of structure are very similar for these two mechanisms, as further discussed in [76].
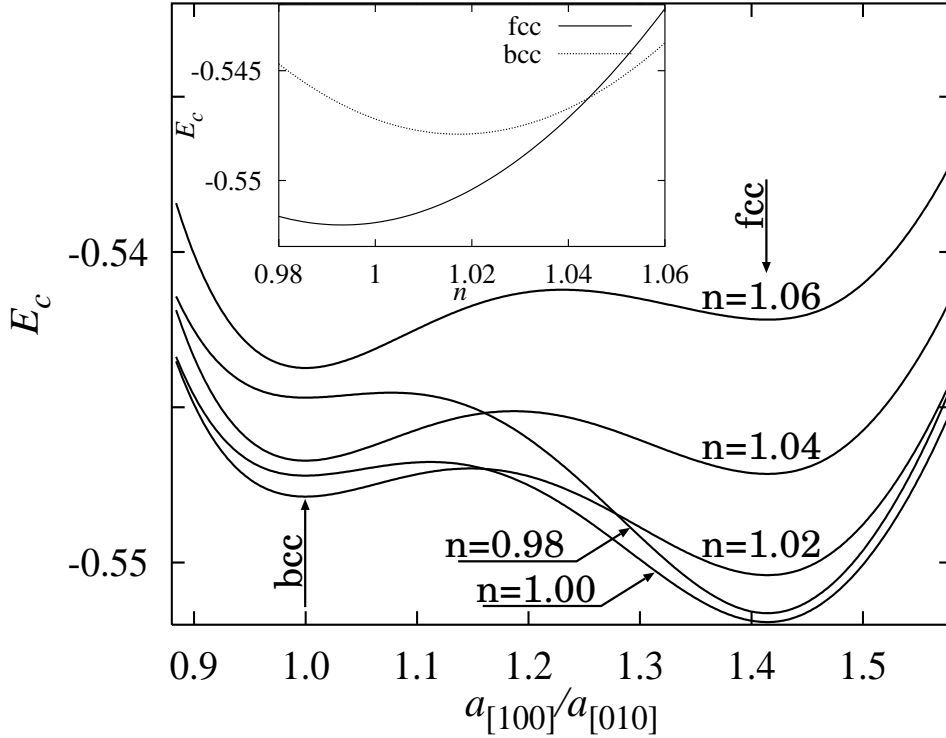

Figure 2.2: Cohesive energy vs. ratio $a_{[100]}/a_{[010]}$ during volume conserving tetragonal Bain transformation. The transformation of the ideal GEAM metal lattice is presented for global number densities $n = 0.98, \ldots, 1.06$. The bcc structure occurs at $a_{[100]}/a_{[010]} \approx 1$ and the fcc at $a_{[100]}/a_{[010]} = 1.414$. The insert shows the effect of density n on the cohesive energy for ideal fcc and bcc structures. All quantities are given in dimensionless reduced units, cf. Sec. 2.3 and Tab. 2.2.

For GEAM, both fcc and hcp structures are ground state structures, i.e., structures with minimum energy per particle for $n^{1/3}r_{\mathrm{cut}} < 1.83$. This results in a zero stacking fault energy γ_{sf} and energy difference between fcc and hcp structure. For this reason, one might expect pronounced defects – stacking faults and twins – in a GEAM metal under shear 'flow', i.e., shear deformation at constant deformation rate. This need not to be the case in the strong flow regime: (i) Stacking fault is created when two semi-infinite blocks of fcc crystal are sheared on (111) plane along a $[1\bar{1}0]$ direction. Along this path, the system has to first pass through an energy barrier referred here as the unstable stacking fault energy γ_{usf}. The stacking fault results in the formation of a hcp plane inside the fcc structure. Recent studies suggest that the dislocation activity is not determined by the value of the stacking fault energy alone. The difference between stacking fault energy and unstable stacking fault energy $|\gamma_{\mathrm{usf}} - \gamma_{\mathrm{sf}}|$ has been included into the description [33, 34, 35, 78]. For the case of GEAM, the difference $|\gamma_{\mathrm{usf}} - \gamma_{\mathrm{sf}}|$ is comparable in magnitude with the value observed in metals with low γ_{sf} values, see Tab. 2.2. (ii) In the strong shear flow regime the thermal energy of the particles is comparable, but smaller than the magnitude of the potential barrier γ_{usf}. Therefore,
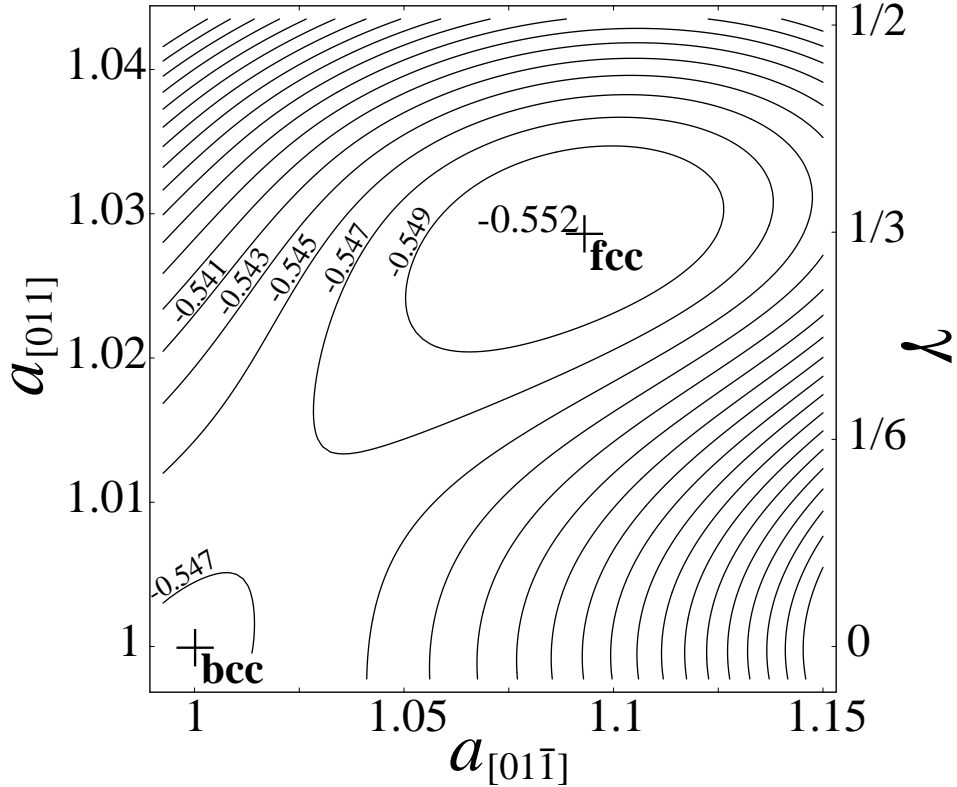
Figure 2.3: Cohesive energy contours in the vicinity of the Burgers transformation path. The system is simultaneously deformed ($a_{[011]}$) in [011] direction and sheared by an amount γ along the [01$\bar{1}$] direction/gradient direction [011]. For a Burgers transformation [75] the original bcc structure is transformed into the fcc structure after being deformed by $\approx 9\%$, 3%, and -11% along the [01$\bar{1}$], [011], and [100] directions, respectively, and subsequently sheared with $\gamma = 1/3$.

atoms in fcc single crystals subjected to strong shear deformation easily slide into their nearest potential minima, creating stacking faults.

For densities close to $n = r_0^{-1/3}$ (or $n = 1$ in reduced units, cf. Sec. 2.3) the minimum energy is lower in fcc solids. In order to describe the influence of model parameters on some constitutive properties of ideal fcc and bcc structures a state point with vanishing (total) isotropic pressure, $p^{\text{iso}} = P_{\mu\mu}/3$, and fix the binary potential well depth to the above GEAM value is considered. The shape of the binary potential is controlled by changing the values r_{min} and r_{cut}. The size of r_{cut} changes the strength of contributions to the embedding density. Smaller r_{cut} means smaller contribution of neighbors, $\sum_{i \neq j} w(r^{ij})$, in Eq. (2.2). The corresponding parameter in other embedded-atom models, cf. Refs. [60, 61], is the nearest neighbor equilibrium distance.

Parameter dependence of constitutive properties

The pressure and the elastic modulus tensor is to be obtained using the virial expressions in Eq. 2.3-2.6 from analytical calculations and also from nonequilibrium molecular dynamics (NEMD), by which the GEAM model is solved numerically (cf. Sec. 3). In the following, elastic coefficients, pressure tensor and related quantities are evaluated from the expressions given in the preceding section in the limit of low temperatures, where particles occupy ideal lattice sites.

The cohesive energy E_{coh} depends strongly on the embedding part of the model potential, see Fig. 2.4(a) and 2.4(b) for a quantitative analysis. The main contribution of the two-particle interaction to E_{coh} stems form the first neighbors. At zero-pressure, the first neighbors are near the minimum of the binary potential; the resulting density depends only on the position of the minimum of the potential [Fig. 2.4(d)]. Since the well depth of the two-particle potential is held constant, the cohesive energy does not depend on the position of the potential minimum. The vacancy formation energy E_{1v} is the minimum energy needed to move an atom from the bulk onto the surface of the crystal [9, 60], see Fig. 2.9(a). In order to perform a systematic analysis of E_{1v} parameter dependence, relaxation of structure around vacancy is not considered. The dominant contribution in EAM to the unrelaxed vacancy formation energy stems from the binary interaction potential. The unrelaxed vacancy formation energy depends weakly on the embedding part of the potential and the position of the cutoff radius, cf. Table 2.1. It depends indirectly – through zero-pressure density – on the position of the potential minimum. The vacancy formation energy depends loosely on the embedding part of the potential and the position of the cutoff radius, cf. Fig. 2.1 and 2.5(a). This enables us to fit experimental values for the cohesive energy and vacancy formation energy independently by varying the strengths of the embedding term $F_2, F_4, \ldots$. Compared to other constitutive properties of EAM metals, the vacancy formation energy changes slowly with change of all model parameters.

The surface energy is determined by dividing the total energy increase in separating bulk material on the crystallographic plane [Fig. 2.9(b)] by the total new surface area created [60]. For case of the GEAM ($r_{min} = 2^{1/6}$, $r_{cut} = 1.6$, $F_2 = 1$, and $F_k = 0$ for $k > 2$), the unrelaxed surface energies for three low index planes are

$$\Gamma_{111,fcc} = 0.083, \ \Gamma_{100,fcc} = 0.101, \ \Gamma_{110,fcc} = 0.109 \tag{2.15}$$

and

$$\Gamma_{100,bcc} = 0.113. \tag{2.16}$$

The order from lowest to highest surface energy is for (111), (100), (110) planes as expected for fcc structure. Plane (110) in fcc structure transforms under volume conserving Bain transformation into (100) plane of bcc structure; thus values of these two surface energies are close. Note in Fig. 2.4(a) and Fig. 2.5(b) that surface energy depends stronger on strength of the first therm in embedding functional F_2 while cohesive energy depends stronger on higher order terms ($F_4, F_6, \ldots$). Other ground state defect energies of the model metal, e.g., the surface formation energy, can be also calculated from Eq. (2.1).
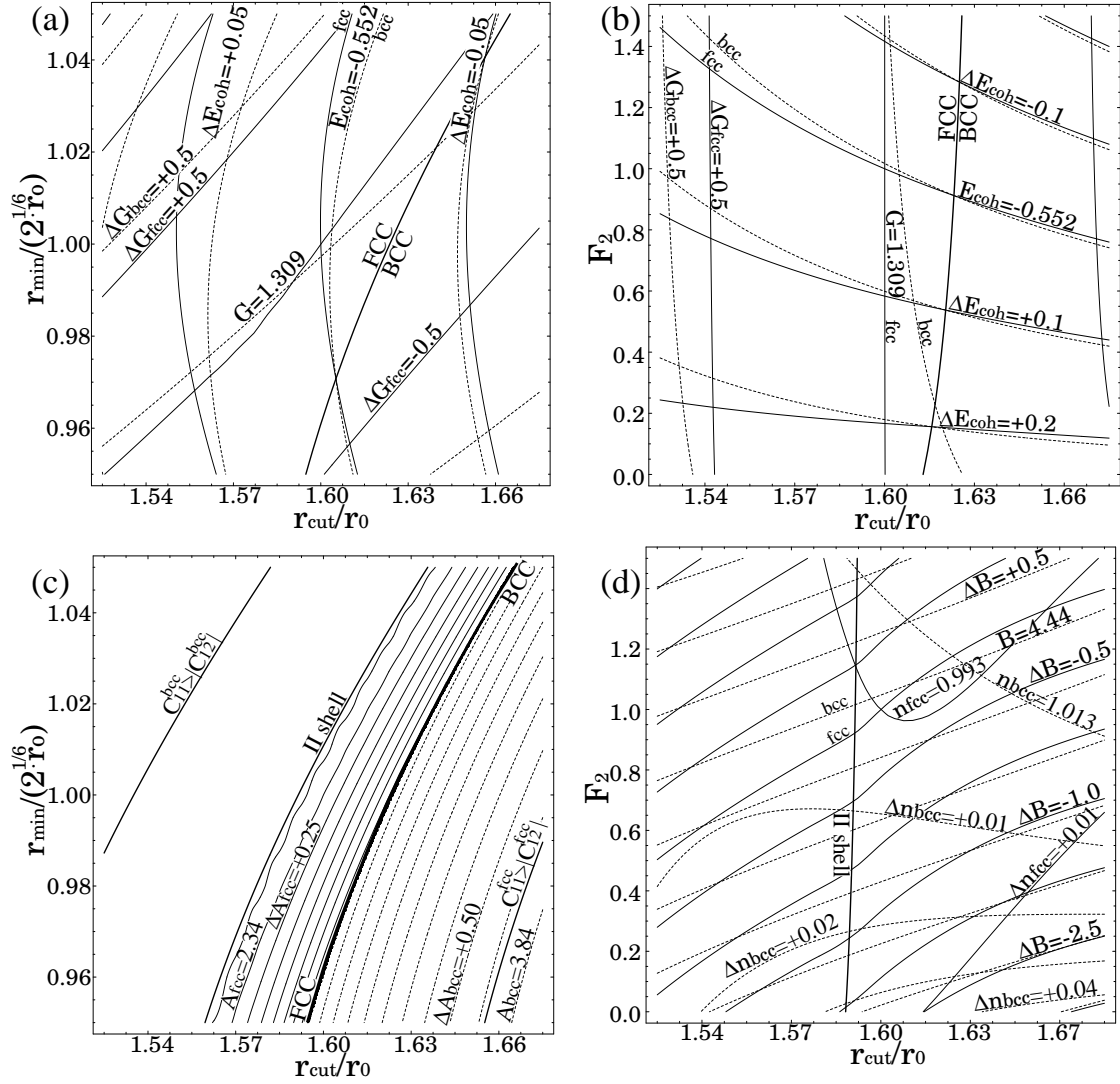
Figure 2.4: Cohesive energy E_{coh}, shear G and bulk B moduli, anisotropy ratio A, and density n for the case of vanishing pressure tensor. All quantities are in standard LJ units. Values for fcc (solid curves) and bcc (dashed curves) structure are presented. (a) Effect of cutoff radius r_{cut}, position of the potential minimum r_{min} for $F_2 = 1$ (GEAM). (b) Effect of cutoff radius r_{cut} and embedding strength F_2 for $r_{min} = 2^{1/6}r_0$ (GEAM) (c) Effect of r_{cut}, r_{min} ($F_2 = 1$) on the anisotropy ratio A. Areas (bold line) where fcc and bcc structures are energetically favored are also shown. For cubic structures one has $A = 2$ if interactions with the first nearest neighbor shell only are present; "II shell" denotes the separation line. The line $C_{11} > |C_{12}|$ separates the regimes where bcc and fcc structures are mechanically unstable. (d) Effect of r_{cut}, F_2 (for $r_{min} = 2^{1/6}r_0$) on the bulk modulus B and zero-pressure density n.

Recent studies, Refs. [79, 80], indicate that there is no straightforward comparison between vacancy formation and surface formation energies calculated with EAM and experimental data. Difference between electronic structure at a surface level and in bulk is not considered by EAM, thus EAM should give in case of metal with high electronic
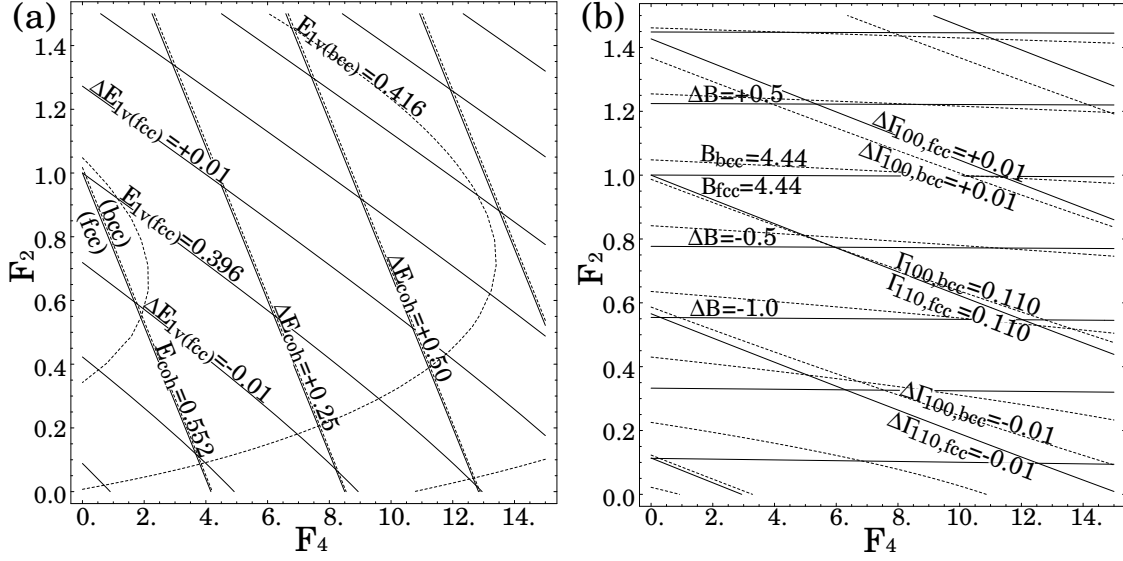
Figure 2.5: Vacancy formation energy E_{v1} and cohesive energy E_{coh} for the case of vanishing pressure tensor. All quantities are in standard LJ units. Values for fcc (solid curves) and bcc (dashed curves) structure are presented. (a) Effect of embedding strength term components F_2, F_4 for $r_{min} = 2^{1/6}$, $r_{cut} = 1.6$ and $F_k = 0$ for $k > 2$ (GEAM). (b) Effect of F_2, F_4 ($r_{min} = 2^{1/6}, r_{cut} = 1.6$ and $F_k = 0$ for $k > 4$) on the bulk modulus B and surface energies in fcc $\Gamma_{110,fcc}$ and bcc $\Gamma_{100,bcc}$ structure.

density (Pt,Pd) noticeably lower vacancy formation energies from experiment.

The elastic coefficients – bulk modulus B, (average) shear modulus G, C_{44}, and the Cauchy pressure $\widetilde{C}_{44} = (C_{11} - C_{12})/2$ depend on the second derivative of the free energy for a nearest neighbor model, cf. Eq. (2.6). The second-order term [$k = 2$, Eq. (2.14)] in the embedding functional is most important for the values of the elasticity coefficients which include response of material on volume changes (B, C_{11}, C_{12}) since the embedding density is usually very close to the desired embedding density, see Fig. 2.4(d). Shear moduli, C_{44} and $\widetilde{C}_{44}$ in cubic crystals include only response to volume conserving shear deformation that do not change embedding density and consequently contribution of embedding functional to free energy. For this reason shear moduli depend only on two-body interaction parameters (r_{cut}, r_{min}), see Fig. 2.4(a) and 2.4(b). The same conclusion can be obtained from symmetry analysis of Eq. (2.6) for cubic crystals. This enables us to fit experimental values for the shear moduli G and bulk moduli B independently by varying strength of F_2 term. Other order terms of embedding functional may be considered to obtain an improved quantitative agreement between model behaviors and experimentally observed behaviors, in particular with respect to the ratios between elastic coefficients and the cohesive energy, cf. Table 2.1. Due to Eq. (2.10), the difference between bulk and shear modulus is approximately

$$(3B - 5G) \approx \frac{nF_2}{3} \Big(\sum_{j \neq i} r^{ij} \frac{\partial w}{\partial r} |_{ij} \Big)^2 \tag{2.17}$$

near the zero-pressure density in an ideal cubic crystal. The ratio $G/B \leq 3/5$ decreases with increasing second-order term in the embedding functional.
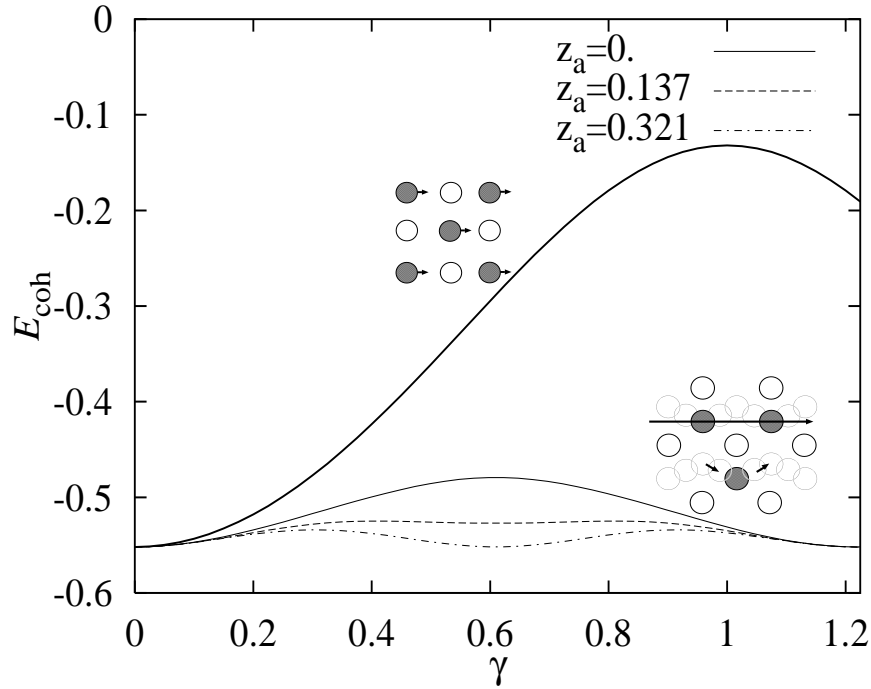
Figure 2.6: Shearing of the ideal fcc crystal in the limit of low temperatures. The change of the cohesive energy (E_{coh}) with the increasing shear deformation (γ) is presented for shear direction [100]/gradient direction [010] (thick curves, upper insert) and shear direction [$1\bar{1}0$]/gradient direction [111] (thin curves, lower insert). In the latter case, sinusoidal trajectories with amplitude $z_a = 0$, 0.137, and 0.321 in vorticity direction [$22\bar{1}$] and possessing a wave length equivalent with the distance between two successive potential minima are assumed.

The so-called "anisotropy ratio" $A = C_{44}/\widetilde{C}_{44}$ of a cubic material is the ratio of the extremal values of the shear modulus, maximum C_{44} and minimum Cauchy pressure $\widetilde{C}_{44}$. It depends on the shape of weighting function and the two-particle potential. It does not depend on the embedding strength (F_2). The anisotropy ratio is $A = 2$ in cubic crystals, when only interactions with nearest neighbors are present, according to Cauchy relations. In bcc structure the Cauchy pressure falls with increasing cutoff radius and the anisotropy ratio rises. If the Cauchy pressure becomes negative, the system is mechanically unstable for zero applied stress, see Fig. 2.4(c). For the mechanical stability analysis in case of non-zero stresses one should use modified stability criteria, see Ref. [81]. Even when disregarding the higher order terms, the embedded-atom potential Eq.(2.14), predicts well the anisotropy ratios of both fcc and bcc metals. Higher order terms ($F_4, F_6, \ldots$) can be considered to obtain a quantitatively improved description (Table 2.1) predominantly concerning the cohesive energy. Other constitutive properties stay mostly unchanged upon considering these higher order terms.
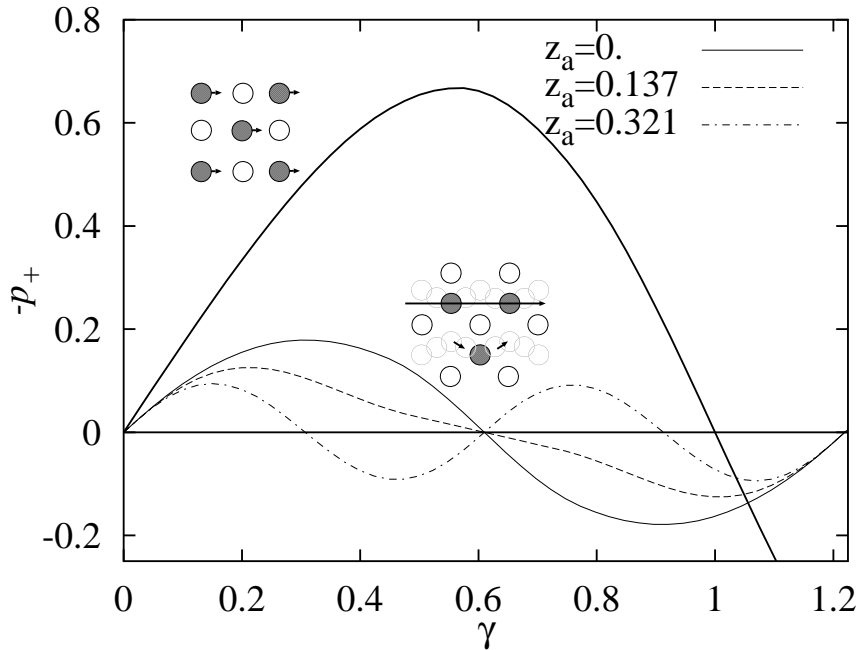
Figure 2.7: Shear stress $(-p_+)$ vs. shear deformation (γ) for shear direction [100]/gradient direction [010] (ticker curve, upper insert) and shear direction [1$\bar{1}$0]/gradient direction [111] (thinner curves, lower insert). In the latter case, particles follow sinusoidal trajectories with amplitude z_a in vorticity direction [22$\bar{1}$] and a wave length equivalent to the distance between two potential minima. At $\gamma = 0$ particles occupy ideal fcc lattice sites.

Shear deformation in the limit of low temperatures

The symmetric traceless (anisotropic) pressure tensor has 5 independent components. In the special case of simple shear flow with velocity in x-direction and velocity gradient in y-direction only 3 independent components have to be considered (as long as symmetry is not broken in an average sense). Let us denote them conveniently as $p_{+,-,0}$, where $p_+ \equiv (P_{yx} + P_{xy})/2$ corresponds to a shear pressure, two normal pressure differences are $p_- \equiv (P_{xx} - P_{yy})/2$, and $p_0 \equiv (2P_{zz} - (P_{xx} + P_{yy}))/4$, respectively. The scalar (isotropic) pressure p^{iso} is the trace of the total pressure tensor divided by the spatial dimension, $p^{\text{iso}} = P_{\mu\mu}/3$. Note that the 'stress tensor' is identical with the pressure tensor except for its sign, i.e., $-p_+$ is the shear stress.

First, the changes of pressure tensor components and the cohesive energy are calculated in the limit of low temperatures in two cases: (i) shear direction [100]/gradient direction [010] and (ii) shear direction [1$\bar{1}$0]/gradient direction [111]. In the former case the distance between the two minima corresponds to a shear deformation $\gamma = 2$, in the latter case the same distance corresponds to $\gamma = \sqrt{3/2}$. In the undeformed state $(\gamma = 0)$ particles occupy ideal lattice sites, i.e., are located in a position of minimum potential energy. The cohesive energy E_c increases with shear deformation until an unstable equilibrium is reached, cf. Fig. 2.6. The corresponding shear stresses are given in Fig. 2.7. A system with bcc or fcc structure produces maximum shear stress and
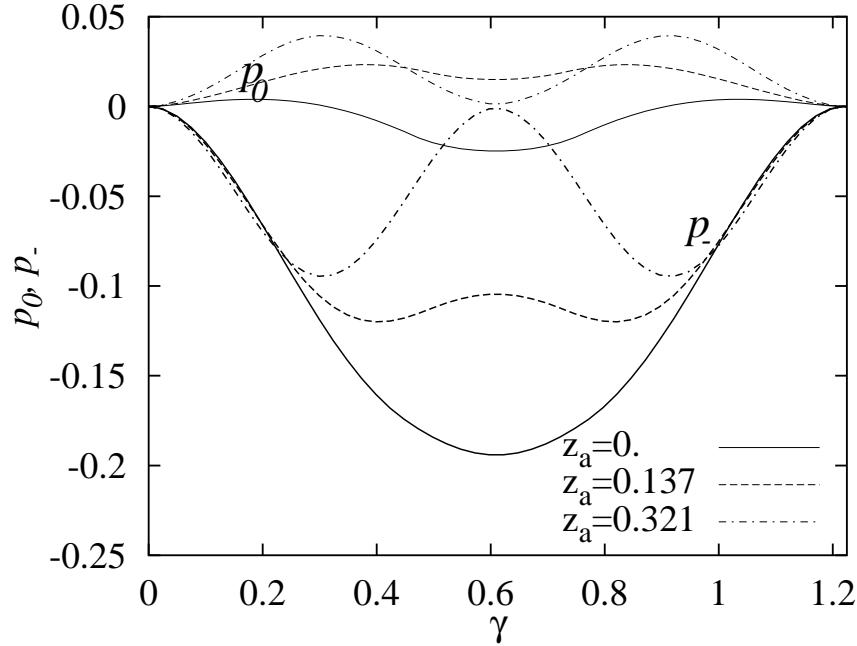
Figure 2.8: Normal pressure differences p_- (ticker curves) and p_0 (thinner curves) vs. shear deformation (γ) for shear direction $[1\bar{1}0]$/gradient direction $[111]$ in the low-temperature limit, cf. Sec. 5.6.1. Particles follow sinusoidal trajectories with amplitudes $z_a = 0.$, 0.137, and 0.321 in vorticity direction $[22\bar{1}]$ and a wave length equivalent to the distance between two potential minima. Prior to the onset of shear particles occupy ideal fcc lattice sites.

maximum resistance to shear in shear direction $[100]$/gradient direction $[010]$, where particles have to cross the highest potential barrier. The fcc system, when sheared along the $[1\bar{1}0]$ direction/gradient direction $[111]$ of the crystal, has minimal resistance. Particles are then stacked within densely packed hexagonal layers corresponding to the (111) plane of the fcc crystal structure. The shear stress and the height of the potential barrier are further reduced through collective zig-zag movements of hexagonal layers within the plane, see Fig. 2.7.

2.2.2   Characteristics of doped GEAM

In order to study interactions between two (or more) metal species in contact, the standard equations of embedded-atom model are adapted, Eqs. (2.1) and (2.2):

$$E = \sum_{i=1}^{N}(\mathcal{F}(\rho_i) + \sum_{j>i}^{N} e_{ij}\,\mathcal{U}(r^{ij})), \tag{2.18}$$

$$\rho_i = \sum_{j\neq i}^{N} w_{ij}\,w(r^{ij}) + w(0), \tag{2.19}$$

the coefficients e_{ij} and w_{ij} are introduced to model the properties at the interface between two (or more) metal species in contact. They allow to specify the strength of
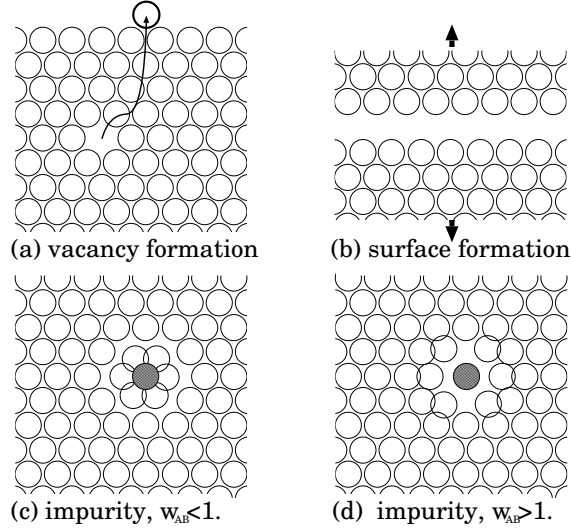
(a) vacancy formation   (b) surface formation

(c) impurity, $w_{AB} < 1$.   (d) impurity, $w_{AB} > 1$.

Figure 2.9: Vacancy is crated when an atom is moved from the bulk onto the surface of the crystal (a). Surface formation energy is defined as total energy increase in separating bulk material on the crystallographic plane per surface unit (b). To calculate approximately heat of solution in limit of low temperatures, an atom from the bulk material is replaced with impurity, relaxation of the crystal structure around impurity is partially included with adjusting of the distance to the next neighbors so that (total) isotropic pressure vanishes. Local density around impurity increases for $w_{AB} < 1$ (c), and decreases in case $w_{AB} > 1$ (d).

interaction between atoms belonging to the same and to different materials. Since throughout the work is death with two metals (type A and B) in contact, the coefficients e_{ij} can take one of the three values e_{AA}, e_{BB}, or $e_{AB} = e_{BA}$, depending on the species to which atoms i and j belong (either A or B). By default, and if not otherwise mentioned, all interaction strength parameters are set to unity. Thus, the default is a (bulk) system without marked interface.

The heat of solution ΔE for a host bulk material of type A and an inclusion of type B is defined as the change of the total system's energy when an atom of the host material A is replaced by an impurity atom of type B. To estimate the effect of model parameters on the heat of solution in an approximate fashion, this quantity is calculated in the limit of low temperatures using the following procedure: an atom from the bulk is replaced by an impurity; the radial distance to its next neighbors is adjusted so that the (total) isotropic pressure vanishes; the heat of solution is calculated as the difference between total energies between start- and final configurations. For metals with similar crystal lattice constants, within focus of this work (see Tab. 2.2 and Ref. [61]), the true amount of relaxation is small. For that reason also corrections to the approximate values calculated here must be small. Resulting curves are displayed in Fig. 2.10, where the effect of the strengths e_{AB} and w_{AB} on the heat of solution is presented. For $e_{AB} = e_{AA} = 1$, and $w_{AB} = w_{AA} = 1$ there is no difference between impurity and material, thus ΔE vanishes in that limit. The heat of solution increases linearly with e_{AB} as the binary interaction potential does. From Fig. 2.11 one can observe that the density corresponding to zero pressure increases with e_{AB} as a result of the mismatch between zero pressure densities
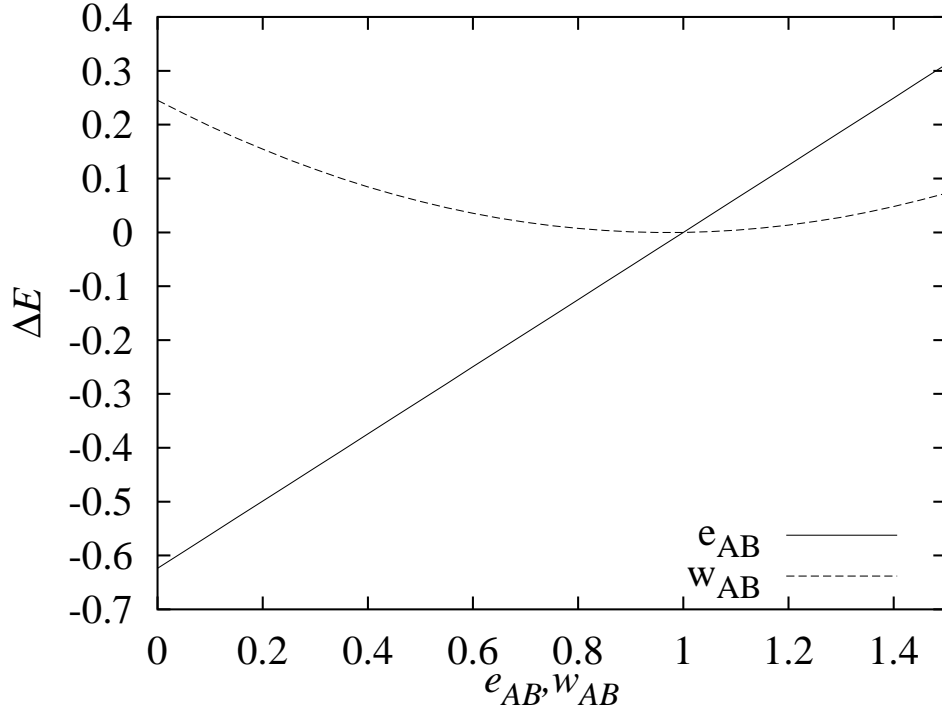
Figure 2.10: Alloy heats of solution for a single substitutional impurities in fcc crystal lattice for different e_{AB} and w_{AB} in reduced units.
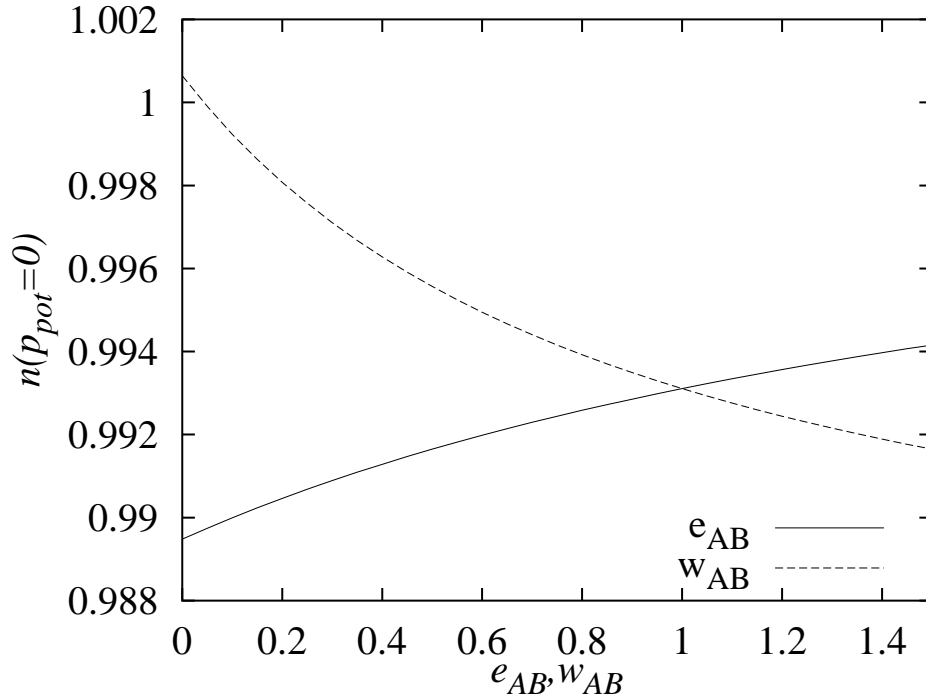
Figure 2.11: Zero-pressure number density n=N/V for a single substitutional impurities in fcc crystal lattice for different e_{AB} and w_{AB}. All quantities are given in reduced units.

for systems interacting solely via binary and embedding interactions, respectively. The size of w_{AB} influences the value of the embedding density (ρ) at the impurity location in such a way that it is decreasing with decreasing w_{AB}. As result, the number density (n)

metal	a_0 [nm]	n [nm^{-3}]	E_{coh} [eV]	B [GPa]	G [GPa]	γ_{sf} [eV/nm^2]	γ_{usf}	ΔE [eV]	(host-impurity)
Cu	0.362	85.9	3.50	142	59.3	0.4	1.25	0.03	(Cu-Ni)
Ni	0.352	84.6	4.45	183	94.3	1.14	1.48	0.11	(Ni-Cu)
Ag	0.409	58.0	2.95	101	33.5	0.11	0.58	-0.19	(Ag-Au)
Au	0.408	58.5	3.81	174	30.7	0.23	0.69	-0.16	(Au-Ag)
Pd	0.389	68.0	3.91	195	54.3	1.06	1.95	-0.04	(Pd-Pt)
Pt	0.392	66.4	5.77	283	65.1	1.68	2.45	-0.21	(Pt-Pd)
GEAM	0.271	72.5	1.91	179	52.7	0	1.00		(dimensional)
	1.12	0.993	0.552	4.442	1.309	0	0.021		(adimensional)

Table 2.2: Experimental values [69, 70, 71, 72, 82] for Cu, Ni, Ag, Au, Pd, and Pt: lattice constant a_0, particle number density n, energy per particle (cohesive energy) E_{coh}, bulk B and shear G moduli, along with heats of solution ΔE for given host-impurity pairs. The stacking fault energy γ_{sf} and unstable stacking fault energy γ_{sf} are obtained with tight-binding and first-principles calculations in Refs. [77, 78]. For GEAM metal constitutive properties are given in both in "real" (dimensional), and reduced (adimensional) units (bottom row).

around an impurity increases with increasing difference $|w_{\mathrm{AB}} - w_{\mathrm{AA}}|$ in order to achieve the desired vanishing isotropic pressure, cf. Fig. 2.11. The heat of solution increases with the absolute distance $|w_{\mathrm{AB}} - w_{\mathrm{AA}}|$ due to the parabolic form of the embedding functional, see Fig. 2.11. For the reasons described in Sec. 2.2.1, the shear moduli (G, C_{44}, $\widetilde{C}_{44}$) scale with the two body interaction parameters e_{AA} and e_{BB} linearly, i.e., in case of average shear modulus one has $G(e_X) = e_X G(e_X = 1.)$ for $X \in \{\mathrm{AA}, \mathrm{BB}\}$.

2.3 Reference values

To compare nonequilibrium molecular dynamics (NEMD) simulation results with experimental data, constitutive properties of present model are related to experimental data for real metals in Table 2.1. The last four columns of this table give the characteristic ratios of constitutive properties for four fcc metals (Cu,Ni,Ag,Au) and one bcc metal Fe, together with the same ratios for corresponding model metals obtained by linear optimization of model parameters; values for GEAM are also listed. The reference values for dimensionless model quantities Q_{dimless} can be computed from experimental (top number) and calculated values listed in middle section of Table 2.1. The determined model parameters and reference values are not unique in the sense that it is possible to find similar sets which would as well resemble the properties of real materials. In following, reference values used to translate between dimensionless simulation quantities and experimental values, will be discuss shortly. Any measurable quantity Q with a dimension $[Q]$ specified in SI units kg, m, and s is made dimensionless by a reference quantity

$$Q_{\mathrm{ref}} = m^{\alpha+\gamma/2} r_0^{\beta+\gamma} \phi_0^{-\gamma/2} \quad \text{for } [Q] = \mathrm{kg}^\alpha \mathrm{m}^\beta \mathrm{s}^\gamma, \qquad (2.20)$$

such that $Q = Q_{\mathrm{dimless}} Q_{\mathrm{ref}}$; quantities m, r_0, and ϕ_0 provide the scales via the interaction potential Eq. (2.12) and the equations of motion. The reference values for length r, number density n, energy $k_{\mathrm{B}} T$ (and defect energies), temperature T, time t, shear rate $\dot{\gamma}$, pressure P, and the elastic moduli in terms of the simulation parameters are therefore $r_{\mathrm{ref}} = r_0$, $n_{\mathrm{ref}} = r_0^{-3}$, $e_{\mathrm{b,ref}} = \phi_0 = k_B T_{\mathrm{ref}}$, $t_{\mathrm{ref}} = r_0 \left(m/e_{\mathrm{b,ref}} \right)^{1/2}$, $\dot{\gamma}_{\mathrm{ref}} = t_{\mathrm{ref}}^{-1}$, and $P_{\mathrm{ref}} = \phi_0 r_0^{-3} = n_{\mathrm{ref}} e_{\mathrm{b,ref}}$. For Cu, e.g., one obtains reference values $\phi_0 = 3.61 eV$ and $P_{\mathrm{ref}} \equiv 38\,\mathrm{GPa}$, $r_0 = 2.26$ Å and $n_{\mathrm{ref}} = 86.2\,\mathrm{nm}^{-3}$ from Table 2.1. Atomic mass of copper is $m_{\mathrm{Cu}} = 1.06 \times 10^{-25}\,\mathrm{kg}$ and the reference time is estimated as $t_{\mathrm{ref}} = 0.97 \times 10^{-13}\,\mathrm{s}$. By choosing $T_{\mathrm{ref}} = \phi_0/k_B = 40$ kK, $P_{\mathrm{ref}} = 40$ GPa one obtains $\phi_0 = 3.45$ eV, $n_{\mathrm{ref}} = 72.5$ nm^{-3} and $r_0 = 2.4$ Å for GEAM. For $0.8 < e_{AB} < 1.2$ and $0.4 < e_{AB} < 1.5$ the alloy heats of solution of GEAM metal are within the range expected for real metals, cf. Table 2.2. Atomic masses of most metals are within the range $m = (0.8 - 3.5) \times 10^{-25}$ kg, thus an estimated reference time for GEAM metal is in range $0.9 - 2.0 \times 10^{-13}$ s.

The predicted values of the vacancy formation energy, elastic anisotropy and the bulk modulus are within the expected ranges for fcc and bcc metals. Since both density and vacancy formation energy depend strongly on the position of the potential minimum, there is no unique way to choose model parameters such that both density and vacancy formation energy precisely match values for a given real metal, cf. Table 2.1 and Figs. 2.4(a) and 2.4(b) for possible choices.

Chapter 3

Simulation method

The equations of motion in the conducted NEMD simulation are integrated by a velocity-Verlet algorithm. A cubic simulation box with constant volume and Lees-Edwards periodic boundary conditions are used to simulate shear deformation. The components of force acting on particle i, directly obtained from Eq. (2.1), read

$$F_\nu^i = -\sum_{j \neq i} \left(\nabla_\nu \mathcal{U}(\mathbf{r})\Big|_{ij} + \Big(\frac{\partial \mathcal{F}(\rho)}{\partial \rho}\Big|_i + \frac{\partial \mathcal{F}(\rho)}{\partial \rho}\Big|_j \Big) \nabla_\nu w(\mathbf{r})\Big|_{ij} \right). \qquad (3.1)$$

The Greek subscript ν stands for Cartesian components associated with the x, y, z directions.

A suitable integration time step is $\triangle t / t_{\text{ref}} = 0.01$ for the chosen range of temperatures and densities. The temperature is kept constant by rescaling the magnitudes of the peculiar particle velocities which corresponds to a Gaussian constraint of constant kinetic energy in the limit $\triangle t \to 0$.

For the case of a model metal under steady shear deformation (or flow), a relative motion of periodic images in the flow (x) direction is performed, with a shear gradient in y direction. The flow simulation introduces the shear rate $\dot{\gamma}$, given by $\dot{\gamma} = \partial v_x / \partial y$, as a further independent variable. While a linear flow profile is observed at moderate rates, at higher shear rates and during the transition towards a steady state, parts of system to move as blocks. To allow simulations of plug-like flow it is essential to use a "profile unbiased thermostat" (PUT, Refs. [83, 84]) which calculates the mean streaming (peculiar) velocities self-consistently. Alternatively, shear flow can also be generated by modifying the equations of motion with a Sllod algorithm [85, 86].

The simple model metal is explicitly determined by the set of model potentials and solved without approximations with computational effort of order N.

3.1 The Verlet algorithm

For numerical solving of the equations of motion exist a large number of algorithms with computational speed and precision. In molecular dynamics, the most commonly used time integration algorithm is probably the so-called Verlet algorithm [87, 88]. The basic idea is to write two third-order Taylor expansions for the positions , one forward and

one backward in time. For position vector of the particle i, $\mathbf{r}_i$, and its time-derivatives, one has

$$\mathbf{r}_i(t + \Delta t) = \mathbf{r}_i(t) + \frac{\partial \mathbf{r}_i}{\partial t}\Big|_t \Delta t + \frac{1}{2}\frac{\partial^2 \mathbf{r}_i}{\partial t^2}\Big|_t \Delta t^2 + \frac{1}{6}\frac{\partial^3 \mathbf{r}_i}{\partial t^3}\Big|_t \Delta t^3 + O(\Delta t^4) \qquad (3.2)$$

and

$$\mathbf{r}_i(t - \Delta t) = \mathbf{r}_i(t) - \frac{\partial \mathbf{r}_i}{\partial t}\Big|_t \Delta t + \frac{1}{2}\frac{\partial^2 \mathbf{r}_i}{\partial t^2}\Big|_t \Delta t^2 - \frac{1}{6}\frac{\partial^3 \mathbf{r}_i}{\partial t^3}\Big|_t \Delta t^3 + O(\Delta t^4). \qquad (3.3)$$

Adding the expressions (3.2) and (3.3) gives

$$\mathbf{r}_i(t + \Delta t) = 2\mathbf{r}_i(t) - \mathbf{r}_i(t - \Delta t) + \frac{\partial^2 \mathbf{r}_i}{\partial t^2}\Big|_t \Delta t^2 + O(\Delta t^4). \qquad (3.4)$$

This is the basic form of the Verlet algorithm. Since Newton's equations are integrated, acceleration (second derivative of position in time) is just the force (Eq. 3.1) divided by the mass:

$$\frac{\partial^2 \mathbf{r}_i}{\partial t^2} = \frac{1}{m}\mathbf{F}_i. \qquad (3.5)$$

As one can immediately see, the truncation error of the algorithm when evolving the system by Δt is of the order of Δt^4, even if third derivatives do not appear explicitly. This algorithm is at the same time simple to implement, accurate and stable. It is exactly reversible in time and, given conservative forces, conserves linear momentum. A problem with this version of the Verlet algorithm is that velocities are not directly generated, while they are not needed for the time evolution. Still in order to calculate kinetic energy (sometimes important test, if MD simulation is runs correctly) and for temperature control in NEMD simulations it is necessary to have the information about velocities in the system. One could calculate velocities from position vectors, however, the error in that case would be of order Δt^2 rather than Δt^4.

To obtain more accurate values of velocities, they have to be stored in memory. Modifications of Verlet algorithm give exactly the same trajectory like the basic algorithm, but store different variables (coordinates, velocities, accelerations) in the memory at different times. One of improved implementations of the Verlet algorithm is the so-called velocity Verlet algorithm [87], where positions, velocities and accelerations at time $t + \Delta t$ are obtained from the same quantities at time t in the following way:

$$\mathbf{v}_i(t + \frac{\Delta t}{2}) = \mathbf{v}_i(t) + \frac{1}{2}\mathbf{a}_i(t)\Delta t, \qquad (3.6)$$

$$\mathbf{r}_i(t + \Delta t) = \mathbf{r}_i(t) + \mathbf{v}_i(t + \frac{1}{2}\Delta t)\Delta t, \qquad (3.7)$$

$$\mathbf{a}_i(t + \Delta t) = \frac{1}{m}\mathbf{F}_i, \qquad (3.8)$$

$$\mathbf{v}_i(t + \Delta t) = \mathbf{v}_i(t + \frac{\Delta t}{2}) + \frac{1}{2}\mathbf{a}_i(t + \Delta t)\Delta t \qquad (3.9)$$

where $\mathbf{v}$ stands for velocity and $\mathbf{a}$ for acceleration. Note that 9N memory locations are needed to save the 3N positions, velocities and accelerations, but different quantities are never simultaneously stored or called from memory.
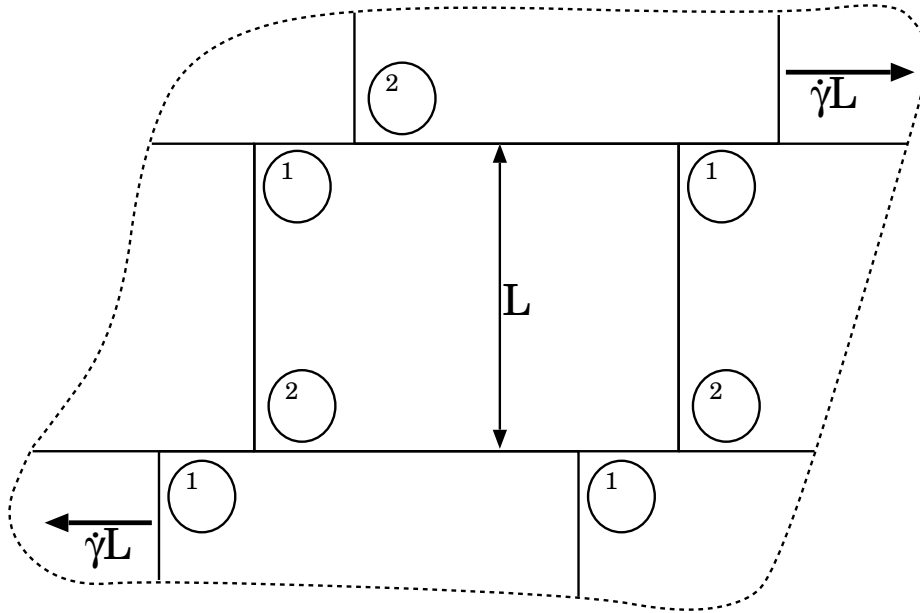
Figure 3.1: Lees-Edwards boundary conditions for homogenous shear flow.

3.2 Lees-Edwards periodic boundary conditions

In order to simulate bulk properties of the solids periodic boundary conditions are used. In periodic boundary conditions, the cubic (simulation) cell is copied throughout space to form a lattice. Particles interact with the closest image particle according to *minimum image convention.* The minimum image convention gives through cut-off radius r_{cut} of the potential minimal dimension of the simulation cell; if L_x, L_y, L_z are three dimensions of the cubic cell, the condition is $L_x, L_y, L_z > 2r_{cut}$. Choice of the dimensions of the simulation cell is usually determined by the characteristic correlation length of the studied system; dimensions of the simulation cell should be larger then characteristic correlation length of the system. Crystalline systems due to their periodicity have very long correlation lengths, and strictly taking, one should use very large systems with several crystal grains inside. However, smaller cubic cells that can be efficiently calculated on currently available computers, sill can be used. One should take care that crystal structure inside simulation cell continues periodicly in the images and in shear systems, the system should be sufficiently large to accommodate shear-induced structure (system tends to form integer number of crystal unit cells between two boundaries).

From very beginning simulations were used for studding shear properties of the materials. One of the common techniques was proposed by Lees and Edwards [89]. The in this thesis infinite periodic system is subjected to shear in xz plane. The simulation box and its images in the same xz plane (images between $-L_y/2$ and $L_y/2$) are stationary. The image cells in layer above $L_y/2$ are moving in positive x direction with speed $\dot{\gamma}L_y$ and image cells under $-L_y/2$ with speed $-\dot{\gamma}L_y$ (Fig. 3.1).

The Lees-Edwards periodic boundary conditions can be used alone to set up a steady linearly velocity profile, with gradient $\dot{\gamma}$. However, in a driven system heat is generated and the total energy of the system is not anymore constant. A mechanism which allows homogeneous removal of the heat will be discussed in the next chapter.

3.3   Profile unbiased thermostat with velocity scaling

In equilibrium MD simulation equations of motion of particles are integrated numerically to reproduce the particle trajectories (see 3.1). The number of particles, shape of cell and total energy can be easily fixed on begin of the simulation and held latter constant. Therefore, macroscopic quantities can be obtained in molecular dynamics simulation at a constant (E, V, N) condition; where E stands for total energy of the system, V volume and N number of particles. This corresponds to mico-canonical ensemble, where temperature T is related to kinetic energy averaged in time

$$\Big\langle \sum_i \frac{\mathbf{p}_i^2}{2m_i} \Big\rangle = \frac{3}{2} NkT. \tag{3.10}$$

where $\mathbf{p}_i$ is momentum and m_i mass of particle. However, the temperature becomes known first after simulation is carried out and simulations cannot be carried at exactly defined temperature.

In experiments temperature is usually one of the input parameters. The properties of system at constant temperature are studied in the canonical ensemble. Studied system is surrounded by a very large external system, heath bath, with constant temperature T. Change of temperature in heath bath because of exchange of heat with the studied system is assumed to be neglectful. The exchange of heath is only interaction between system and surrounding heath bath. The temperature inside of the system is kept constant through interaction with heath bath. In contrast to micro-canonical ensemble total energy fluctuates and one can obtain canonical distribution [90]:

$$f_c(\mathbf{r}, \mathbf{p}) = \frac{e^{-H(\mathbf{r}, \mathbf{p})}}{\int e^{-H(\mathbf{r}, \mathbf{p})} d\mathbf{r} d\mathbf{p}}. \tag{3.11}$$

The interaction between heath bath and the system is very complex and cannot be studied in detail. There exists variety of methods for control of temperature, the main difference between these methods arises from the way how the interaction between heat bath and studied system is modelled. One way is to impose a constrain on the velocities in the equation of motion

$$\sum_i \frac{\mathbf{p}_i^2}{2m_i} - \frac{3}{2} kT = 0. \tag{3.12}$$

By inserting this condition into Liouville equation [90, 91] one obtains

$$f_c(\mathbf{r}, \mathbf{p}) = \delta\Big(\sum_i \frac{\mathbf{p}_i^2}{2m_i} - \frac{3}{2} NkT \Big) e^{-\mathcal{U}(\mathbf{r}, \mathbf{p})}. \tag{3.13}$$

The distribution in space has canonical form but distribution of momenta is δ function because of the imposed constrain in Eq. (3.12). In this way, the exact canonical ensemble average is obtained in simulations only for those quantities which are functions of coordinates.

The first attempt to carry out a simulation in controlled conditions was velocity scaling algorithm proposed by Woodcock [92]. It was shown that it yields canonical distribution (see Ref. [93]), if after each integration step, velocities are scaled to satisfy the constant kinetic energy condition. The procedure is very fast and simple.

In order to study planar Couette flows (along x-axis, with gradient in y direction) a modification to kinetic temperature is introduced

$$\frac{m}{2} \sum_i [\dot{\mathbf{r}}_i - \mathbf{v}(\mathbf{r}_i)]^2 = \frac{3}{2} NkT \tag{3.14}$$

where $\mathbf{v}(\mathbf{r}_i)$ is mean streaming (peculiar) velocity at position $\mathbf{r}_i$. Deviations from the mean streaming velocity are interpreted here as thermal fluctuations and suppressed by thermostat. In systems with planar Couette a linear velocity profile can be assumed for peculiar velocities $\mathbf{v}(\mathbf{r}_i) = \dot{\gamma} y_i \mathbf{e}_{\mathrm{x}}$ [94]. In this way constructed temperature control is profile biased, and it will suppress other possible forms of flow, such as, plug like or two phase flow.

Profile unbiased thermostat (PUT) [83, 84, 95, 96] first calculates average streaming velocities in discrete layers, by averaging over the velocities of the particles in the layers. The average streaming velocities inside of layers are used in Eq. (3.14) for evaluation of temperature. Two criteria for the choice of the thickness of the layers should be met:

- the layer thickness Δ should be small compared with lengthscale given by the velocity gradient and temperature: $(\dot{\gamma}\Delta)^2 \ll k_{\mathrm{B}} T/m$;

- the number of particles in each layer should be large enough to give a reasonable statistics.

In this work both, thermostats with the linear velocity profile and profile unbiased thermostat, are used. The differences are observed only in intermediate regime, after yield stress is reached and before steady shear flow is reached. As it was expected, profile biased thermostat suppresses plug like flow of two blocks separated with melted model metal at higher shear rates. Also gradual rearrangement of the system at lower shear is visible only with profile unbiased thermostat (see Section 5.4). Steady shear flow was reached faster in case of profile biased thermostat, in intermediate state system is melted and no significant amount of periodic crystal structure is observed.

3.4 Calculation details

The values of the shear stress components are obtained from NEMD simulations by extracting their averages once the system has reached the stationary state. This corresponds to the statistical average typically over a period $\triangle t/t_{\mathrm{ref}} = 800$ in system of 2000 particles, the configurations are sampled after every 10 time units. The temperature was increased stepwise every $\triangle t/t_{\mathrm{ref}} = 2000$. The results for pressure tensor components for a number of parameters are compared with data extracted from NEMD simulations of larger systems (N=43200) and runs $\triangle t/t_{\mathrm{ref}} = 4000$ to test convergence to steady state.

The stick-slip motion is observed only in intermediate state and it is not observed after first 1000 time units of the simulation. System size effects on total energy, pressure tensor components, and their fluctuations are not observed. Yield stress and frequency of defects formed in steady state shear regime depend through energy needed to form a defect on the system size, see Ref. [97]. Thus, it is important to use a large number of particles ($N > 5000$) to obtain relevant information about value of yield stress and stationary state structure of system.

The dry solid friction process is characterized by large relative velocities at the interface. In simulations presented here the relative velocity is about $0.01c_{\mathrm{T}}$ (the shear rate is $\dot{\gamma} = 0.001$), where c_{T} is the transverse sound speed. Thus for the GEAM medal, the relative velocity is of the order of $30\,\mathrm{m/s}$. Such high velocities are expected for example in case of thread breaking [98, 99, 100]. The time scale of a solid friction process is estimated by the size of an average asperity and velocity, leading to a value of approximately $100\,\mathrm{ns}$. The typical length of a simulation run is 10^4 time units which corresponds to a total simulation time of about $2\,\mathrm{ns}$. Concerning both lengths and times scales, the simulated systems may represent only a fragment of an asperity. For this reason, the properties of the system such as overall density, pressure, and temperature are taken to be constant within the simulation cell. However, as shown in Sec. 5.6.1 the stationary state structure is reached soon after onset of the shear flow and enables to obtain a picture about interplay between the microstructure, dislocation dynamics, material mixing and flow properties (stress tensor, effective shear rate). The MD simulations with simulation times up to 2.5×10^4 and with different initial configurations (e.g. amorphous, with parallel slip ($[1\bar{1}0]$) and shear directions, and extended in gradient directions) are performed to ensure that processes that might dominate shear deformation are recognized properly during the limited time window of the MD simulations to be discussed.

Chapter 4

Common neighbor analysis

Recent computer simulations of structural phase transitions and plastic flow of model solids [32, 68, 101] prove a need for an analysis which offers a detailed picture about local- and nanostructures on a scale from single to several atoms. The method to be outlined provides the amount and spatial distribution of different structures at every time step, recognizes the amorphous regions and yields information about orientation and shape of crystal domains. Distinct measures of structural information such as structure factors, two-particle correlation functions, order parameters (e.g., Q_{446} via "shape spectroscopy") are not able to provide competitively detailed information [102, 103, 104], since the spatial resolution of proposed method is at an atomic level and neither restricted to mono-crystalline nor to ideal structures.

This method addresses the problem of structure analysis using pattern recognition of the shape of the polyhedron formed by "relevant" neighbors of any individual atom. The meaning of "relevant" will be clarified below and is different from "closest" and "within first coordination shell". The algorithm implements criteria for recognition of the two close packed crystal structures: hexagonal close-packed (hcp) and face-centered cubic (fcc), the almost close packed body-centered cubic (bcc), and the icosahedral (ico) structure. The latter is expected to appear in case of amorphous solids or nanoclusters which tend to be close packed and as an intermediate phase during the transformation of structure, e.g., in the presence of external fields [105]. These four structures are considered for convenience and should be the most relevant for the study of dense fluids and metals modeled by radially symmetric potentials. The algorithm can also be adapted to recognize other structures such as simple cubic structure along the lines indicated in the following sections.

Concerning physical applications of this algorithm, the computer simulation of a homogeneous shear flow has shown the existence of shear-induced changes even in a fluid-like colloidal dispersions subjected to high shear rates [106]. The colloids (or "atoms") formed strings parallel to the stream lines which were sometimes ordered in a perfect hexagonal pattern when projected onto a plane orthogonal to the streaming direction. Similarly, for colloidal crystals it was also observed from snapshots and pair correlation functions that they undergo a structural transition in which two-dimensional hcp (2d-hcp) layers are formed which are oriented to minimize the resistance against flow [107, 108, 109, 110, 111, 112, 113]. This ordering influences the rheological properties,

type	I	II(bcc)	r_{cutoff}	II(fcc/hcp)	III
fcc	1 (12)			$\sqrt{2} \simeq 1.41$ (6)	$\sqrt{3} \simeq 1.73$ (24)
hcp	1 (12)		~ 1.32	$\sqrt{2} \simeq 1.41$ (6)	$\sqrt{\frac{8}{3}} \simeq 1.63$ (2)
bcc	1 (8)	$\sqrt{\frac{4}{3}} \simeq 1.16$ (6)			$\sqrt{\frac{8}{3}} \simeq 1.63$ (12)

Table 4.1: Positions of the coordination shells I-III, the cutoff radius - for clarity placed between shells II(bcc) and II(fcc/hcp) - and the number of the neighbours in coordination shell (in brackets), for three analysed crystal structures.

e.g., enhance shear thinning, since the layered structure complies easily with the flow.

4.1   Relevant neighbors

Usually, as closest neighbors of an atom confined inside an ideal structure, atoms in its first coordination shell should be considered.

i) Taking into account physical reality, namely fluctuations, phonons and non-ideal lattices, it is relevant to note that for the body-centered structure the difference between radial coordinates of atoms within the first and second coordination shells may become very small. In fact, the diameter of the second coordination shell for ideal bcc is just 15.47% larger than the one for its first coordination shell. In contrary, for both, the ideal fcc and hcp structures, this difference is about 41.4%.

ii) Both the fcc and hcp lattice contain regular tetrahedra composed of four atoms. If this lowest level is considered, on which tendency of a material to be close packed can be satisfied, the similar conclusion can be made. The bcc crystal lattice is not composed of regular tetrahedra. The ratio of the edges in tetrahedra consisting only of atoms in the first coordination shell, 1:1:1:1.15:1.15:1.63 (cf. Table 4.1) shows that the local tendency to form regular tetrahedra is not even partially fulfilled on the level of the first coordination shell. On the contrary, tetrahedra consisting of atoms from both first and second coordination shells resemble the regular tetrahedron (1:1:1:1:1.15:1.15).

For these reasons, one should include atoms of the second coordination shell for bcc structures into the analysis of structure. Due to thermal motion of particles atoms from the second shell easily become nearest neighbors in case of a bcc lattice, the first two shells in bcc structure are going to be mixed and they cannot be separated by the Voronoi analysis. This is demonstrated in Fig. 4.1, where already at low temperatures ($T = 0.0152$ in reduced units) the first and second maximum of the bcc structure are overlapping, qualitatively different from the case of fcc structure. The expected number of neighbors will therefore be 14 in the case of a bcc structure. The expected number of (the closest) neighbors for fcc and hcp structures is 12. The ico structure consists of atoms surrounded with 12 neighbors, which form 20 irregular tetrahedra. It is assumed that the first maximum in the pair correlation function of ico structure is at the same position as the first maximum of the other close-packed structures.

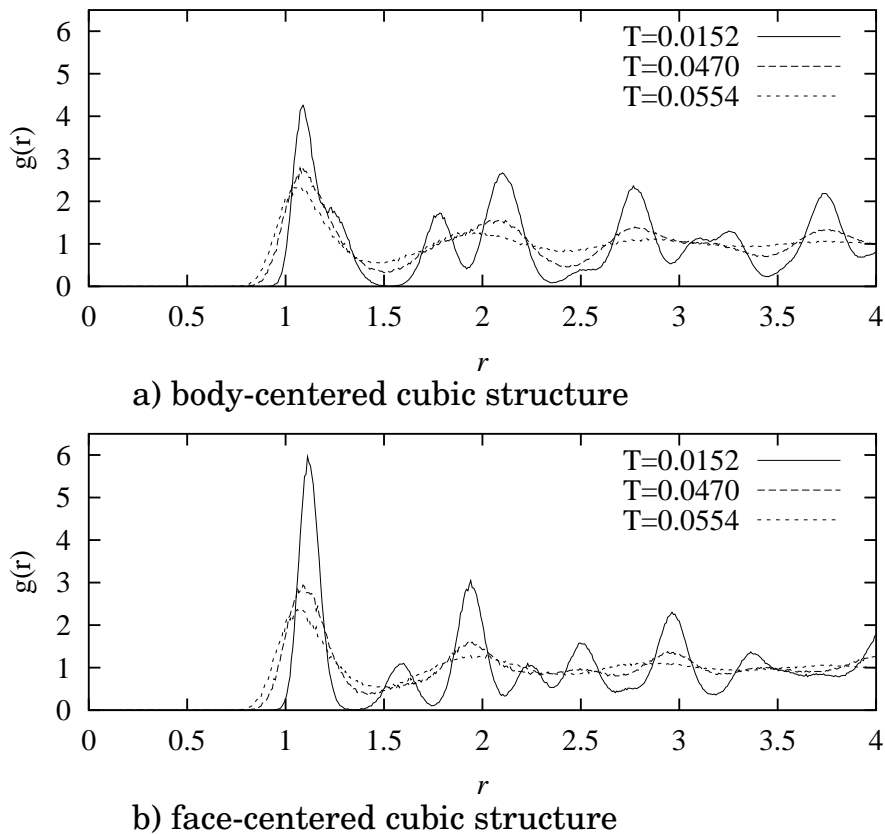Let us call these particles "relevant neighbors" of an atom.

a) body-centered cubic structure

b) face-centered cubic structure

Figure 4.1: The changes of pair correlation function with temperature for a) bcc and b) fcc structure at three temperatures $T/T_{\mathrm{ref}} = 0.0152, 0.0470, 0.0554$.

The code RLSCODE (see Appendix A) makes use of the standard Voronoi construction [87] to determine relevant neighbors. The Voronoi method yields a polyhedron, defined as that region of space closer to the chosen atom than to any other. Neighboring polyhedra, sharing at least a single point, define neighboring atoms. The minimum image convention and a cutoff, the distance beyond which atoms are assumed not to be neighbors are used. These measures can cause unreliable results for small and/or random systems, if the cutoff is chosen without care. To avoid that atoms from second coordination shell of fcc and hcp structures enter the analysis, and to ensure that atoms from the (overlapping) first and second coordination shells of bcc structures enter, a preselection is made by taking cutoff radius to be minimum of the global pair correlation function between the shell containing "relevant neighbors" and the subsequent one, cf. Table 4.1. As shown below, for the purpose of current analysis of non-ideal lattices, this leads to stable results.

4.2 Criteria based on planar graphs

The first step of the analysis is therefore to extract the pair correlation function, the position of its first maximum, as well as the first relevant minimum, (procedure CUTOFFRAD, Table A.2), and to extract from the list of potential neighbors a set of

relevant neighbors by the Voronoi analysis (NEIGHBLST, Table A.2). Next, by using the above mentioned cutoff a planar graph for each atom is established based on this set of relevant neighbors (STRUCTLST). The neighbors are represented by nodes - the central atom is not included in the graph, and the nodes are connected with an edge if two neighbors of an atom are also neighbors of each other. The graph does only contain information about connections. Note that atoms in set of neighbors of an atom do not have to be neighbors of each other.
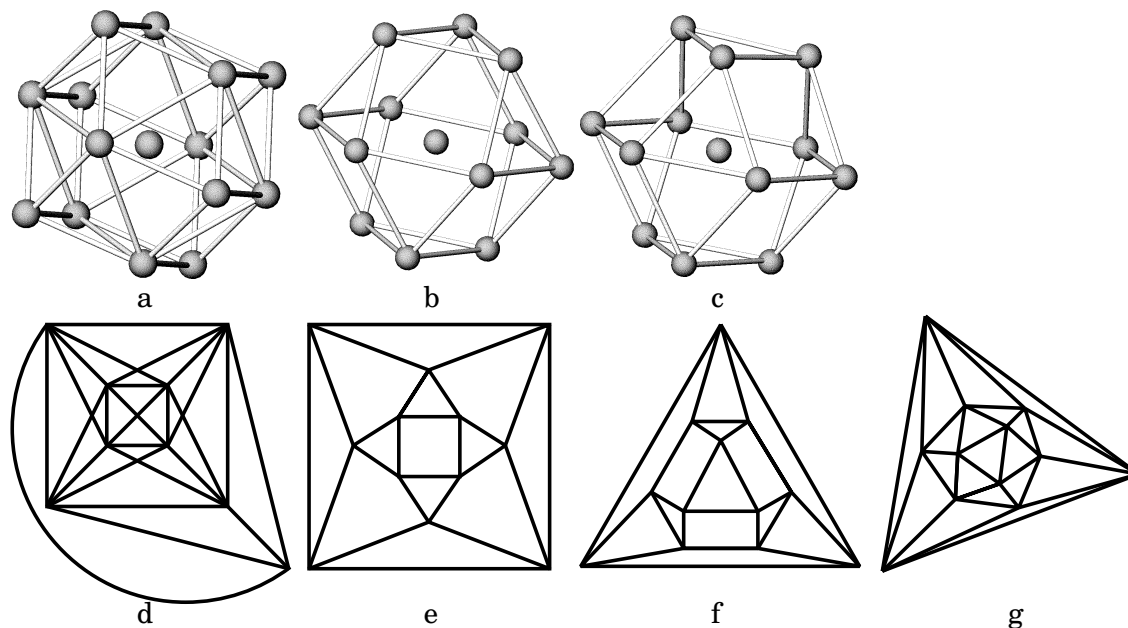

Figure 4.2: The disposition of neighbors around atom in case of ideal crystal structures and the planar graphs defined on members of set of neighbors of one atom in bcc (**a,d**), fcc (**b,e**), hcp (**c,f**) and ico (**g**) structure. The nodes represent the neighbors and they are connected with a branch (edge) in case if they are also neighbors.

The planar graphs are topologically different for each of the four structures of interest (cf. Fig. 4.2). A change of the orientation of a certain crystal structure does not result in topologically different planar graphs. The criteria to determine if the graph of a single atom is topologically equivalent with the planar graph of one of the structures is discussed next. The Euler theorem for planar graphs and further relations connecting the total number of the edges and the number of different surfaces – with three, four and more edges – into which the plane is divided by a planar graph, are used. The Euler theorem states that a connected and planar graph with n nodes and m edges divides the (infinite) plane into $f = m - n + 2$ surfaces. The theorem is derived by induction over the number of edges for any number of nodes [114]. In following, the usefulness of the approach will be illustrated on an example of the bcc structure.

From the Euler theorem, the number of surfaces in case of bcc is 24 since the number of neighbors (nodes) is 14 and the number of edges is 36. Let us assume that there are surfaces also surrounded with more than three edges, e.g., with four edges. The number of these surfaces is denoted by $\triangle$ and $\diamondsuit$ for surfaces with three and four edges, respectively. The equations for surfaces and edges of the planar graph in this case read, respectively,

$$\diamondsuit + \triangle = 24,$$
$$4\diamondsuit + 3\triangle = 2 \times 36. \tag{4.1}$$

There is a single solution, $\triangle = 24$ and $\diamondsuit = 0$. Similar relations can be written for the planar graph with same number of nodes and edges, which divides the plane into surfaces with arbitrary number of edges: Inserting $\sum_{x=3}^{\infty} ⓧ = 24$ (with ③ $\equiv \triangle$, ④ $\equiv \diamondsuit$ etc.) into $\sum_{x=3} xⓧ = 2 \times 36$ yields $\sum_{x=4}^{\infty}(x-3)ⓧ = 0$. Since all ⓧ's are positive numbers, one has $\forall_{x \geq 4} ⓧ = 0$. It is therefore proved that just the planar graph with 24 triangular surfaces does exist (③ $= 24$). Trying to combine 24 triangular surfaces in a planar graph, it is found that only one configuration is possible, the one characteristic for the bcc structure (Fig. 4.2). There are eight nodes with four edges and six nodes with six edges.

In bcc structure eight neighbors of the atom have four neighbors and the remaining six neighbors have six neighbors within the set of neighbors of the central atom. The minimum and sufficient criterion for bcc structure is: an atom is surrounded with bcc structure if it has 14 neighbors and eight of them have four neighbors and six of them six neighbors within the set of neighbors of the central atom.

In ico structure the atom should have 12 neighbors and each neighbor should have five neighbors (Fig. 4.2g). Both in the fcc and hcp structure the atom has 12 neighbors which form eight triangular and six square surfaces. While hcp structure has three pairs of triangular surfaces with the same edge, fcc structure has none and this fact is now used to distinguish between hcp and fcc, see Figs. 4.2e-f.

The ratio between all atoms which are found to belong to that structure (central atoms plus their neighbors, no double counting) and total number of atoms in the system is taken as a measure of the amount of certain crystal structure in the material.

4.3 Test run: MD computer simulation of melting

The test run is concerned with the melting of the generic model metal GEAM described in the preceding section by means of a NVT molecular dynamic method for $N = 10978$ particles, starting from an ideal fcc and bcc lattice, respectively. Basic details on the implementation of computer simulation method can be found in the Sec. 3. Simulation with constant density $n/n_{\mathrm{ref}} = 1$ have been performed. The temperature is increased stepwise by $\delta T/T_{\mathrm{ref}} = 0.0006$ every 800th time unit in the range $T/T_{\mathrm{ref}} = 0.005, \ldots, 0.065$. Before the temperature is increased configurations were saved to a file, which is provided here as test examples. The temperature is kept constant by rescaling the magnitude of the particle velocity which corresponds to the Gaussian constraint of constant kinetic energy (Sec. 3.3). A cubic simulation box with volume V, and periodic boundary conditions are used. The axes x, y, z correspond to the initial crystal directions [100], [010], [001], respectively. The angles, in angular distribution plots, are introduced as the angle, ϕ, between projection of vector in xz-plane and z axis taking the values in range $[-\pi, \pi]$ and the angle, θ, between y-axis and vector, its values are in range $[0, \pi]$. Cutoff radius is calculated only once for the configuration with the lowest temperature.
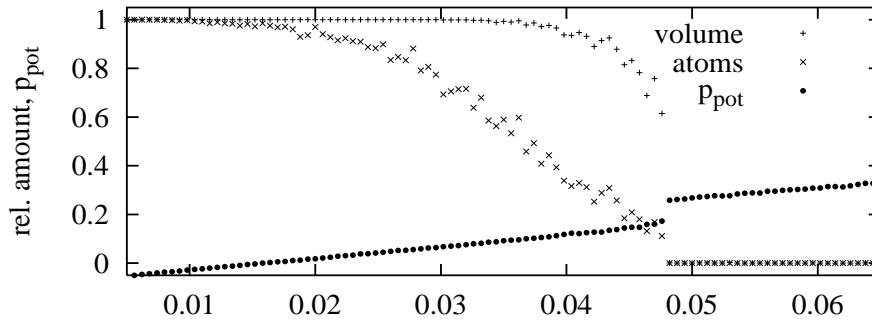
a) body-centered cubic structure
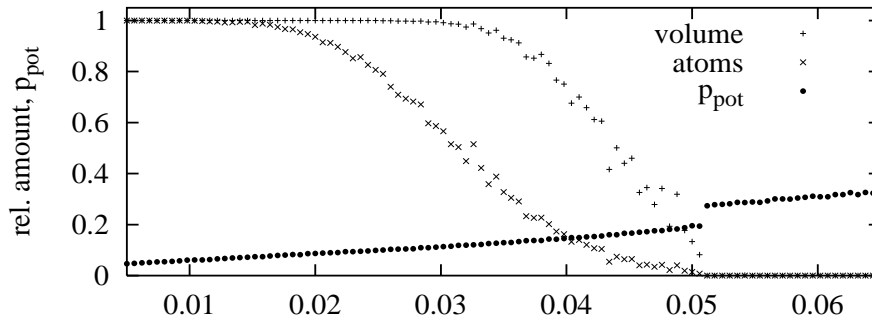
b) face-centered cubic structure

Figure 4.3: Molecular dynamics simulation of melting, starting configuration is (a) bcc and (b) fcc. The relative number of atoms ($\times$) surrounded with crystalline structure, relative volume ($+$) occupied by atoms and their neighbors, and potential part of pressure ($\bullet$) are presented.

In Figure 4.3, relative number of atoms found to be surrounded by neighbors, which resume (a) bcc and (b) fcc structure pattern, and relative volume occupied by atoms and their neighbors in these structures are presented. The evolution of potential part of pressure with the increase of temperature is given for comparison. The relative volume is larger than the relative number of atoms in fcc structure, since the crystalline parts of the sample are fragmented (Fig. 4.4). That results in fact that less that 4% atoms whose neighbors have fcc pattern, fill with their neighbors almost 30% of box volume. Occasional increases of observed crystalline structure after the increase of temperature can be explained as consequence of fluctuations.

The changes in the fcc lattice with the temperature are illustrated in Fig. 4.4 with the cross section in plane y=0 (the crystal plane [100]) and angular distribution of directions to the closest neighbors of atoms for three different temperatures $T/T_{\mathrm{ref}} = 0.0152, 0.0470, 0.0554$, the number of atoms and relative volume are given for comparison. The slice is $\delta y = 1$ wide.

At temperature $T/T_{\mathrm{ref}} = 0.0470$, a greater dispersion of atoms around these maximums is visible. In the melted state, the angular distribution of neighbors is uniform, and on cross section of the system absence of the any order is visible.

The mixing of atoms of first and second coordination shells can be observed - as
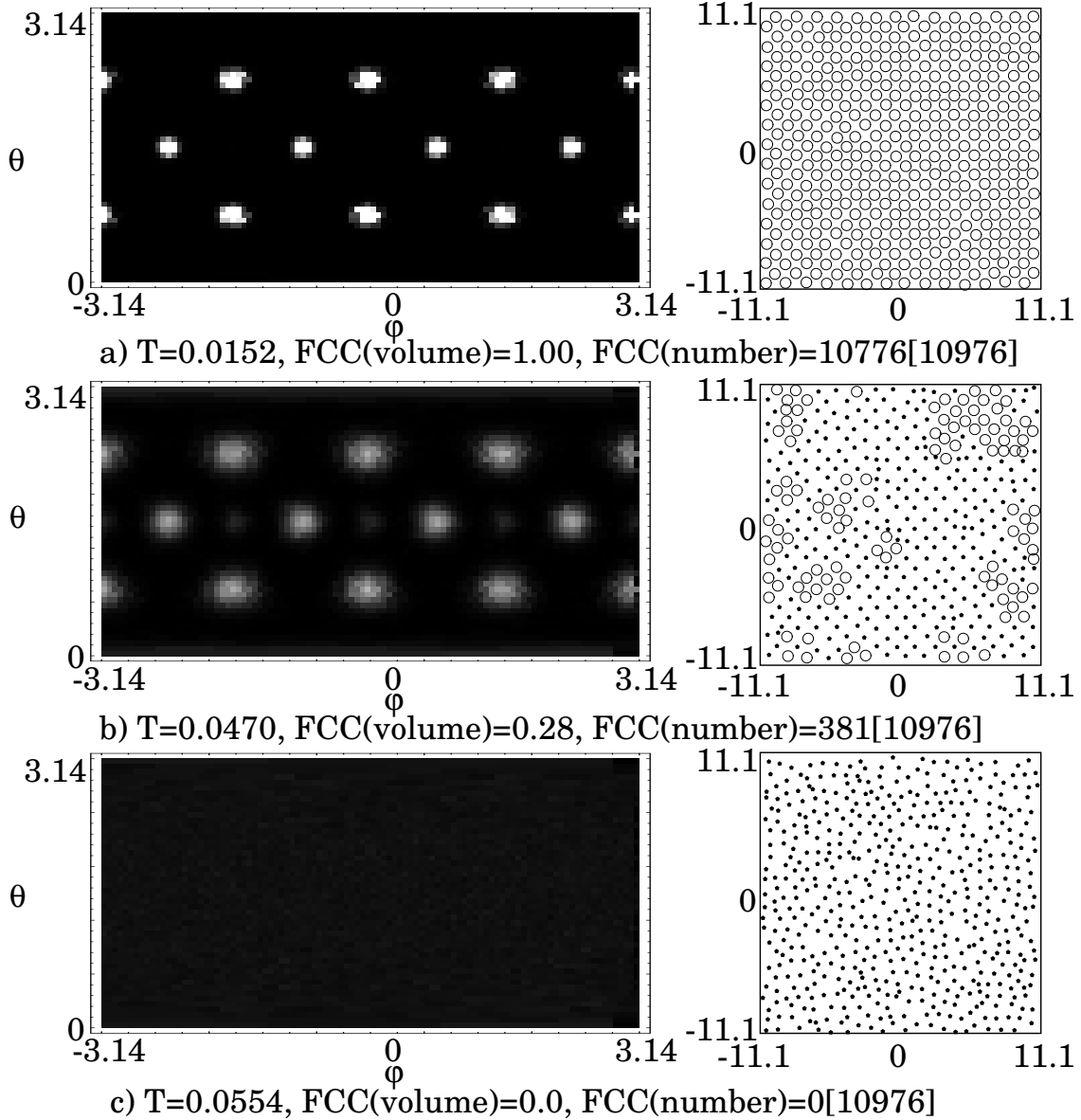
Figure 4.4: The angular distribution of directions to the closest neighbors and cross section of the system in plane y=0 (the slice is $\delta y = 1$ wide). Dimensions of the system are $L_x, L_y, L_z = 22.2$. The plane of cross section corresponds to [100] plane of the crystal. The atoms and their neighbors whose spatial distribution corresponds to fcc structure are represented with $\bigcirc$, others are represented with $\bullet$. The evolution of the system with increase of the temperature is illustrated $T/T_{\text{ref}} = 0.0152, 0.0470, 0.0554$.

the points between angular distribution function maximums of original structure at temperature $T/T_{\text{ref}} = 0.0470$. This can be also observed in the pair correlation function of the same system given in Fig. 4.1.

Chapter 5

Structure in the steady shear flow regime

5.1 Mechanical properties of bulk GEAM metal

When a material is subjected to deformation or an increase of temperature, it responds with changes of its free energy and pressure. At low temperatures the particles are near to their positions in an ideal crystal. The isotropic "cold" pressure $p_{\text{cold}}(n)$ is calculated by inserting distances of nearest neighbors (for an ideal lattice) into Eq. (2.3). A modification of the known expression for the "cold" pressure has been recently used to model the isotropic pressure at finite temperatures for the case of the SHRAT potential used here, see Ref. [66]. The adapted formula for the pressure takes into account that with increasing temperature particles approach each other more closely, and reads:

$$p_{\text{solid}}(n, T) = nk_{\text{B}}T + \frac{1}{2}[p_{\text{cold}}(n + s_{\text{F}}(n, T)) + p_{\text{cold}}(n - s_{\text{F}}(n, T))]. \qquad (5.1)$$

It is observed that the factor $s_{\text{F}}(n, T)$ depends on the strength of the embedding functional $\mathcal{F}$ (here only F_2 is considered) and also on the type of crystal structure as follows:

$$
\begin{aligned}
s_{\text{F}}^{\text{fcc}}(n, T) &\approx \sqrt{(5.25 - 1.25F_2)\frac{k_{\text{B}}T}{e_2}}, \\
s_{\text{F}}^{\text{bcc}}(n, T) &\approx \sqrt{(4.5 + 0.5F_2)\frac{k_{\text{B}}T}{e_2}}.
\end{aligned}
\qquad (5.2)
$$

Coefficients $s_{\text{F}}^{\text{fcc}}(n, 0) = s_{\text{F}}^{\text{bcc}}(n, 0) = 0$ and $e_2 = \partial^2 E_{\text{coh}}/\partial n^2$. Equation (5.2) improve the corresponding expression given in Ref. [66]. Though one could discuss further corrections to the expression for $s_{\text{F}}(n, T)$, the proposed Eq. (5.2) shows good agreement with simulation results as demonstrated by Fig. 5.1. This figure presents equilibrium molecular dynamics (MD) results for the heating of the EAM metal (at $n = 1.00$) for different model parameters. The temperature is increased stepwise between $T = 0.006$ and 0.04 ($\triangle T = 0.002$ each 1000 time units). In Fig. 5.1, MD results for p^{iso} are denoted by symbols, and lines stem from the analysis based on the above expressions
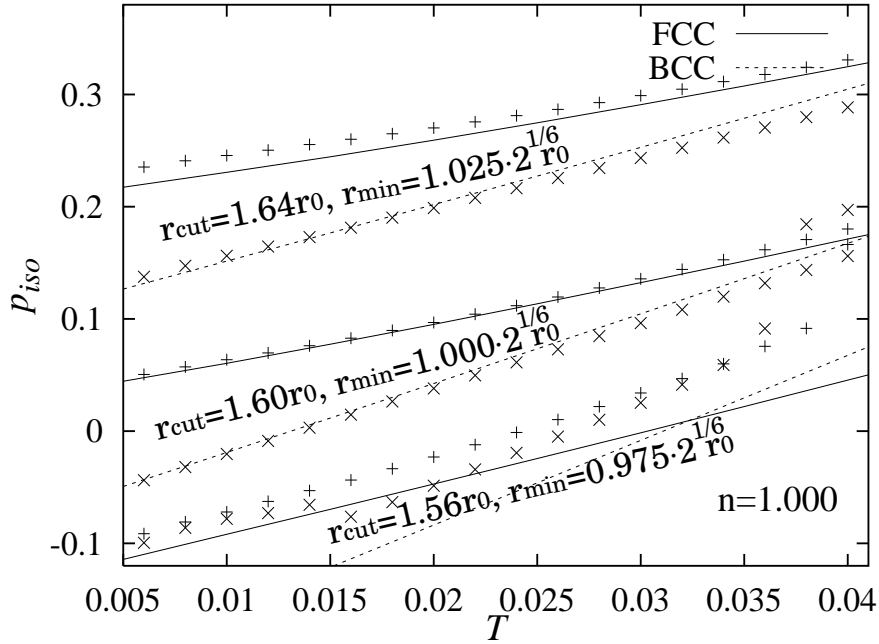
Figure 5.1: Pressure as function of temperature (in standard LJ units) for different model parameters, cutoff $r_{\min}$ and minimum of the potential $r_{\min}$. Molecular dynamics (MD) simulation results for p^{iso} are denoted with $+$ (bcc configuration) and $\times$ (fcc). The curves represent the approximate expression for the pressure, Eqs. (5.1) and (5.2). Global density in the system is $n = 1.00$.

(5.1) and (5.2). The system can withstand tension due to internal attraction, when the pressure is negative. This is a consequence of the presence of boundary conditions at fixed volume. For the large negative pressures (model parameters: $r_{\min} = 0.975 \times 2^{1/6}$, $r_{\mathrm{cut}} = 1.56$, $F_2 = 1$) holes in the system are created, and the system does not reach a stable state within the simulation time. For the same system, melting is observed near the temperature $T = 0.035$.

The isothermal bulk modulus and shear modulus determine the elastic properties of an isotropic solid. Using the approximate expression for the isotropic pressure [Eqs. (5.1) and (5.2)], an approximate expression for the bulk modulus is obtained directly. It is shown in Fig. 5.2 for a range of temperatures and densities where the system is solid. The elastic moduli decrease with increasing temperature. At higher temperatures the fluctuation contribution to the shear modulus is of the same order of magnitude as the Born-Green contribution. In the molten state the shear modulus vanishes.

5.2   Plastic yield

Representative results of the NEMD simulation concerning elastic response and plastic yielding of the solid GEAM are presented in Fig. 5.3. The system responds with growing shear stress $(-P_{xy})$ to an increasing shear deformation $\gamma = \dot{\gamma}t$ (constant shear rate $\dot{\gamma}$) switched on at $t = 0$. In this figure, shear stress is plotted as function of shear deformation for an initially prepared fcc GEAM metal at temperatures $T = 0.01, 0.04$ and
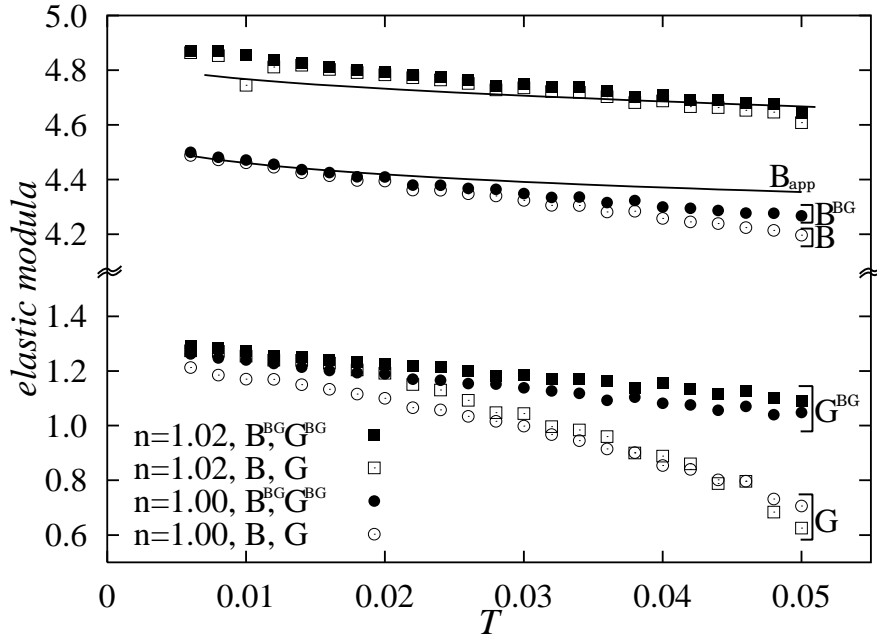
Figure 5.2: Shear modulus (G), bulk modulus (B) and their Born-Green contributions vs temperature for densities $n = 1.00, 1.02$ for GEAM in dimensionless LJ units, obtained via nonequilibrium molecular dynamics (NEMD). The curve for bulk modulus (B_{app}) is calculated inserting the approximate expression for pressure, Eqs. (5.1) and (5.2), into the definition of bulk modulus.

three different shear rates $\dot{\gamma} = 0.001, 0.005$, and 0.01 (reduced units). The axes x, y, z correspond to the directions [100], [010], [001] in the initial crystal structure. It is seen that the yield deformation does not depend on the shear rate for $T = 0.01$. This may be expected in view of Lindemann's criterion which says that a crystal will melt when the amplitude of vibration (x_0) of atoms exceeds about one-tenth of the lattice constants. The smaller values of the yield deformation at high temperature $T = 0.04$ and $\dot{\gamma} = 0.001$ can be also explained by this criterion. By assuming a harmonically oscillating motion of atoms, one obtains the relation $kT = f x_0^2 / 2$ between temperature and the amplitude of vibrations, where f stands for an effective spring coefficient between an atom and its neighborhood. The coefficient f can be related to elastic moduli, see Ref. [115], and it falls with temperature. High temperatures and a small spring coefficient result in a large amplitude of oscillations and a small yield deformation.

The plastic behavior following the yield point, however, depends on shear rate. At high rates (and high temperatures) defects are formed immediately after a yield stress is reached. This results in a slowdown of the relaxation of accumulated stress at high shear rates. Under these conditions, soon after the yield point has been reached (here at $\gamma = 0.1$), shear-induced melting is observed. During this intermediate state (inhomogeneous melting), a layer of liquid metal is formed between two blocks of the solid metal, and the blocks are moving at constant speed, see upper left cross section in Fig. 5.8. Actually, the periodic simulation cell contains 34 layers of particles and an effective shear rate at the position of the layer is $\sim 34\dot{\gamma}$ – just at startup of flow. For this reason, for systems at temperatures near the melting point ($T = 0.04$) and at high
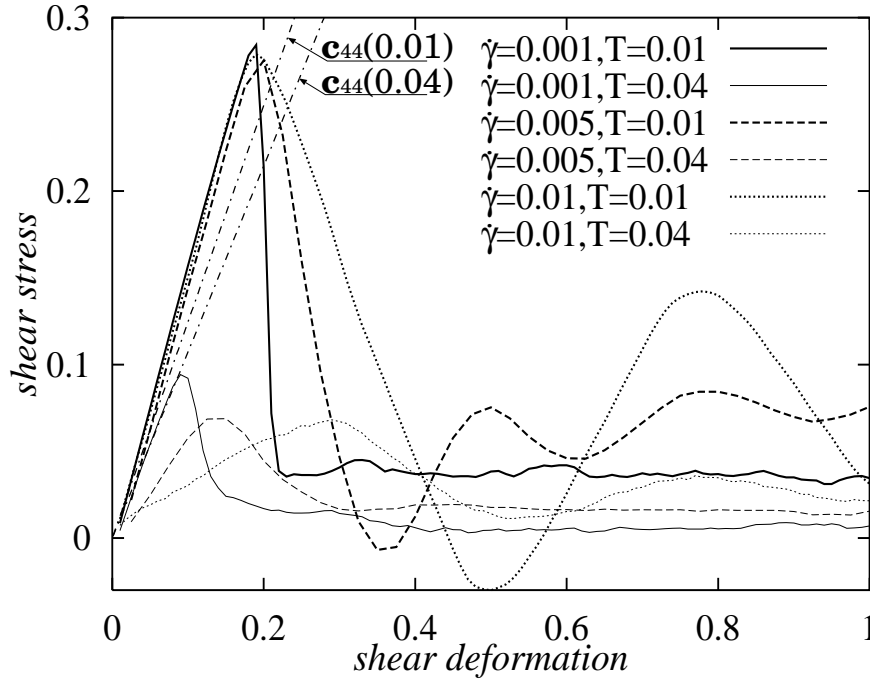
Figure 5.3: Shear stress as function of deformation for three shear rates $\dot{\gamma} = 0.001, 0.005$, and 0.01 at two temperatures $T = 0.01$ (thicker curve) and $T = 0.04$ (thinner curve) of GEAM, obtained via NEMD. The starting configuration is the ideal fcc structure at density $n = 1.00$ with $N = 43000$ particles. The shear started at $t = 0$. Shear direction is the [100] direction in crystal, and shear plane coincides with the (010) crystal plane. The coefficient C_{44} is obtained via MD simulation. All quantities are given in LJ units.

shear rates $\dot{\gamma} = 0.005, 0.01$ the system partially melts soon after the shear commenced. In Ref. [30], a similar behavior is observed during sliding of a tetrahedral tip (Cu) over substrate (Ni) via simulation. The stick-slip motion is observed, with abrupt structural transition of the tip layer closest to the substrate between two slips in which Cu (110) surface transformed into (111) surface to match (111) surface structure of Ni substrate. Two comparisons with inhomogeneous melting in current system can be made: (*i*) regions in intermediate shear regime exist (before stationary state structure is formed, Fig. 5.3), where motion is converted to the strain energy. A part of the strain energy is spent on the structure change (melting) of the structure between the blocks and the rest is dissipated though the system. (*ii*) The structure of the fluid at the interface tends to match the interface surface structure [30, 116]. The observed melting is a result of two opposed mechanisms, blocks have fcc (100) surface structure but the system tends to form fcc (111) structure in this plane (see Sec. 5.4).

The measured yield stress decreases considerably with temperature, since particles at comparatively high temperatures can cross the potential barrier and enter the next potential minimum faster.

5.3 Rheological properties for stationary shear flow

For a planar Couette flow the symmetric traceless pressure tensor (which equals the negative stress tensor) has only three independent components $p_{+,-,0}$, a shear pressure $p_+ \equiv P_{xy}$ or shear stress $-P_{xy}$, and two normal pressure differences: $p_- \equiv (P_{xx} - P_{yy})/2$, $p_0 \equiv [2P_{zz} - (P_{xx} + P_{yy})]/4$. The pressure tensor is calculated via NEMD over the range of temperatures $T = 0.008, \ldots, 0.06$, for densities $n = 0.98, \ldots, 1.08$, and for two shear rates $\dot{\gamma} = 0.001, 0.01$. These simulations are performed with 1000, 2000, and 43000 particles.
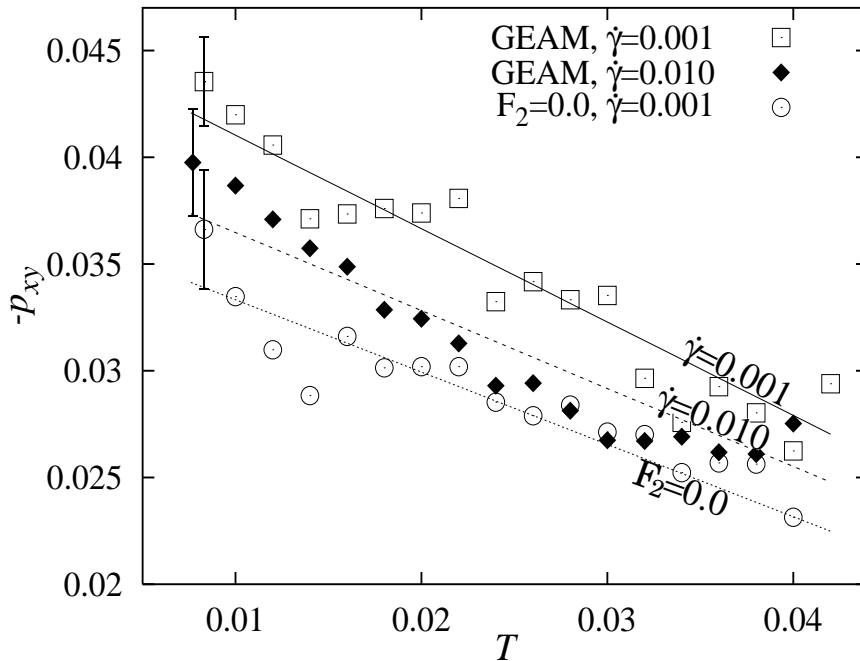

Figure 5.4: Shear stress vs temperature. Symbols denote averages from the NEMD simulation of GEAM with different densities for two shear rates $\dot{\gamma} = 0.001, 0.01$ ($F_2 = 1$) and for $F_2 = 0$ ($\dot{\gamma} = 0.001$). All quantities are expressed in LJ units. Curves are obtained by linear regression analysis of the simulation results. Estimated error ranges (standard deviation) have similar size for all data points, for this reason they are plotted only at $T/T_{\text{ref}} = 0.08$.

In order to discuss the relationship between shear stress and temperature for two shear rates a simple linear relationship between them is tested, where the coefficients are obtained via regression. Within statistical errors and for the range of chosen densities, no effect of density on the friction pressure is detected. The resulting approximate expressions are given in Table 5.1. The regression curves of shear stress ($-p_+$ or $-P_{xy}$) together with the simulation data are presented in Fig. 5.4. Data are plotted for two shear rates $\dot{\gamma} = 0.001$ (solid curve), $\dot{\gamma} = 0.010$ (dashed curve) and $\dot{\gamma} = 0.001, F_0 = 0$. (dotted curve). The shear stress decreases with increasing temperature. This is so, because atoms have large kinetic energies and can move uncorrelated and far from their

$\frac{r_{\min}}{2^{1/6}}$	$\frac{r_{\text{cut}}}{1.6}$	F_2	$\dot{\gamma}$	a_T	c
1.	1.	0.	0.001	-0.34(6)	0.037(1)
1.	1.	0.5	0.001	-0.47(6)	0.039(2)
1.	1.	1.	0.001	-0.44(5)	0.045(1)
1.	1.	1.	0.010	-0.37(5)	0.040(1)
1.025	0.95	1.	0.001	-0.5(2)	0.092(5)
1.025	1.05	1.	0.001	-0.64(7)	0.055(2)

Table 5.1: Coefficients in approximate expressions for shear stress, $-p_{xy} = a_T T + c$, in Figs. 5.4 and 5.5 for different values of model parameters r_{cut}, $r_{\min}$ and F_2 (all other parameters are zero).

equilibrium positions as compared to atoms in a layer plane. For the same reason, the observed shear stress decreases with increasing shear rate. At a higher shear rate more defects are produced and the ordering of atoms into hexagonal layers is weakened, see the insets of Fig. 5.8. The embedding contribution reduces density fluctuations, making atoms more bounded into layer structure, thus the shear stress decreases with decreasing influence of the embedding contribution, cf. Table 5.1 and Fig. 5.4. From simulations, the kinetic and potential contribution to the pressure tensor can be computed separately. The kinetic part of the isotropic pressure is given by $p_{\text{kin}}^{\text{iso}} = kT$ and of the order of the potential contribution to the pressure. The kinetic contributions of the shear stress ($-p_+$) and normal pressure differences ($p_{-,0}$) is only about 10^{-3} of the potential contribution. This is expected for dense fluids and solids. The simulated values of the two normal pressure differences $p_{-,0}$ are found to vanish both within the precision of data presented in this work.

In Fig. 5.5, the data are presented for three systems: GEAM (with fcc ground state structure and shear moduli $G = 1.31$), for model parameters $r_{\min} = 1.025 \times 2^{1/6}$, $r_{\text{cut}} = 1.68$, $F_2 = 1$ (bcc, $G = 1.33$) and $r_{\min} = 1.025 \times 2^{1/6}$, $r_{\text{cut}} = 1.52$, $F_2 = 1$ (fcc, $G = 2.39$). Since the shear stress and moduli have the same origin in shape of two-body interaction potential, the observed shear stress increases linearly with increase of the shear moduli. The dependencies of the shear stress on the temperature and the shear rate are particularly important when the metal is subject to severe stresses or non-uniform heating, e.g., as result of thread-breaking [98, 99, 100].

In a liquid metal, atoms are quite free to move and the system exhibits a comparable small resistance to the shear flow, cf. the enclosed points in Fig. 5.6(a) and 5.6(b). This means that if the model metal stays crystalline (during shear) it mostly reduces energy per particle rather than reducing resistance to shear. Thus, the observed reordering of the crystal structure under shear has little in common with the mechanism responsible for an ordering transition – accompanied by shear thinning – observed in fluids [14]. The present transition is similar to an ordering phenomenon observed experimentally and predicted theoretically for colloidal crystals in solid state [16]. However, in colloidal crystals the shear stress rises at the melting transition [14, 15, 16]. The structure in a colloid is formed to reduce the resistance to shear. Only if the shear rate and the temperature are sufficiently low, the system can reduce the potential energy by forming
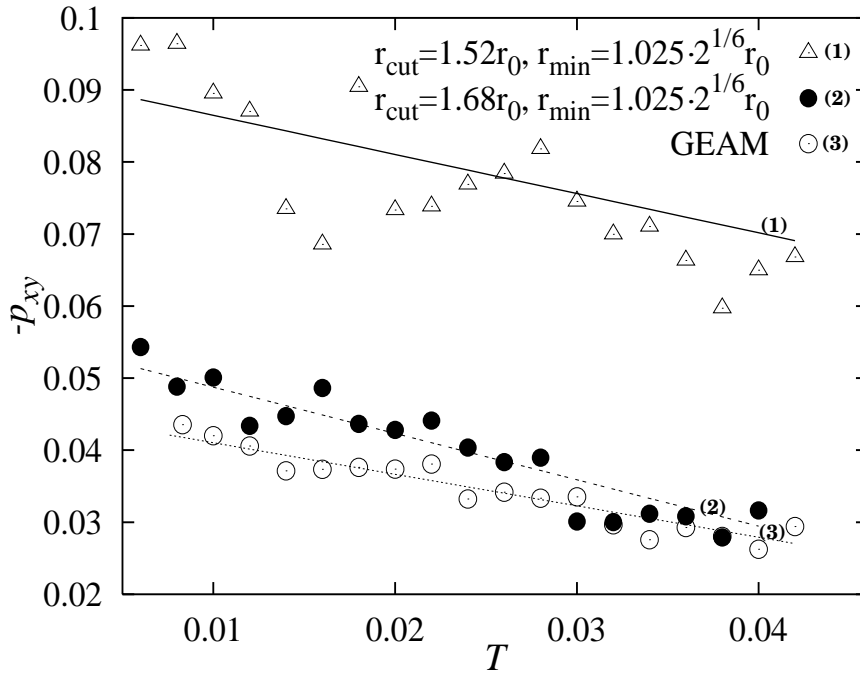
Figure 5.5: Shear stress as function of temperature (in standard LJ units) for different model parameters, minimum $r_{\min}$ and cutoff radius of the potential r_{cut}. Symbols denote averages from the NEMD simulation at shear rates $\dot{\gamma} = 0.001$. Curves are obtained by linear regression analysis of the simulation results.

periodic crystal structures. In metals the interaction between atoms is stronger than in colloids and the mechanism which tries to reduce the potential energy of the system is dominant. The data points in Fig. 5.6 stem from NEMD simulations at different densities, shear rates, and temperatures.

The equilibrium and nonequilibrium values for the isotropic pressure are shown in Fig. 5.7 as function of temperature T and density n. The symbols mark the computed pressure for the system under shear. The curves represent the evolution of the isotropic pressure during melting of a bcc system (dashed curve) and a fcc system (solid curve) without shear. The increase of pressure at high temperatures indicates the onset of a shear-induced melting [118]. For the high densities ($n = 1.02, 1.04$), the observed structure in the system is mainly of bcc type, resulting in an isotropic pressure smaller than the one for the corresponding fcc structure.

In case of dry solid friction between two blocks made of the same material, the load is related to the isotropic pressure inside the interface (asperity). Except in the case of polished surfaces, all asperities will be in state of incipient flow, see Ref.[1]. The simulation cell can be regarded as containing a typical part of such an interface. The typical value of the isotropic pressure should be therefore estimated from the penetration hardness, which is defined as the ratio between load N and contact area A at the onset of plastic flow. For most metals, the penetration hardness lies in the range 0.005-0.025 (reduced Lennard-Jones (LJ) units) [1, 2]. From simulation data in Fig. 5.7 it is visible that with and also without shear one can consider the penetration hardness as a good estimate for the average isotropic pressure within an asperity. The friction
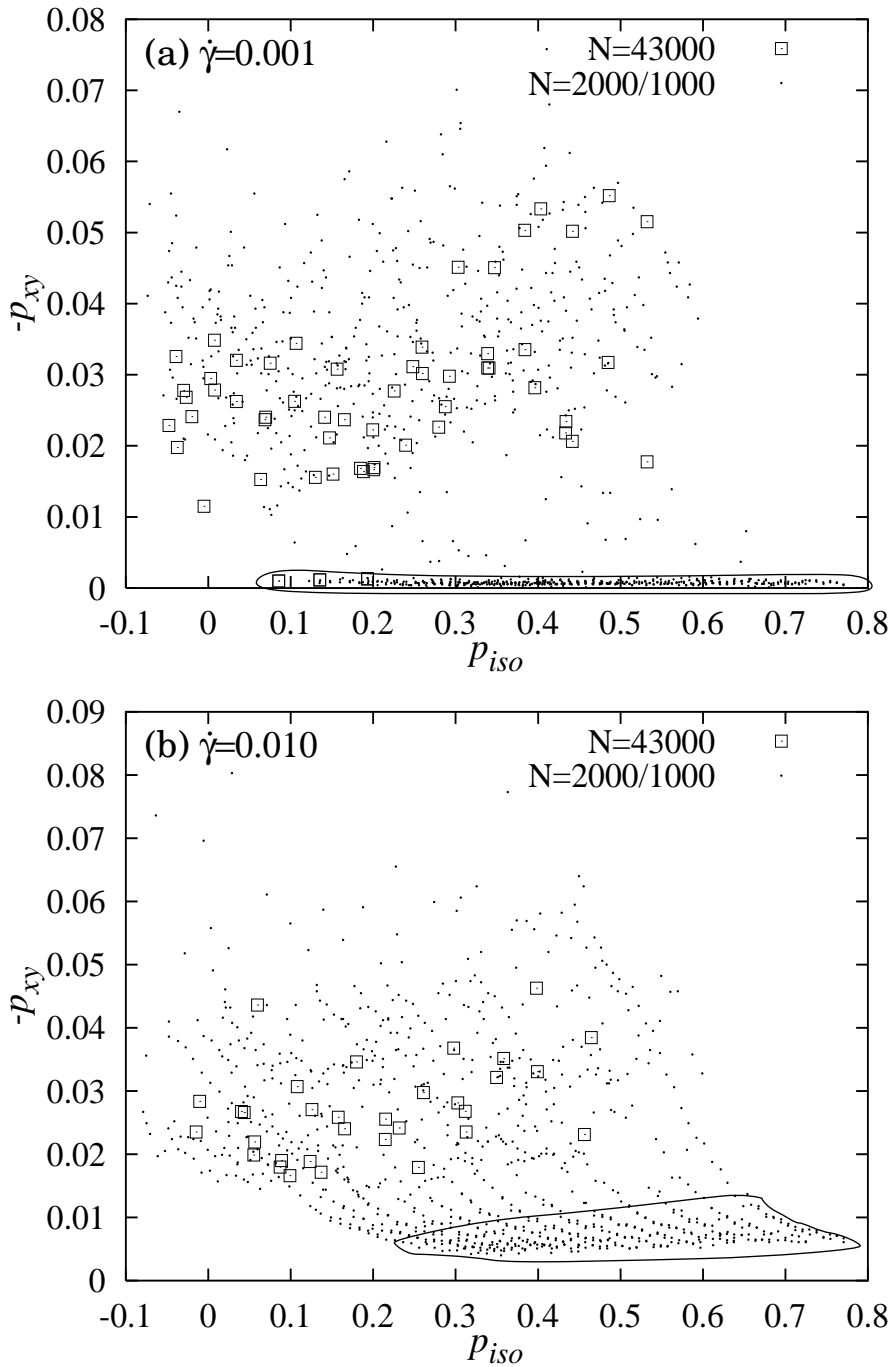
Figure 5.6: Shear stress $-p_{xy}$ vs the isotropic part of the pressure, for two shear rates: (a) $\dot{\gamma} = 0.001$ and (b) $\dot{\gamma} = 0.01$. Symbols indicate results from NEMD simulations of GEAM for different densities and temperatures. All quantities are given in LJ units. Data points where the system is molten are encircled with a line.

coefficient is defined as the ratio between shear stress (integrated over the volume of an asperity) and the load. Under the assumption for sufficiently high loads, e.g., large surfaces of asperities that the isotropic pressure and the shear stress are homogeneous inside the asperity, a "macroscopic" friction coefficient μ is obtain via NEMD in the
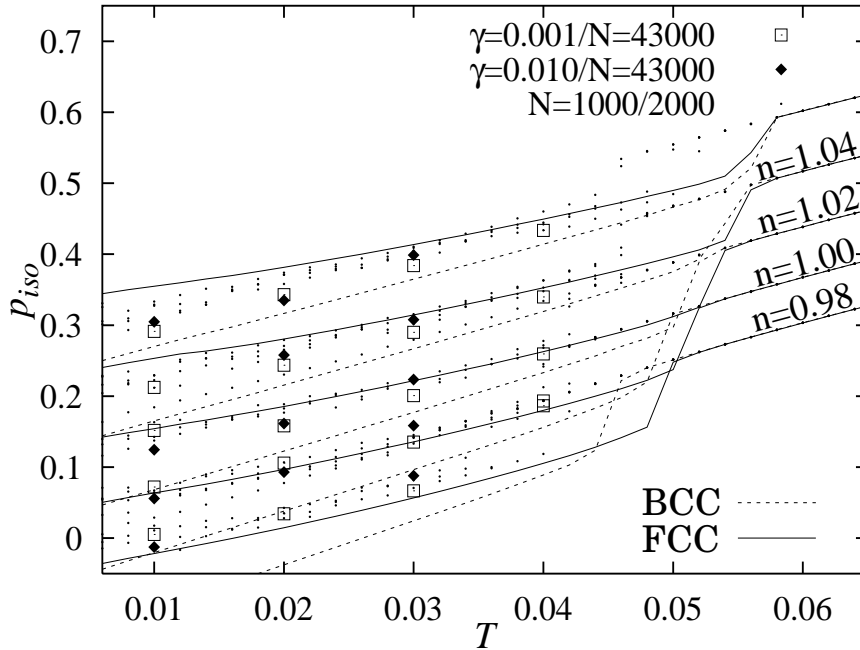
Figure 5.7: Effect of temperature on the isotropic part of the pressure of the system under shear. Symbols indicate results from NEMD simulation of GEAM at different densities, number of particles, temperatures, and shear rates. The curve for isotropic pressure comes from the molecular dynamics simulations of melting for different densities for bcc and fcc structure (without shear). All quantities are given in standard LJ units.

range between 0.2 and 3, defined as $\mu \equiv -p_{xy}/p^{\mathrm{iso}}$. These values are comparable to the ones for real materials. With the available mesoscale methods, such as smooth particle hydrodynamics, which allow to simulate a surface containing several asperities it would be possible to obtain improved values for the analog to the experimentally measured, macroscopic, friction coefficient. Such an investigation is outside the scope of the present work.

The shear stress does not change as much as the isotropic pressure does during the variation of temperature and density. Even at large isotropic pressures above $p^{\mathrm{iso}} = 0.4$, which is realized in shock waves and impact experiments, the shear stress stays near its value at zero-pressure. Strings of the data points, visible in the Fig. 5.6(b), can be understood resulting from partial melting of the system at high temperatures. Partial melting is observed at the (larger) shear rate $\dot{\gamma} = 0.010$, at temperatures below $T = 0.04$. Shear-induced melting is observed at temperatures above $T = 0.04$, see Fig. 5.10. This figure will be further commented in the following section.

5.4   Stationary state structure

In the preceding section, it is demonstrated that shear stress rises before reaching the yield stress for a system subject to shear deformation. After reaching this stress, atoms tend to move into the next potential minima while the system relaxes, as is also reflected by oscillations in Fig. 5.3. If the shear continues, significant structural changes appear in the system. Shear-induced structural local (re)ordering is followed by changes in the streaming profile and by a buildup of long-range order.

Figure 5.8 shows a time series for a subsystem of a cubic cell with $N = 43200$ particles undergoing shear at two different densities $n = 1$ and $n = 1.02$ and small and intermediate rates $\dot{\gamma} = 0.001$ and $\dot{\gamma} = 0.01$, respectively. The snapshots (including structure analysis) show a cut of width $\triangle r = 1$ of the full system, and the direction of shear is depicted in the top right snapshot.

Another quantitative analysis of the evolution of the crystal morphology for the same system with time is presented in Fig. 5.9. The common neighbor analysis method based on planar graphs is used to extract information about structure from the NEMD data, see Sec. 4. The list of the neighbors is used as an input for a pattern recognition which resolves fcc, bcc, hcp, as well as icosahedral structure (ico). The icosahedral structure preferably occurs in amorphous solids. The ratio between all atoms which are found to belong to a structure (central atom plus its neighbors, no double counting) and total number of atoms in the system is taken as measure of the amount of certain crystal structure. In current model all three crystal structures are observed. At high shear rates ($\dot{\gamma} = 0.01$), the icosahedral structure is observed in an intermediate state, see Fig. 5.9.

At the shear rate $\dot{\gamma} = 0.001$, after the yield stress had been reached, a sudden increase in the amount of hcp structure is observed from Fig. 5.9, the crystal planes shear oblique to the shear direction and form a defect. The defect is visible in the cross section shown in this figure for $t = 500$ as the area where both hcp and fcc structures are present. The generated defect blocks flow and induces a further increasing shear stress. Particles gain kinetic energy by randomly moving away from the defect. As a result, the system melts locally. This causes the appearance of gradual rearranged areas around the defects in the system. To make this better visible the angular distribution of directions to next neighbors is also provided in the insets in Fig. 5.8. The shear direction is marked with two crosses ($\times$) in the insets, and the plane normal to flow gradient projects on a line (not drawn) connecting the crosses. During this structural transition closest neighbors of an atom change their disposition and local structure, on level of an atom and its neighbors "rotates", see insets for $\dot{\gamma} = 0.001$, $n = 1.00$ in Fig. 5.8. In this transformation two dimensional densely packed layers are formed where the shear direction is in parallel with the nearest neighbor direction at $t = 4000$ in Fig. 5.8, visible as strings of particles. In the stationary state the distance which the particles cross between two minima is the smallest possible in the system. This reduces the probability for creating new defects. The densely packed layers are stacked along the gradient direction to maximize the distances between particles as they shear past each other and reduce resistance to shear. For the fcc structure the most densely packed planes correspond to the (111) plane and the shear direction to the $[1\bar{1}0]$ direction. The
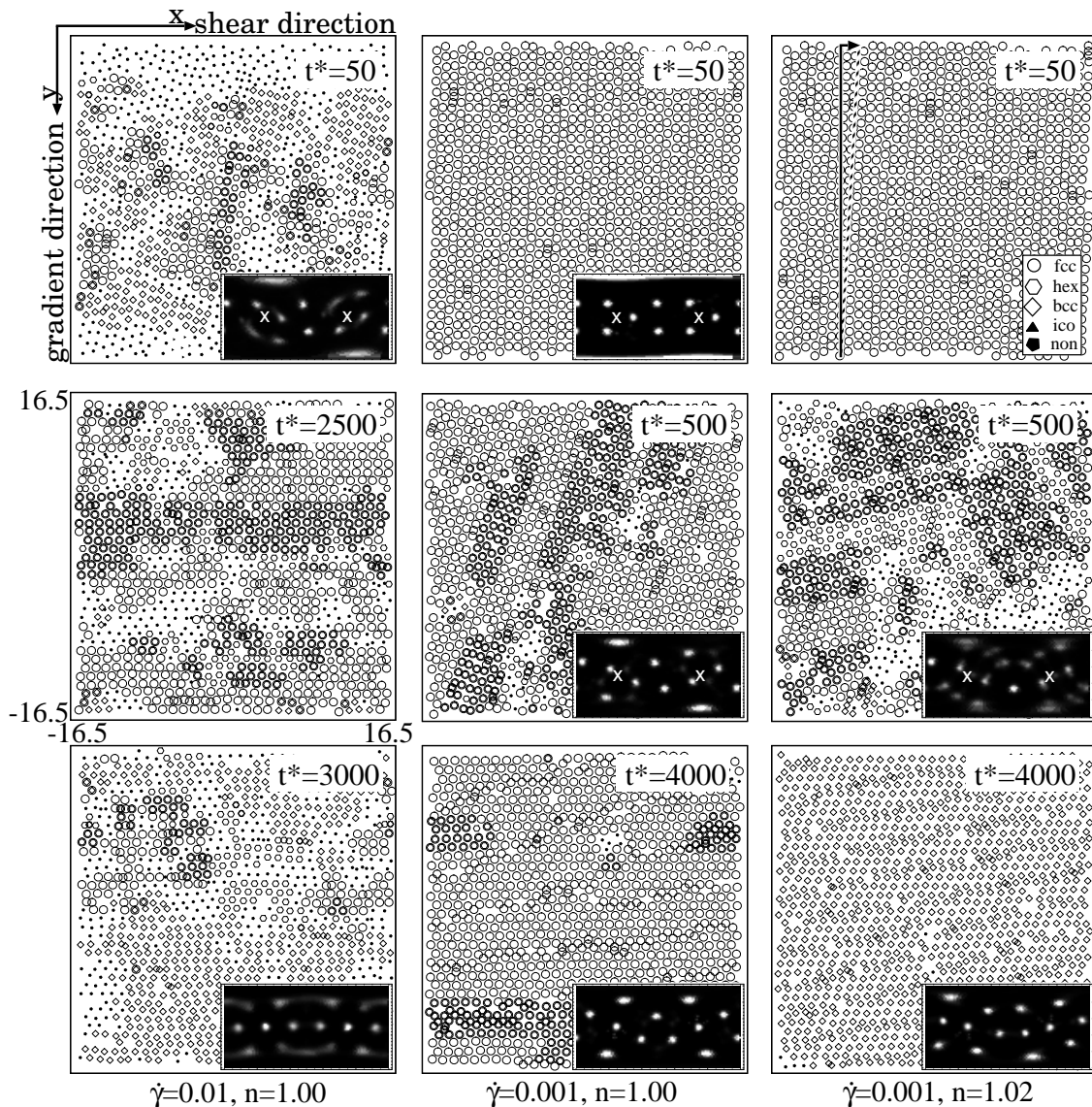
Figure 5.8: Snapshots (via NEMD) visualizing the evolution of the GEAM crystal subject to steady shear deformation at different times. All quantities are expressed in LJ units. The number of particles is $N = 43000$, temperature $T = 0.02$. Each slice is one length unit wide. Snapshots for two different shear rates $\dot{\gamma} = 0.001, 0.01$ and densities $n = 1.00, 1.02$ are presented. The type of local structure is indicated. The start configuration is the ideal fcc structure, shearing started at $t = 0$. The directions of shear and gradient directions are indicated in upper right picture. The insets contain the angular distribution of closest neighbors, where the representation is such that the shear direction projects at points denoted with $\times$ and the plane normal to flow gradient direction projects on a line (of length 2π) connecting the $\times$-points.

corresponding plane and direction in a bcc structure are (110) and [111], respectively.

Shear deformation inherently generates defects since atoms can move oblique to the shear direction to reach some close-by energetically preferred states and therefore prevent the shear stress from relaxing. Even when stationary flow is reached, shear
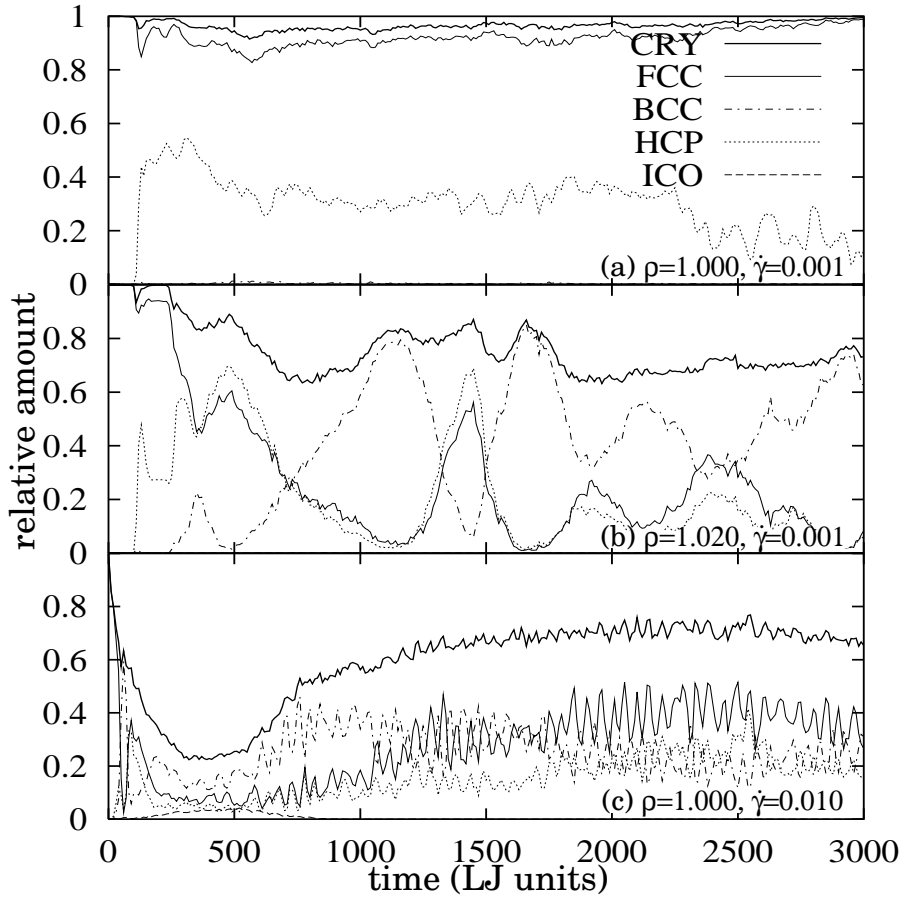
Figure 5.9: Transient behavior of the relative volumes occupied by fcc, bcc and hcp structure, together with the volume occupied by the amorphous icosahedral structure (ICO), obtained via NEMD, for GEAM at two shear rates $\dot{\gamma} = 0.001, 0.01$ and densities $n = 1.00, 1.02$. The bold curve (CRY) represents relative volume occupied by the three crystalline structures together. Domains with different crystal structures can overlap, thereby the total amount of crystallinity (CRY) is not a sum of relative volumes occupied by fcc, bcc and hcp structure. Time is given in standard LJ units and the number of particles is $N = 43000$, temperature $T = 0.02$. Starting configuration is the ideal fcc structure, shearing started at $t = 0$.

in the the direction oblique to the shear flow is observed leading to deviations from a stationary shear flow profile. The influence of the defects formed in stationary flow on structure, pressure tensor and self diffusion will be further discussed in Sec. 5.6.

The boundary condition imposes a further constraint on the newly formed crystal structure. Crystal planes tend to contain a multiple of unit crystal cells between the boundaries of the system. This results in a small deviation between densely packed planes and plane normal to the flow gradient, which may increase the probability for the appearance of defects. Several system sizes are studied to make sure that the presented results are not artificially caused by finite size effects.

For $\dot{\gamma} = 0.01$ the structure of the system changes between randomly close packed (fcc and hcp) and bcc, Fig. 5.9. The total amount of crystallinity is almost constant.

The bcc structure is produced by a volume conserving Bain transformation [17] of parts of the fcc structure. This process is reversible. The reason for such a behavior should be larger amount of energy introduced into the system at the higher shear rates. The fcc and hcp structures have the same energy per particle in the limit of low temperatures and occur always together as randomly close packed structures. Though one could expect to observe an identical amount of fcc and hcp structures, in current simulations the fcc structure shows up to be dominant. The explanation should be that the hcp structure allows shearing only in a single plane and that it is less resistant to defects, as compared to fcc. At higher densities and temperatures the bcc structure becomes dominant. This structural transformation between fcc and bcc structure under shear and in equilibrium will be further analyzed in the following section.

5.5   Phase diagram

The condition $p_{\text{solid}} = 0$ is used in Eq. (5.1) to estimate the area of mechanical instability $n(T)$ due to internal attraction of the GEAM metal under shear in a nonequilibrium phase diagram, see Fig. 5.10. Cracks – several crystal constants wide – are observed for small densities and low temperatures, see Sec. 5.6.3. The constant volume condition prevents their growth. The upper three (solid) curves in the nonequilibrium phase diagram for GEAM, show melting temperatures with and without shear. Shear-induced melting is observed at temperatures above $T \approx 0.04$. In equilibrium, the system melts at temperatures above $T \approx 0.045$.

In Figure 5.10 the bold dashed curve separates the densities and temperatures where at low shear rates ($\dot{\gamma} = 0.001$) bcc or fcc structures are found to be dominant. In the limit of low temperatures the preferred structure can be calculated directly from Eq. (2.1). At high temperatures the bcc structure is observed at densities and pressures, where the fcc structure dominates at lower temperatures. The crystal structure formed under the influence of shear exhibits a large shear stress compared to the one in the liquid metal. It appears that under the steady shear flow the structure with minimal free energy replaces the initial crystal configuration. The shear deformation determines the orientation of the structure: the stationary state crystal structure is oriented to minimize the resistance to the shear flow (cf. Sec. 5.3 and 5.4). The shear deformation in this picture weakens the influence of the boundary conditions. The fcc-bcc transition happens at pressures of the order of yield stress that are unaccessible for unconfined metals (see Fig. 5.11). The thermal quench of crystal structure formed under combined effect of high pressure and temperature could be reason for formation of the hardened layers in rail.

Transformations of crystal structure from one solid phase into the other solid phase are usually triggered in nature by temperature, volume or pressure changes. These structural transformations usually result from the competition between internal energy (or total energy of the system) and entropy. In order to estimate the effect of the given structure (fcc, bcc) on the stability of systems for which the temperature and the volume are fixed at prescribed values, one has to consider the Helmholtz free energy $F(T, V) = U - TS$ [20]. The internal energy U of the system is defined as a sum of
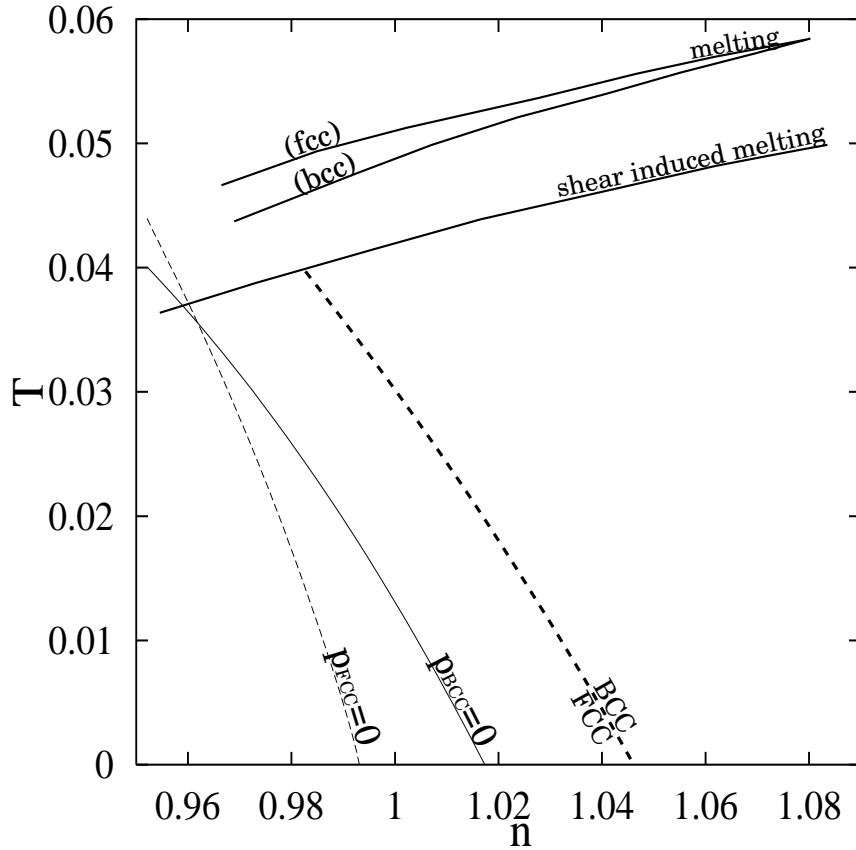
Figure 5.10: Structural phase diagram of GEAM in the temperature-density plane for two shear rates $\dot{\gamma} = 0.001, 0.01$. All quantities are given in the dimensionless reduced units. The bold dashed curve separates the densities and temperatures where at low shear rates ($\dot{\gamma} = 0.001$), the bcc or fcc structure is dominant. The area where the system is mechanically unstable due to internal attraction is estimated by inserting Eqs. (5.1) in condition $p^{\text{iso}} = 0$. The upper three (solid) curves show the melting temperatures with and without shear.

potential and kinetic energies, cf. Sec. 3, and thus directly available from the molecular dynamics (MD) simulations. Concerning the absolute entropy S, however, there is no such basic recipe. A simple route to estimate the entropy for this system is by considering the vibrational entropy of a one harmonic oscillator [22]. The crystal lattice with N atoms is represented through $3N$ independent one dimensional oscillators with frequency ω, mass m, momenta p_i and amplitudes of oscillations q_i analog to the Einstein model for heat vibrations in crystal, cf. Ref. [74]. The Hamiltonian of this system is

$$H = \sum_{i=1}^{3N} \left(\frac{p_i^2}{2m} + \frac{1}{2} m\omega q_i^2 \right) + E_0, \tag{5.3}$$

where E_0 is the potential energy of the system in the limit of low temperatures, calculated from Eq. 2.1. By inserting this Hamiltonian into the expression for the partition
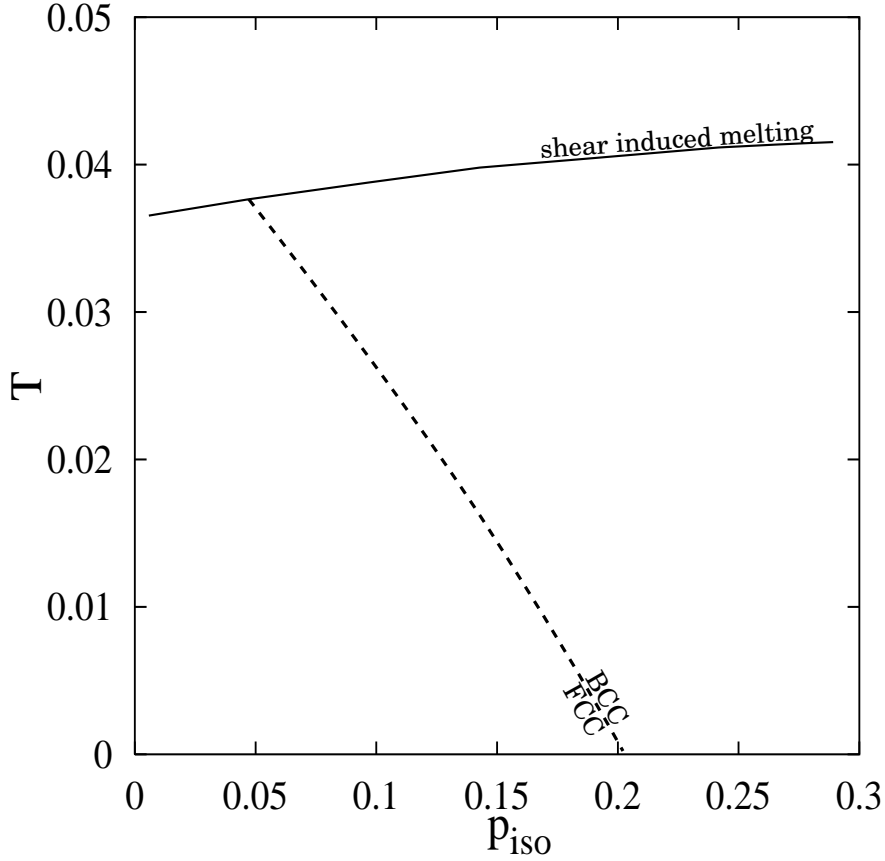
Figure 5.11: Structural phase diagram of GEAM in the temperature-pressure plane for two shear rates $\dot{\gamma} = 0.001, 0.01$. The bold dashed curve, separates the densities and temperatures where at low shear rates ($\dot{\gamma} = 0.001$) bcc or fcc structure is dominant. Upper solid curves melting temperatures with shear. All quantities are given in dimensionless reduced units.

function Z, one obtains

$$Z = \frac{1}{h^{3N}} \int d^{3N}q\, d^{3N}p\, e^{-H/k_\mathrm{B}T} = \left(\frac{k_\mathrm{B}T}{\hbar\omega}\right)^{3N} e^{-E_0/k_\mathrm{B}T}, \tag{5.4}$$

$$F = -k_\mathrm{B}T \ln Z = -3k_\mathrm{B}T \ln\frac{k_\mathrm{B}T}{\hbar\omega} + E_0/N \tag{5.5}$$

for the values of partition function and free energy, respectively. The vibrational entropy is then calculated from the free energy as

$$S = -\left(\frac{\partial F}{\partial T}\right)_\mathrm{V} = 3k_\mathrm{B}\left(1 + \ln\frac{k_\mathrm{B}T}{\hbar\omega}\right). \tag{5.6}$$

The frequency ω is related to the heat capacity by

$$C_\mathrm{v} = \left(\frac{\partial U}{\partial T}\right)_\mathrm{V} = T\left(\frac{\partial S}{\partial T}\right)_\mathrm{V} = 3\hbar\omega. \tag{5.7}$$

Using the above relationships, the frequency ω is obtained from MD simulation data presented in Fig. 5.12. Generally one expects a larger vibrational entropy for the bcc

structure compared to the fcc structure, since it is less densely packed. With increase of density the heat capacities of both structures decrease, see Table 5.2. At very high number densities ($n > 1.044$), where the bcc structure is the preferred structure at all temperatures, the heat capacities of the bcc and fcc structure are approaching the same value.
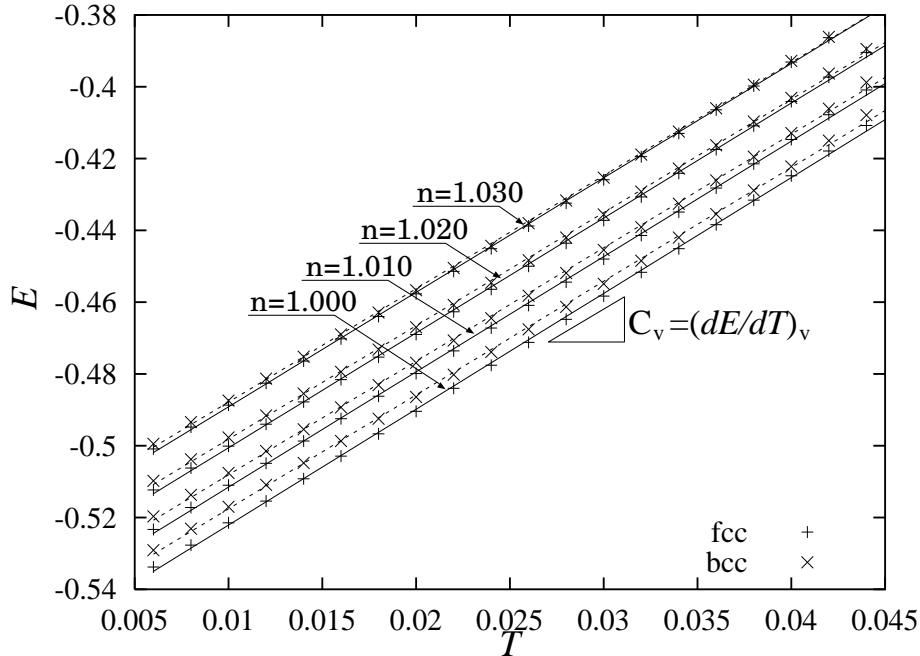

Figure 5.12: Internal energy of the system as function of temperature for different densities $n = 1., \ldots, 1.03$ (all in reduced units). To increase readability of figure the values of energy for successive densities are increased for $\Delta E = 0.01$. Molecular dynamics (MD) simulation results for E are denoted with $+$ (bcc configuration) and $\times$ (fcc). The curves are interpolated through NEMD data; their slope represents heat capacity.

A crystal structure possessing the lower frequency ω (softer lattice) will have the larger vibrational entropy. As a result, its free energy decreases faster with the increase of temperature. For this reason the bcc structure becomes stabilized due to the higher value of its entropy. In the limit of low temperatures, according to Eq. (5.5), the structure with larger energy per particle (E_0/N) is the thermodynamically stable structure. Though simple, this model is able to qualitatively represent the dependence of the free energy on the temperature, cf. Fig 5.13. It also predicts that the fcc-bcc structure transformation is a first order phase transition. Still, the assumption that all atoms in the crystal lattice oscillate with the same frequency is a very crude approximation. The

n	0.98	0.99	1.	1.01	1.02	1.03	1.04	1.05	1.06	1.07
fcc	2.30	2.28	2.22	2.21	2.20	2.19	2.18	2.17	2.17	2.15
bcc	2.26	2.23	2.17	2.16	2.16	2.15	2.15	2.15	2.15	2.14

Table 5.2: Heat capacities C_v of bcc and fcc crystal structure obtained form MD data (cf. Fig. 5.12) for different values of density $n = 0.98, \ldots, 1.07$ in reduced units.
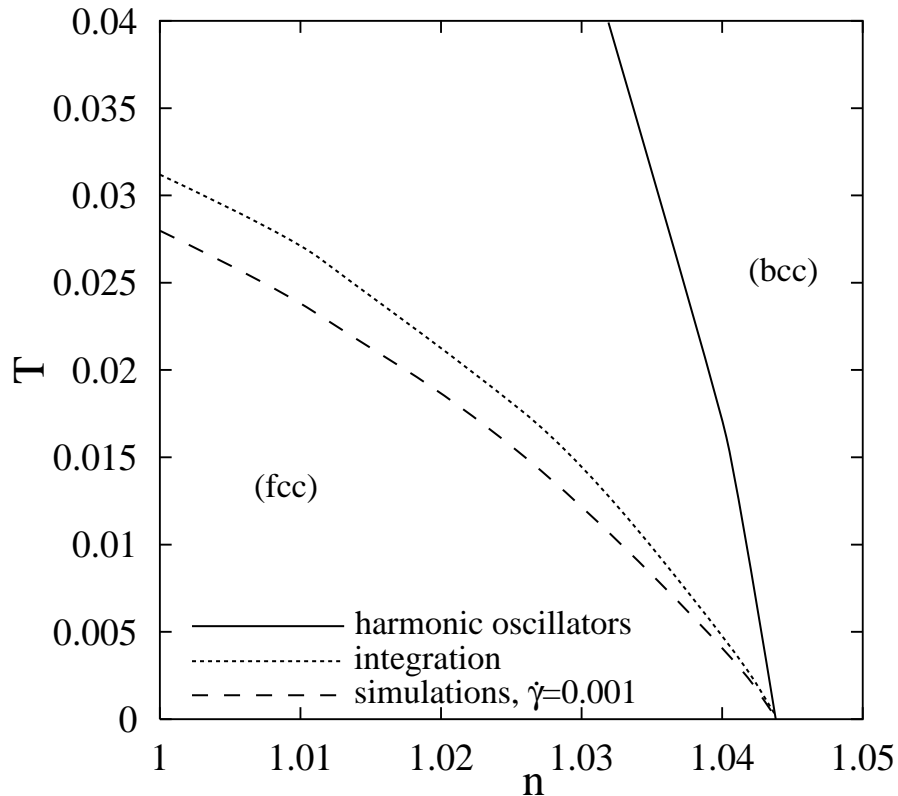
Figure 5.13: Structural phase diagram of GEAM in the temperature-density plane calculated via harmonic oscillator approximation, thermodynamical integration and from NEMD simulations of shear flow with $\dot{\gamma} = 0.001$. All quantities are given in dimensionless reduced units.

GEAM metal does not consist of harmonic oscillators and cannot be fully represented using a single frequency.

From positional correlation matrices obtained from MD simulation instead of a single frequency [21] it is possible to obtain a better estimate of the vibrational entropy. The diagonalization of the correlation matrix gives inverse quadratic eigenfrequencies of the system which can be used to calculate entropy. With this method the vibrational entropy can be calculated from a single simulation run. The disadvantage is that determinants of the large correlation matrices have to be calculated. So for example, for a system with $N = 10976$ atoms one should calculate the determinant of a 32928×32928 matrix. This would require large amount of memory and computational time. For this reason, another method is applied here, which the gives change of the free energy during the the Bain transformation from MD simulation data [22, 101].

The 'thermodynamic integration' technique provides a work-around and estimates the difference between free energies of two phases. The Gibbs relation

$$dF = -PdV - SdT \tag{5.8}$$

quantifies how changes in volume and temperature affect the Helmholtz free energy. The basic idea is to transform, via MD, the fcc solid into a bcc solid along the Bain
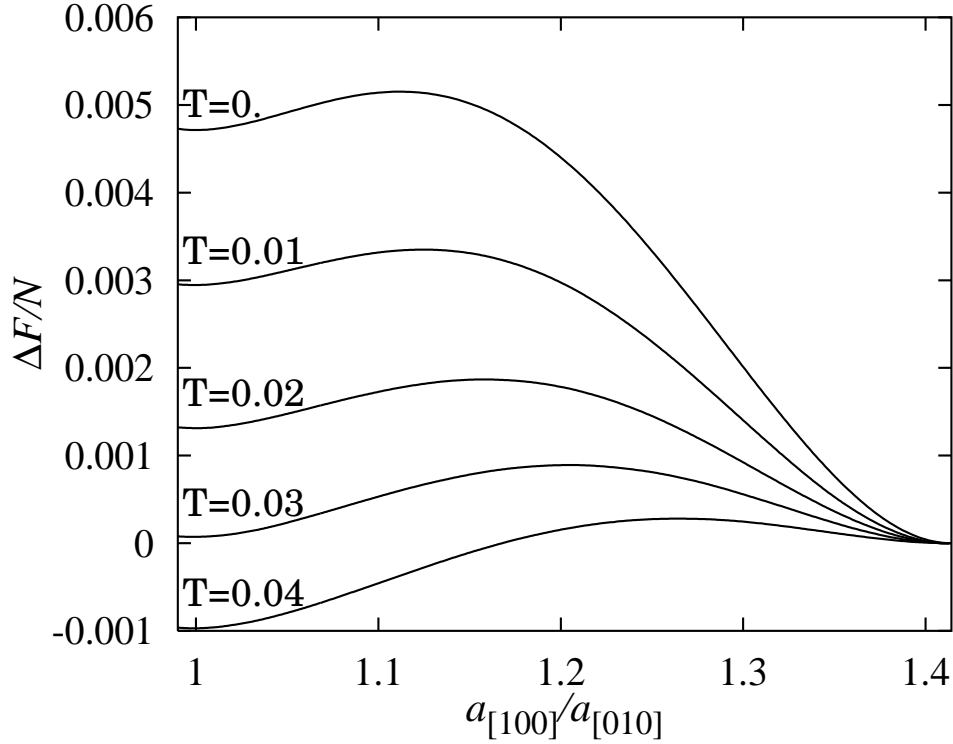
Figure 5.14: Change of the free energy vs. ratio $a_{[100]}/a_{[010]}$ during uniaxial volume conserving Bain transformation. The transformation of the ideal GEAM metal lattice is presented for temperatures $T = 0.01, \ldots, 0.04$. Both fcc and bcc structures correspond to local minima of the cohesive energy with respect to the ratio $a_{[100]}/a_{[010]}$.

transformation path at constant temperature [22, 101]. Then, the change of the free energy dF is

$$dF = -P_{xx}A_x dx - P_{yy}A_y dy - P_{zz}A_z dz, \tag{5.9}$$

where P_i are diagonal, cartesian components of the pressure tensor $(i = xx, yy, zz)$ and A_λ denote surface areas orthogonal to these directions. Figure 5.14 shows the change of the specific free energy $\Delta F/N$ along the Bain transformation path at number density $n = 1$ and temperatures $T = 0, \ldots, 0.04$, calculated via MD.

In the limit of low temperatures, the structure with the larger internal energy is the thermodynamically stable one. Here the bcc structure $(a_{[100]}/a_{[010]} = 1)$ corresponds to a local, the fcc structure to global minimum. A larger entropy for the bcc structure compared to the fcc structure is expected, since bcc is less densely packed. Accordingly, the free energy of a bcc structure should decrease faster with increasing temperature. At sufficiently high temperature the local minimum at $a_{[100]}/a_{[010]} = 1$ can evolve into a global one. This is indeed observed for the GEAM metal, cf. Fig. 5.14, for temperatures $T > 0.03$. In Fig. 5.15, thermodynamical integration is applied to calculate the structural phase diagram for GEAM in the temperature-density plane. The diagram shows regions where bcc and fcc structures are energetically favored, and data for two values of the two body interaction parameter $e_{AA} = 0.5, 1.0$. The thermodynamical integration also provides the size of the potential barrier between two structures along the transformation path. This barrier is small in magnitude ($\Delta \approx 4 \times 10^{-4}$) compared
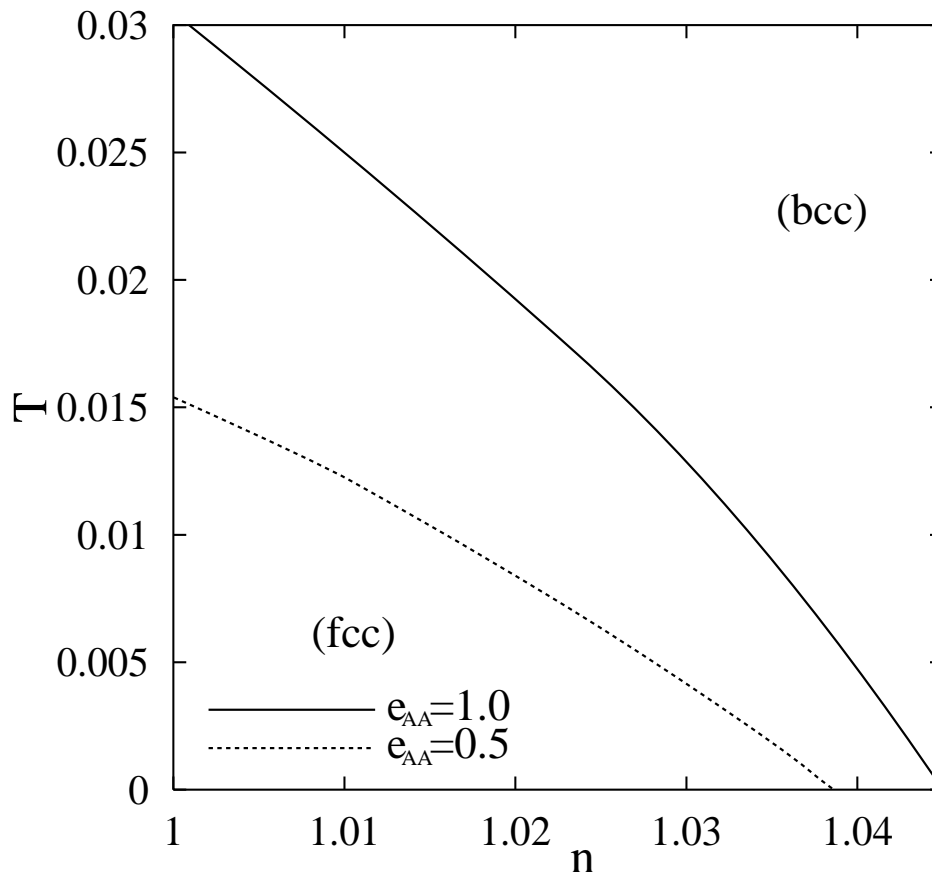
Figure 5.15: Structural phase diagram of GEAM in the temperature-density plane calculated via thermodynamical integration from NEMD simulation data. The curves separate densities and temperatures where bcc and fcc structures are energetically favored for two values of the two body interaction parameter $e_{AA} = 0.5$ (dashed line) and 1.0 (bold). All quantities are given in dimensionless reduced units.

with thermal fluctuations at room temperature. Nevertheless the bulk material stays in the bcc structure after rapid cooling since the structural transformation away from this state would involve collective motions of atoms. The bulk material, free of defects, cannot cross this barrier due to the thermal fluctuations even at high temperatures. Under shear flow, however, the material can sufficiently accumulate strain energy and cross this barrier, while relaxing to an energetically more preferred state as soon as the external field is released.

5.6 Wear and alloying at metal contacts

In this section the results are presented for three different types of metal-metal contacts subjected to shear. While the two materials are characterized by e_{AA}, w_{AA} and e_{BB}, w_{BB}, respectively, the interface is characterized by the strength of the binary interaction parameters e_{AB} and w_{AB}. First the "homogeneous" case of a clean, and dry, metal-metal contact is studied, where all the six interaction strengths are equal and set to unity (Sec. 5.6.1). Here, the interface arises due to initial conditions. In order to understand
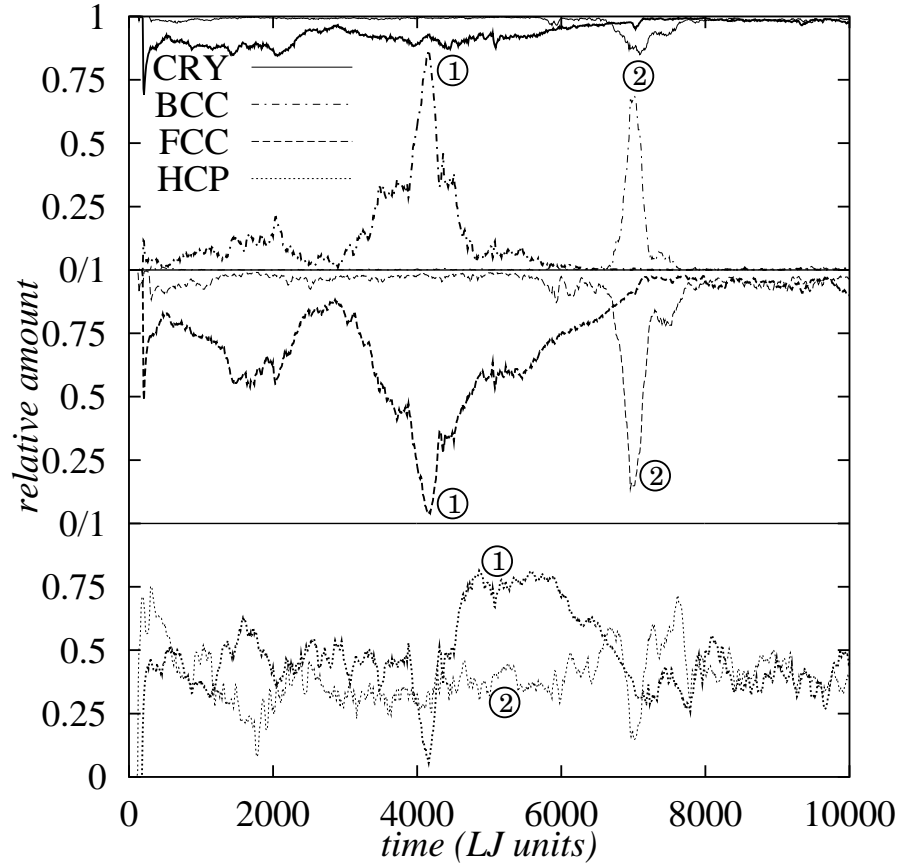
Figure 5.16: Relative volumes occupied by fcc, bcc and hcp structure vs. time. The bold curve CRY represents relative volume occupied by all three crystalline structures together obtained via non-equilibrium molecular dynamics simulation for homogenous GEAM metal subjected to steady shear. In starting configurations particles are placed at the ideal fcc lattice sites with the axes x, y, z corresponding to [100],[010],[001] (ticker curves, ①) and [111], [$\overline{1}\overline{1}$1], [1$\overline{1}$0] (tinner curves, ②) directions in fcc lattice.

the effect of the interaction strengths on the dynamical behavior, two inhomogeneous cases are studied upon varying a single interaction strength in both cases. In Sec. 5.6.3, atoms of different model metals feel an extra attraction due to the embedding term and $w_{AB} \neq 1$ is chosen. In Sec. 5.6.4 two materials with different shear moduli are in contact, i.e., $e_{BB} \neq 1$ is set (while keeping $e_{AB} = e_{AA}$).

For all three cases, a contact zone at relative motion in x-direction, with a load and shear gradient in y-direction is simulated. The temperature $T = 0.01$ and density $n = 1$. are held constant. The initial positions of the particles are fcc lattice sites, where axes x, y, z correspond to the directions in starting crystal configuration: [100],[010],[001] and [111], [22$\overline{1}$], [1$\overline{1}$0], denoted with ① and ②, respectively. Simulations are performed with $N_① = 43200$ and $N_② = 48668$ particles. In the latter case, the shear direction is orthogonal to the slip plane. The shear rate is $\dot{\gamma} = 0.001$. The shear deformation is switched on at $t = 0$. In the simulations of shear at the interface between two blocks of different metals, homogeneous GEAM configurations are used, presheared for 4000 time steps, as start-up. Each particles' type is set according to the side of the interface where

it resides at $t = 0$; type A is assigned to particles with negative y-coordinates. At the boundary in y-direction there is an artificial interface. Particles crossing this interface change type.
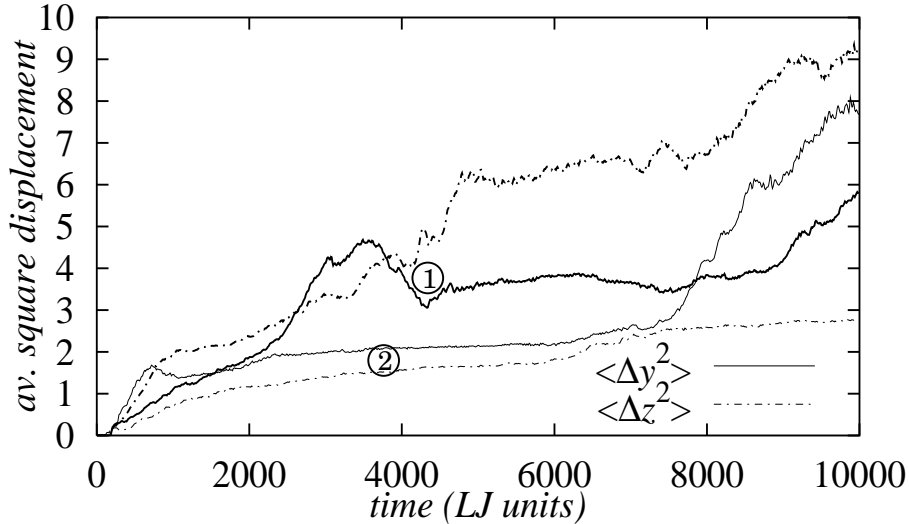

Figure 5.17: Average square displacements of particles in velocity gradient direction (y) and direction orthogonal to shear plane (z). In starting configurations particles are placed at the ideal fcc lattice sites with the axes x, y, z corresponding to [100],[010],[001] (ticker curves, ①) and [111], [$\overline{1}\overline{1}1$], [$1\overline{1}0$] (tinner curves, ②) directions in fcc lattice. All quantities are in standard LJ units.

5.6.1 Clean crystalline metal$_A$-metal$_A$ contact

First, dry solid friction between two blocks made of identical GEAM material is considered, i.e., $w_{ij} = e_{ij} = 1$ for all $i, j \in \{A, B\}$. After the shear deformation is switched on, the system responds with growing shear stress. After reaching a yield stress at $t_① = 180, t_② = 110$ (reduced units), a sudden increase of the amount of hcp structure is observed, as demonstrated in Fig. 5.16. Atoms move into the nearest potential minima, causing shear of the crystal planes in oblique to the shear flow direction. Layers of hcp structure are formed, and tend to block the flow. During continued shear significant structural changes start to appear. The rearrangement of the crystal structure is followed by an increase of self diffusion, or self mixing, of atoms. In Fig. 5.17, the average squared displacement of particles with respect to the shear gradient (y) direction and (vorticity, z) direction normal the shear x-y-plane is plotted. These quantities do not only define the diffusion coefficient, but also monitor the amount of interpenetration of particles across the interface.

After approximately 1000 time units a stationary structure is formed. The particles are packed in hexagonal layers stacked along the gradient direction to maximize the distances between particles as they shear past each other, and to reduce resistance to shear, cf. Sec. 2.2.1 and 5.4. For the chosen set of simulation parameters, fcc and hcp structures are stationary state structures (Sec. 2.2.1). In the course of the
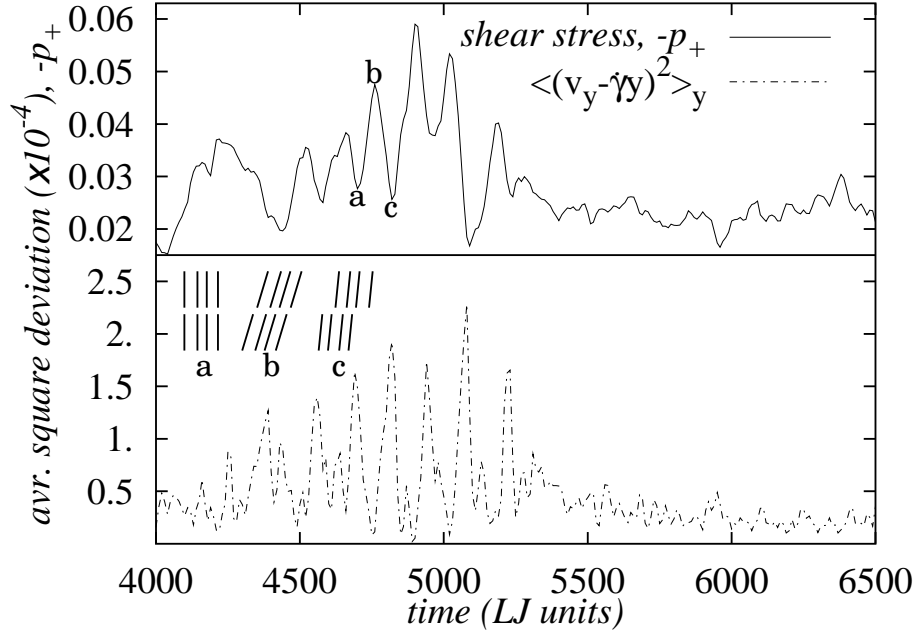
Figure 5.18: Insert of longer simulation showing stick-slip motion. Values for shear stress $(-p_+)$ and average square deviation of velocities from linear esults are obtained via NEMD with 48668 particles at density $n = 1.$, temperature $T = 0.01$ and shear rate $\dot{\gamma} = 0.001$. Non-equilibrium molecular dynamics simulation results for homogenous GEAM metal subjected to steady shear. In starting configurations particles are placed at the ideal fcc lattice sites with the axes x, y, z corresponding to [100],[010],[001].

structural rearrangement particles move in average for ≈ 1.3 reduced lengths units in shear direction, what is equivalent to ≈ 1.5 hexagonal layer distances. For the fcc structure the most densely packed planes correspond to the (111) plane, and slip occurs in $[1\bar{1}0]$ direction. The corresponding plane and direction in a bcc structure is $(01\bar{1})$ and [111], respectively. The shear direction is closely parallel, but definitely non-parallel, to the nearest neighbor (slip) direction of the newly formed structure, cf. Fig. 5.20 at $t = 6500$ for system ①. The shear direction projects onto the point $(\varphi, \theta) = (\pm\pi/2, \pi/2)$. A deviation between the steady state shear direction and the fixed flow direction results in a small increase of the average square displacement with time. If the particles are moving back in direction of their starting position (in y or z-direction), the average square displacement can also decrease. The long time self diffusion behavior, however, still remains unresolved within the actual simulation times.

Shear deformation inherently generates defects since atoms can move oblique to the shear direction to reach some close-by energetically preferred states. Even when a stationary flow situation is reached, defects blocking the flow are observed. These defects should be responsible for the difference between the observed amounts of hcp and fcc structures. Though they possess the same energy per particle in the limit of low temperatures, and occur together as randomly close packed structures, in our simulations the fcc structure shows up to be dominant. The explanation should be that the hcp structure allows shearing only in a single plane and that it is less resistant to
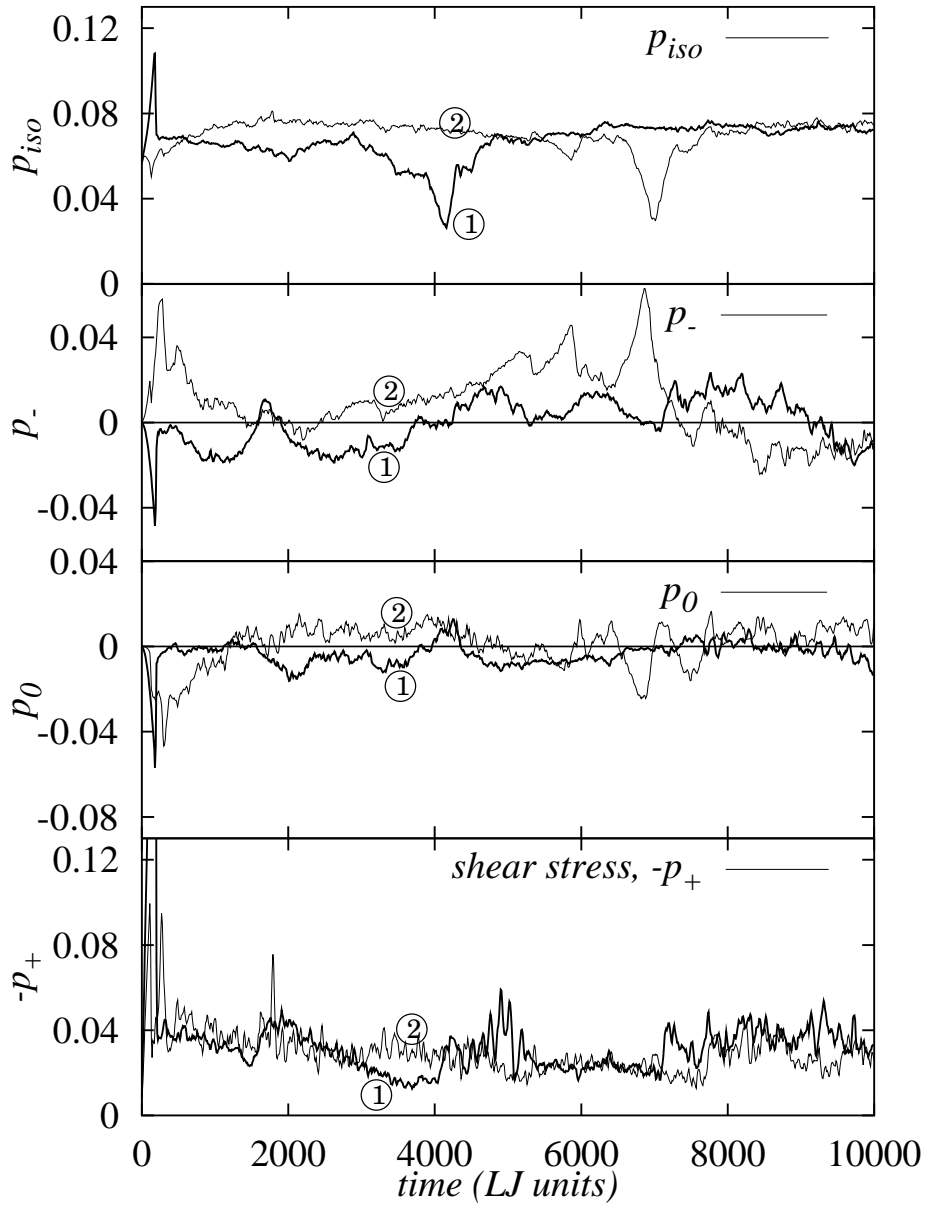
Figure 5.19: Evolution of the isotropic pressure p_{iso} and the three components of the anisotropic pressure tensor $p_{+,-,0}$ with time, cf. Sec.2.2.1 for definitions. Results are obtained via NEMD with 43200, and 48668 particles at number density $n = 1$, temperature $T = 0.01$ and shear rate $\dot{\gamma} = 0.001$ for a homogeneous GEAM metal subjected to steady shear. Initially, particles are placed at ideal fcc lattice sites with the axes x, y, z corresponding to [100],[010],[001] (thicker curves, system ①) and [111], [22$\bar{1}$], [1$\bar{1}$0] (thinner curves, system ②) directions in the fcc lattice.

defects, as compared to fcc. After a defect, partially or completely blocking the flow, is formed, parts of the system move as blocks. Shear stress is then released locally, yielding very high effective shear rates. The effective shear rates up to $10\,\dot{\gamma}$ are observed around $t = 5000$ in both systems, cf. Fig. 5.18. The material between blocks is moving fast in densely packed layers, and blocks are carried with the flow. Thus, the increase of
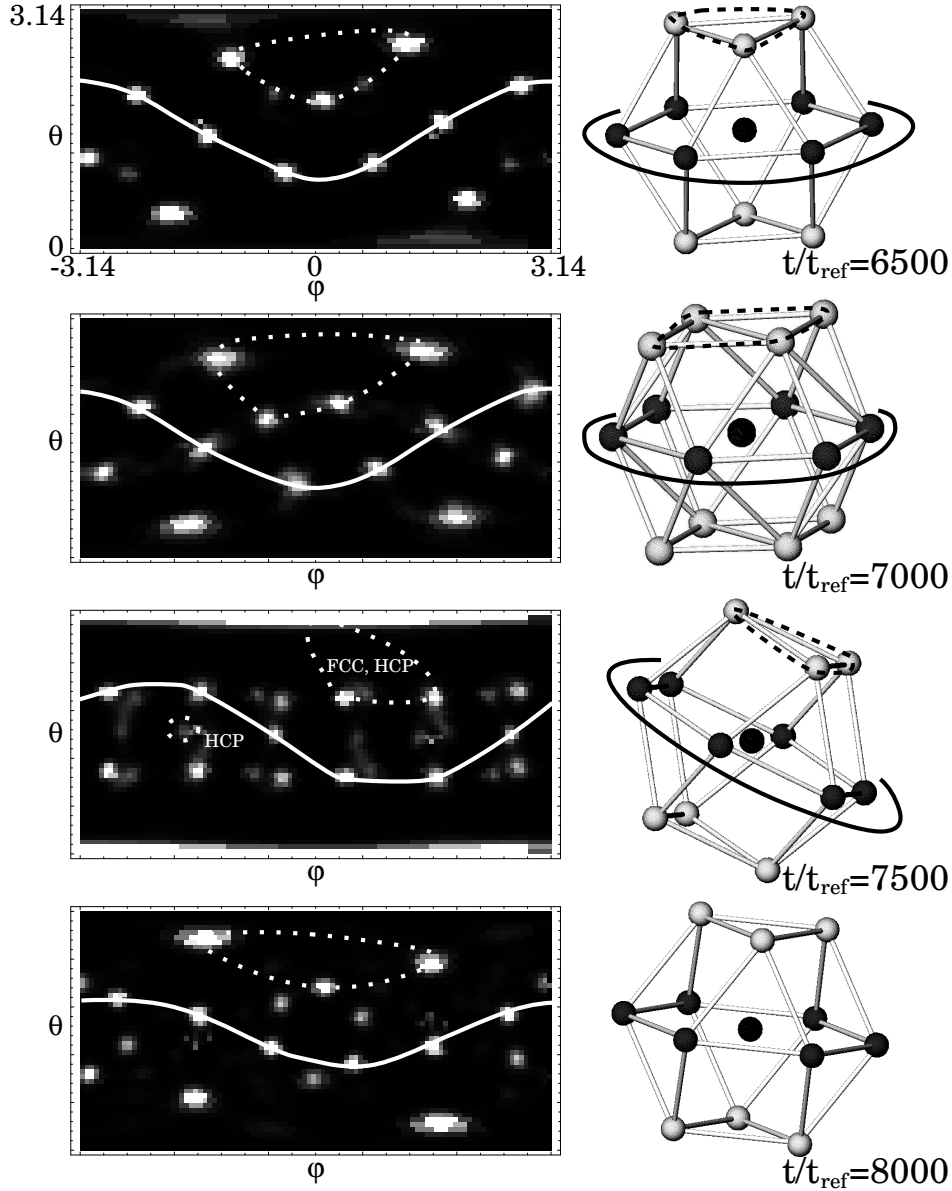
Figure 5.20: Angular distribution of directions to closest neighbors during the transformation between fcc and bcc crystal structures. Snapshots are obtained via NEMD with 43200 particles (system ①). Simulation parameters are: $T = 0.01$, $\dot{\gamma} = 0.001$ and $n = 1$. Starting configuration is the ideal fcc structure, the flow, gradient and vorticity directions correspond to $[111]$, $[22\bar{1}]$, $[1\bar{1}0]$ crystal directions, respectively. The nodes represent neighbors and they are connected with an edge if they are neighbors with themselves. Atoms in slip planes are marked by bold lines. In this representation, the shear direction projects at points $(\varphi, \theta) = (\pm\pi/2, \pi/2)$.

the effective shear rate alone does not result in larger average square displacements of particles. The quasi-periodic spikes of the shear stress and square deviation of the flow velocity from a linear profile indicate the existence of stick-slip motion in the system ①, cf. Fig. 5.18. The period between two spikes is ≈ 100 time units. During this process, in a first step the shear stress accumulates inside the blocks and the velocity
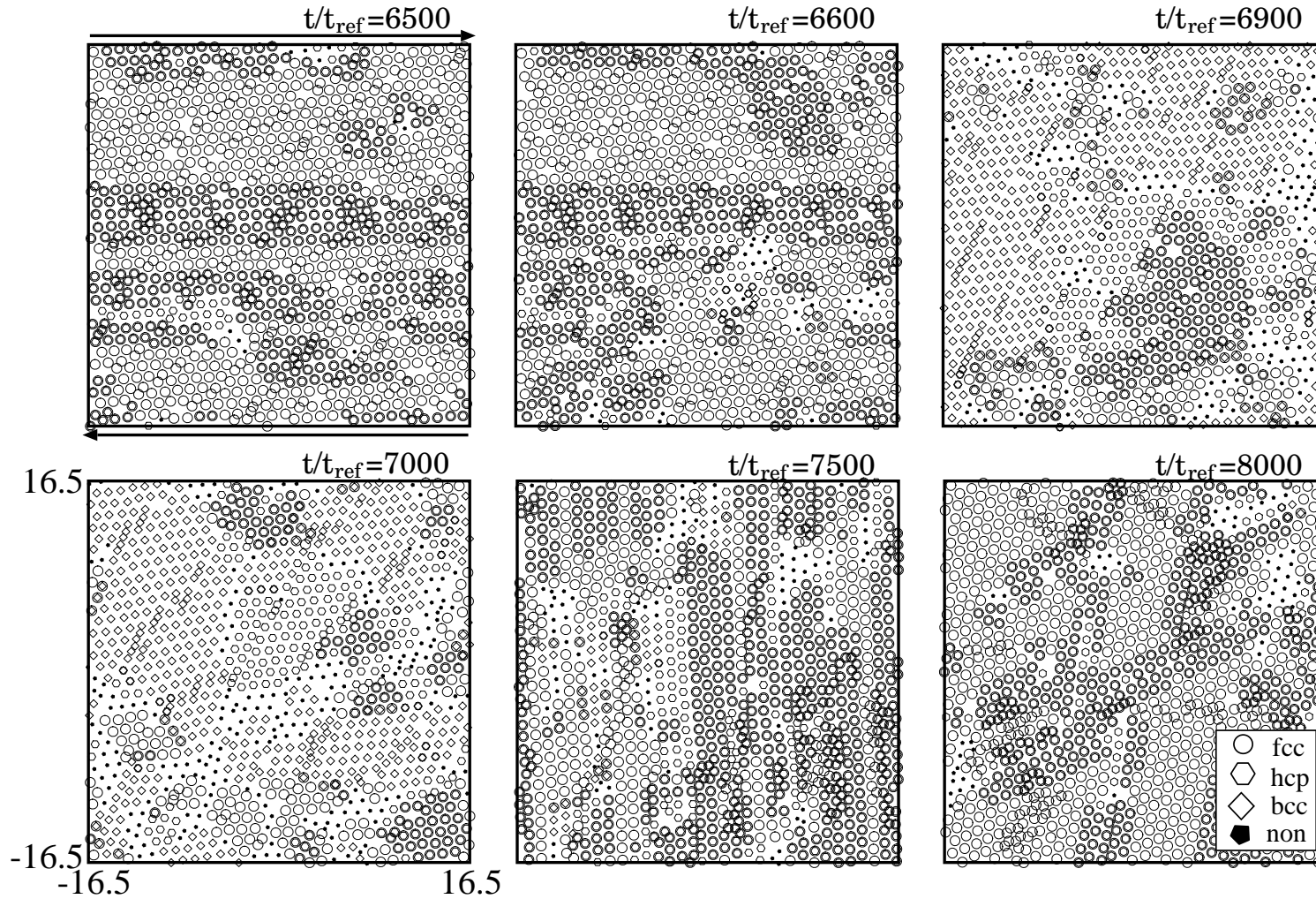
Figure 5.21: Snapshots visualizing the evolution of structure during temporary transformation of crystal structure from fcc into bcc. Snapshots are obtained via NEMD with 43200 particles (system ①). Each slice has a depth of unity. Simulation parameters are: $T = 0.01$, $\dot{\gamma} = 0.001$ and $n = 1$. The [111], [22$\bar{1}$], [1$\bar{1}$0] directions in the starting configuration, a fcc crystal lattice, correspond to shear flow direction, gradient direction and direction of normal to the shear plane, respectively. The type of local structure is indicated. The shear direction is indicated in the upper left picture. As before, all quantities are expressed in dimensionless LJ units.

profile is mostly linear. In a second step, after slip starts, the accumulated shear stress is released in a thin layer between blocks. Earlier simulations of dry sliding friction between a single Ni asperity and a Cu surface show similar behavior: kinetic energy is converted into potential energy and stored as "strain energy" [30]. Energy stored during stick is released to generate local phonons and later dissipated in the system. The stick-slip motion observed here is the property of those thin layers which interact strongly with the substrate [31].

The kinetic and potential contributions to the pressure tensor can be computed separately via NEMD. The kinetic part of the scalar pressure is, due to temperature control, given by $p_{\mathrm{kin}}^{\mathrm{iso}} = nk_{\mathrm{B}}T$ and of the order of the potential contribution to the scalar pressure. The kinetic contributions to the shear stress $(-p_+)$ and normal pressure differences $(p_{-,0})$, however, are negligible compared with the potential counterparts (of the order of $0.1\,\%$), as for dense fluids [117]. At $t = 6000$ an effective shear rate $\approx 2\dot{\gamma}$ are observed for both systems. Simultaneously, the shear stress and its fluctuations decrease. The explanation should be that different modes of collective motion of densely packed hexagonal layers yield different average shear stresses, see Sec. 2.2.1. Also, the existence of different shear modes should be responsible for slow changes of the shear stress in time. Normal pressure differences, however, are close to zero, and their behavior shows little connection with the intermediate flow properties. A change of the normal pressure differences is observed only if the system cannot globally adjust itself to accommodate shear deformation.

The normal pressure difference p_- increases sharply in Fig. 5.19 (thinner curve), after a defect is formed at $t = 6600$ in the system ②. Increase of p_- is followed by a structural transformation of parts of the fcc structure into bcc structure and a decrease of isotropic pressure. The isotropic pressure decreases since at the same temperature and density the bcc structure has negative isotropic pressure (cf. Figs. 5.16 and 5.19). Under structural transformation the original slip (111) plane/[$1\bar{1}0$] direction of the fcc structure transform into ($01\bar{1}$) plane/[111] direction, of the bcc structure, see Fig. 5.20. This structure transformation could not be simply classify into one of the basic mechanisms described in Sec. 2.2.1. The available results suggest, that both mechanisms are locally present. During the transformation of bcc structure back into fcc structure, parts of the system transform along several different directions. Snapshots of the system ② during the transformation (around $t = 7000$) are presented in Fig. 5.21 where domains with different structures can be observed. At $t = 7500$ the fcc structure is recovered, a number domains with different orientations are visible and the large-scale structure is oriented to block the flow, see Fig 5.21. These domains rotate with the flow (vorticity). After $t \approx 8000$, the system is again partially aligned with the flow but different domains are still visible, see Fig. 5.20. The rotation of domains is characterized by a steep increase of the average square displacement in flow gradient (y) direction, while the displacement in the neutral (z) direction is small. During 2500 time units domains move in y direction for ≈ 2.5 layer distances ($\langle \Delta y^2 \rangle \approx 5.4$). In Ref. [32], a similar behavior was observed for a two-dimensional embedded atom model metal-metal interface. The mixing of the material at the interface was closely related with the fine-grained microstructure, which is created during the shear.
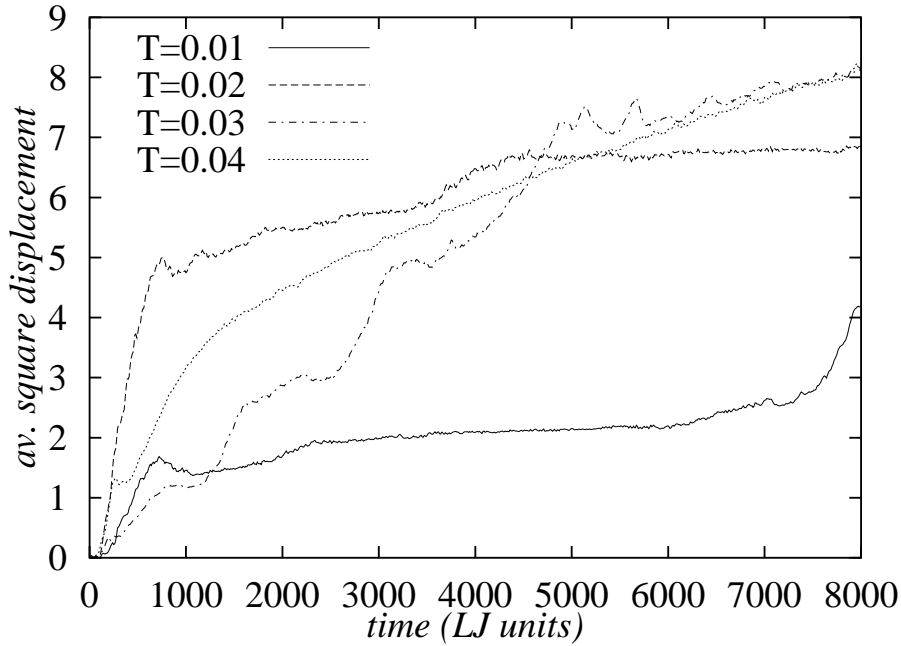
Figure 5.22: The evolution of average square displacement in shear gradient direction for temeratures $T = 0.01, 0.02, 0.03, 0.04$. Results are obtained via NEMD with 43200 particles at density $n = 1$. and shear rate $\dot{\gamma} = 0.001$. Shear deformation is switched on at t=0. Starting configuration was ideal fcc crystal lattice with [111], [$\overline{11}1$], [$1\overline{1}0$] directions corresponding to shear flow direction, gradient direction and direction of normal to the shear plane, respectively. All quantities are expressed in LJ units.

Average square displacement does not show dependence on temperature for simulated time scale, see Fig. 5.22. Even when system is close to melting point ($T/T_{\mathrm{ref}} = 0.04$) atoms are strongly bounded to their positions in hexagonal layers and average square displacement is fairly constant. For that reason, it is not possible study long time behavior of the average square displacement and calculate self diffusion coefficients at in this work simulated time scale .

5.6.2 Clean amorphous metal$_A$-metal$_A$ contact

Figure 5.23 shows results of a NEMD simulations of solid friction between two blocks made of the same GEAM amorphous material. Starting configurations is obtained by rapid cooling of melted metal from a temperature of approximately twice the melting temperature. The system is then relaxed for 2000 time units. The material responds with growing shear stress to the shear deformation immediately after $t/t_{\mathrm{ref}} = 0$. The yield stress is reached at $t/t_{\mathrm{ref}} = 90$ and system starts to flow. In contrary to case of crystalline contact described in preceding section, the linear velocity profile is immediately established. The value of the yield stress is ~ 10 times smaller then yield stress in case of crystalline configuration and differs very little from value of the shear stress in stationary flow regime.

During transformation of the amorphous structure, arrays of particles aligned with
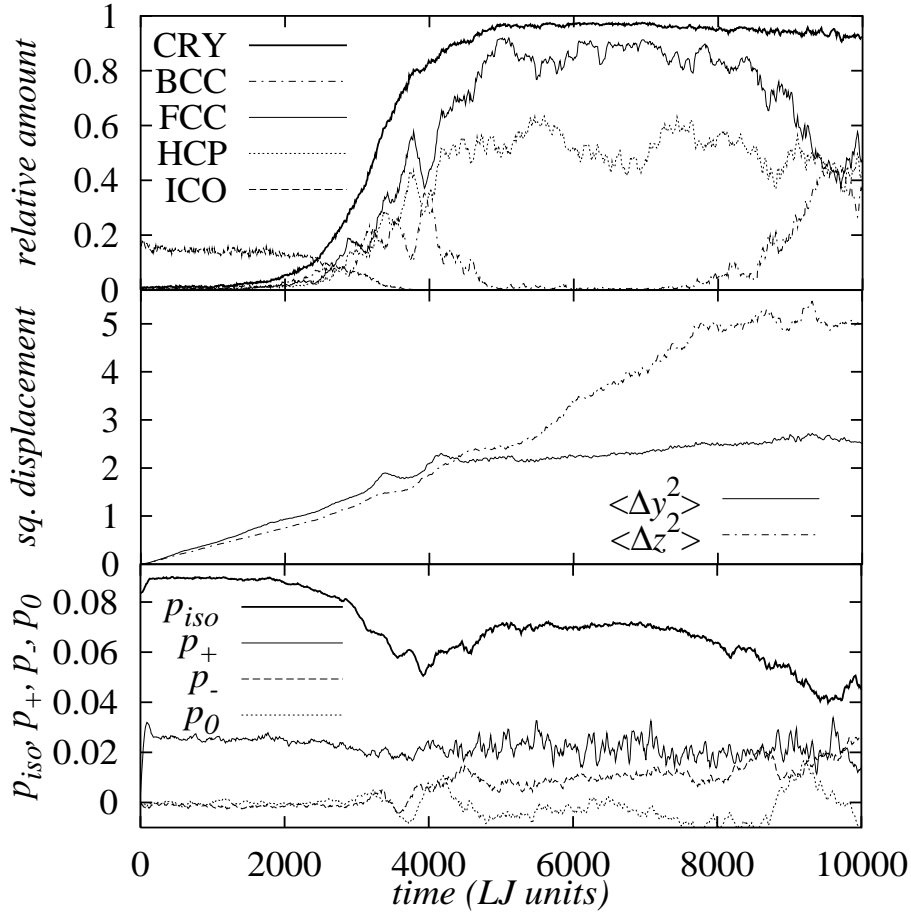
Figure 5.23: Evolution of relative volumes occupied by fcc, bcc and hcp crystal structures and amorphus icosahedral (ico) structure, average square displacements of particles, isotropic pressure p_{iso} and components of traceless pressure tensor $-p_+$, $-p_0$, and p_- with time. Results are obtained via NEMD with 43200 particles at density $n = 1.$, temperature $T = 0.01$ and shear rate $\dot\gamma = 0.001$. Non-equilibrium molecular dynamics simulation results for homogenous GEAM metal subjected to steady shear. Starting configurations is amorphous material obtained by rapid cooling of melted metal.

shear directions are formed. After 2000 time units first traces of crystalline structure are observed, at the same time amount of icosahedral structure decreases. The crystal structure completely fills simulation box at $t/t_{\rm ref} = 4000$. The transformation is gradual and slower then in case of crystalline initial configuration, since there was no local crystalline order before the shear started, cf. Sec.5.4. The particles move in average during the transformation for ~ 1.4 in both directions orthogonal to the flow direction. This indicates that despite amorphus structure of the material, self diffusion is small. Isotropic pressure and total potential energy decrease during the structure transformation while average value of shear stress $-p_+$ stays the same during the course of the simulation. This behavior can be explained, by mechanism described in Sec. 5.3: if model metal stays crystalline (during shear), it is to reduces energy per particle rather than to reduce resistance to shear. The normal pressure differences are very close to zero when material is in amorphous state. In crystalline state, different modes of collec-

tive motion are responsible for larger fluctuations of shear stress and values of normal pressure differences.
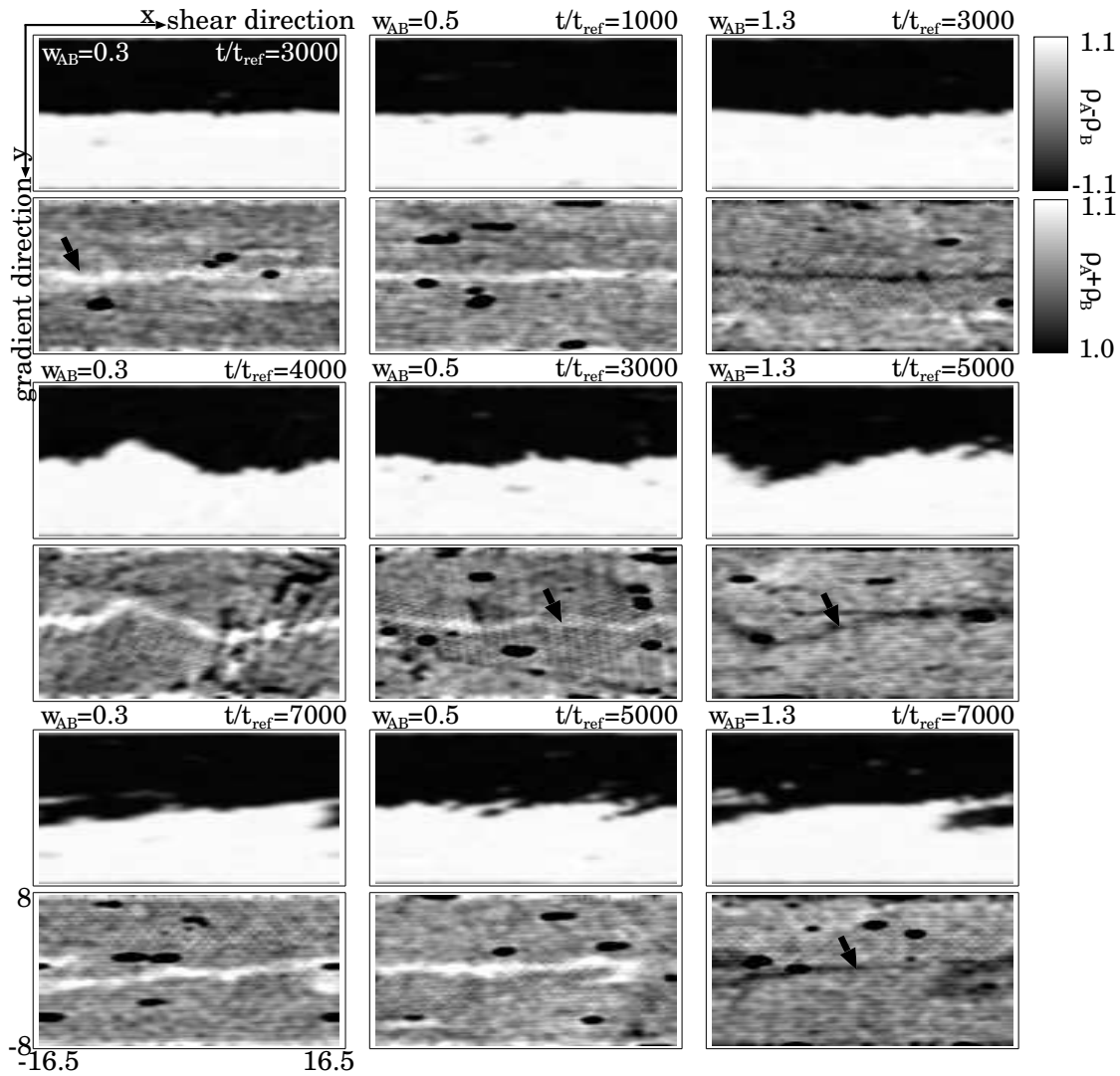
Figure 5.24: Cross-section of the embedding density close to the interface, averaged over a time period $\Delta t = 200$ for three values of the GEAM parameter w_{AB} (arranged in columns) and three different times (arranged in rows). The local density ρ is estimated from the sum of embedding densities of the two materials ρ_A, ρ_B, $\rho \approx \rho_A + \rho_B$ (lower, more structured, nine density plots). Embedding densities ρ_A, ρ_B are calculated for each type of particles separately for all points at a grid. To visualize and resolve inclusions and vacancies at the interface the quantity $\rho_A - \rho_B$ is used (upper density plots). The NEMD configurations are sampled after every 10 time units. Simulation parameters in LJ units are: $T = 0.01$, $\dot{\gamma} = 0.001$ and $n = 1$.

5.6.3   Contact with additional embedding interaction

If the interfacial embedding interaction parameter $w_{AB} \neq 1$ is different from the embedding interaction parameters within the bulk $w_{AA} = w_{BB} = 1$. the local density changes in the vicinity of impurities. The effect of this binary embedding interaction in the limit of low temperatures is discussed in Sec. 2.2.2. For GEAM, the local number density $n = N/V$ is close to the embedding density ρ calculated from Eq. 2.2. Figure 5.24 shows the the evolution of the number density $n \approx \rho_A + \rho_B$ within the interfacial layer between two model metals for $w_{AB} = 0.3$, 0.5, and 1.3 (three cases). Embedding densities ρ_A, ρ_B are calculated for each particle type separately for each point at a square grid. The interface, inclusions and vacancies formed during shear are visualized through the measure $\rho_A - \rho_B$.
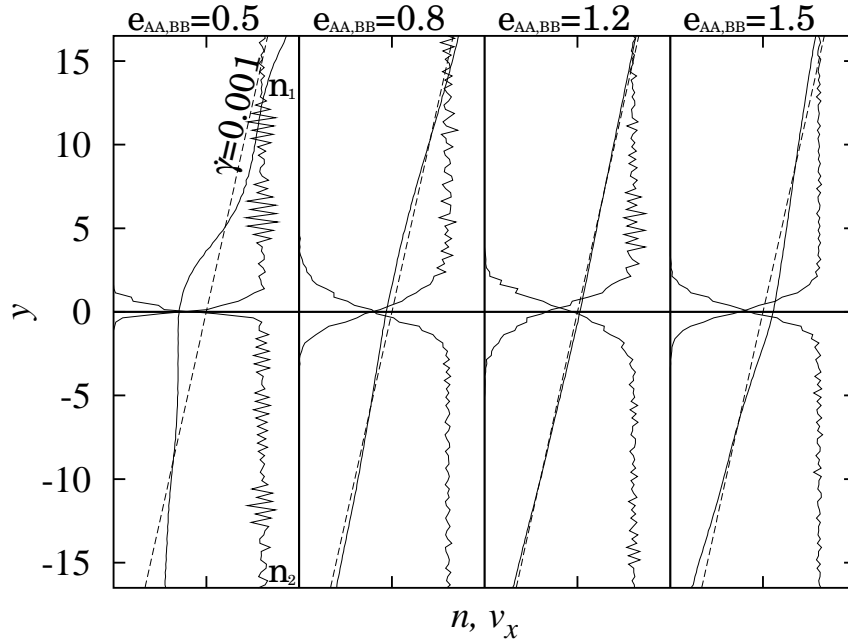
Figure 5.25: Mean flow velocity profile for cases, where two materials with different two body GEAM interaction parameters $e_{AA} = e_{AB} = 0.5$, 0.8, 1.2, and 1.5 (while $e_{BB} = 1$) are in contact. The four samples exhibit different ratios between shear moduli of the two interacting materials $G_1/G_2 = 0.5$, 0.8, 1.2, and 1.5, respectively. The velocity profiles are averaged over the time frame $t = 3000 - 7000$. All systems have 43200 particles. For the same systems sample density profiles for both types of particles are given at time $t = 6000$. The shear rate is $\dot{\gamma} = 0.001$ and temperature $T = 0.01$. All quantities are given in LJ units.

The density inside the bulk material is constant and similar in all these (three) cases. At the interface, changes in the local number density are observe . The system minimize the embedding energy locally by changing the embedding density such that it matches the desired embedding density, cf. Eq. 2.14. This results in an increase of the local density for $w_{AB} = 0.3, 0.5$ (light line in Fig. 5.24) and a decrease for $w_{AB} = 1.3$ (dark line). For $w_{AB} = 0.3$, after a defect – followed by Burgers transformation – is formed at $t = 7200$, the part of the system located around the contact plane starts to rotate

with the shear flow to form an inclusion. The microscopic inclusion produced in sliding penetrates for about 3 length units into the other material block. This process results in mechanical alloying at the interface since the parts of the inclusions move with different relative speeds in shear direction due to the flow gradient. For cross-sections taken at $t = 11000$ see Fig. 5.24. Similar behavior is observed for $w_{AB} = 1.3$. For $w_{AB} = 0.5$, the slip direction of the crystal structure is non-parallel with the interface. This leads to a gradual alloying of two materials parallel to the interface. In Fig. 5.24 can be also observed vacancies created during the shear flow as black spots in the $\rho_A + \rho_B$ density plots. Their vacancy is typically 2 atoms wide and has a life time between $50 - 400$ time units. They appear with and without defects and tend to be aligned with the flow.

Within statistical errors, an influence of the (additional) embedding interaction on the shear stress and normal pressure differences is not detected. This is plausible, because the interface occupies only a small portion of total volume and pressure tensor components reflect the material flow within the whole system.
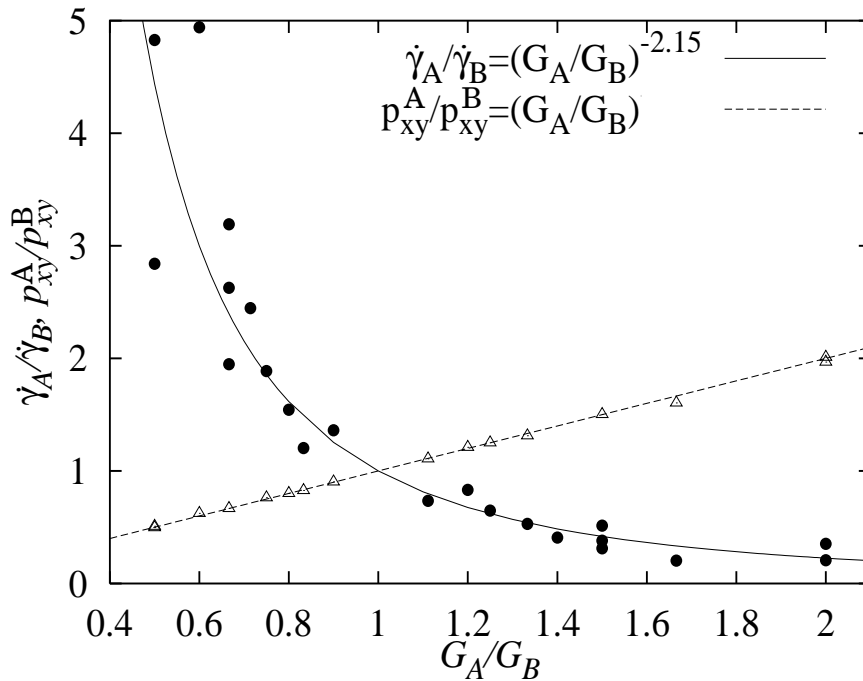
Figure 5.26: Dependence of ratios of effective shear shear rates $\dot{\gamma}_A/\dot{\gamma}_B$ and local shear stresses p_{xy}^A/p_{xy}^B from the ratio of shear moduli G_A/G_B in materials type A and B. Symbols denote averages from the simulation of an interface for shear rate $\dot{\gamma} = 0.001$ and temperature $T = 0.01$ with 43200 particles. The shear moduli is controlled via parameters e_{AA} and e_{BB}, $e_{AA} = e_{AB}$. The curve is interpolated through NEMD data.

5.6.4 Metal$_A$-metal$_B$ contact

The form of the EAM allows to systematically vary shear moduli, i.e., resistance to shear deformation, with strength of two body interaction parameters: e_{AA}, e_{AB}, and e_{BB}, see Sec. 2.2.2. Here is chosen $e_{BB} = 1$. (basic GEAM metal) and vary e_{AA}, while $e_{AB} = e_{AA}$. After onset of shear flow, an inhomogeneous shear profile is established, cf. Fig. 5.25. It can be observed that the mechanical alloying at interface depends on the shear moduli of the two materials. If the absolute difference between their shear moduli is large (here $e_{AA} = 0.5$ or $2.$), the shear is concentrated in the material with smaller shear modulus while the other material moves almost as a block. For this reason mixing of the two metals is observed only within a single hexagonal layer at the interface. If shear moduli are comparable (here $e_{AA} = 0.8, 1.2$) both materials penetrate for ≈ 3 hexagonal close packed layer distances behind the interface (here, after 8000 time units).

The dependence of the ratio of effective shear rates $\dot{\gamma}_A/\dot{\gamma}_B$ on the ratio of shear moduli G_A/G_B for metals A and B is presented in Fig. 5.26. A simple hyperbolic relationship between them is tested, where the coefficient is obtained via regression. Since the shear stress and moduli have the same origin (traced back to the shape of two body interaction potential), the observed ratio of shear stresses equals the ratio of shear moduli, i.e., $p_{xy}^A/p_{xy}^B = G_A/G_B$. It is found, that only the ratio of shear moduli influences the local shear stress and effective shear rate. This should be a consequence of the strong dependence of local shear stress on the mode of collective motion (amplitude of zig-zag motion, cf. Sec. 2.2.1).

The analysis of the crystal morphology at $t = 4000$ is presented in Fig. 5.27. In case $e_{AA} = e_{AB} = 0.5$, the bcc structure is the dominant stationary structure for metal$_A$ particles at $T = 0.01$ and $\dot{\gamma} = 0.001$. In the limit of low temperatures the fcc structure is preferred in metal$_A$. The difference between energies per particle in bcc and fcc structure, $(E_{c,bcc} - E_{c,fcc})$, decreases with the strength of the two body interaction parameter e_{AA}. In Ref. [17] it is shown, that the bcc structure can be additionally stabilized by entropy contributions to the free energy. To make this more visible the angular distribution of directions to next neighbors of dominant structures are also provided for two of the dominant structures on the right side of Fig. 5.27. It is visible that two-dimensional densely packed layers in bcc and fcc structures are parallel and shear such that they pass each other. In the two remaining cases, for $e_{AA} = e_{AB} = 0.8, 1.2$, the fcc structure becomes stationary within the whole system. Mechanisms of mechanical alloying are similar to the case of the additional embedding interaction ($w_{AB} \neq 1$). Again, a temporary transformation of parts of the system into bcc structure is observeed, cf. Fig. 5.27 for $e_{AA} = e_{AB} = 1.2$.
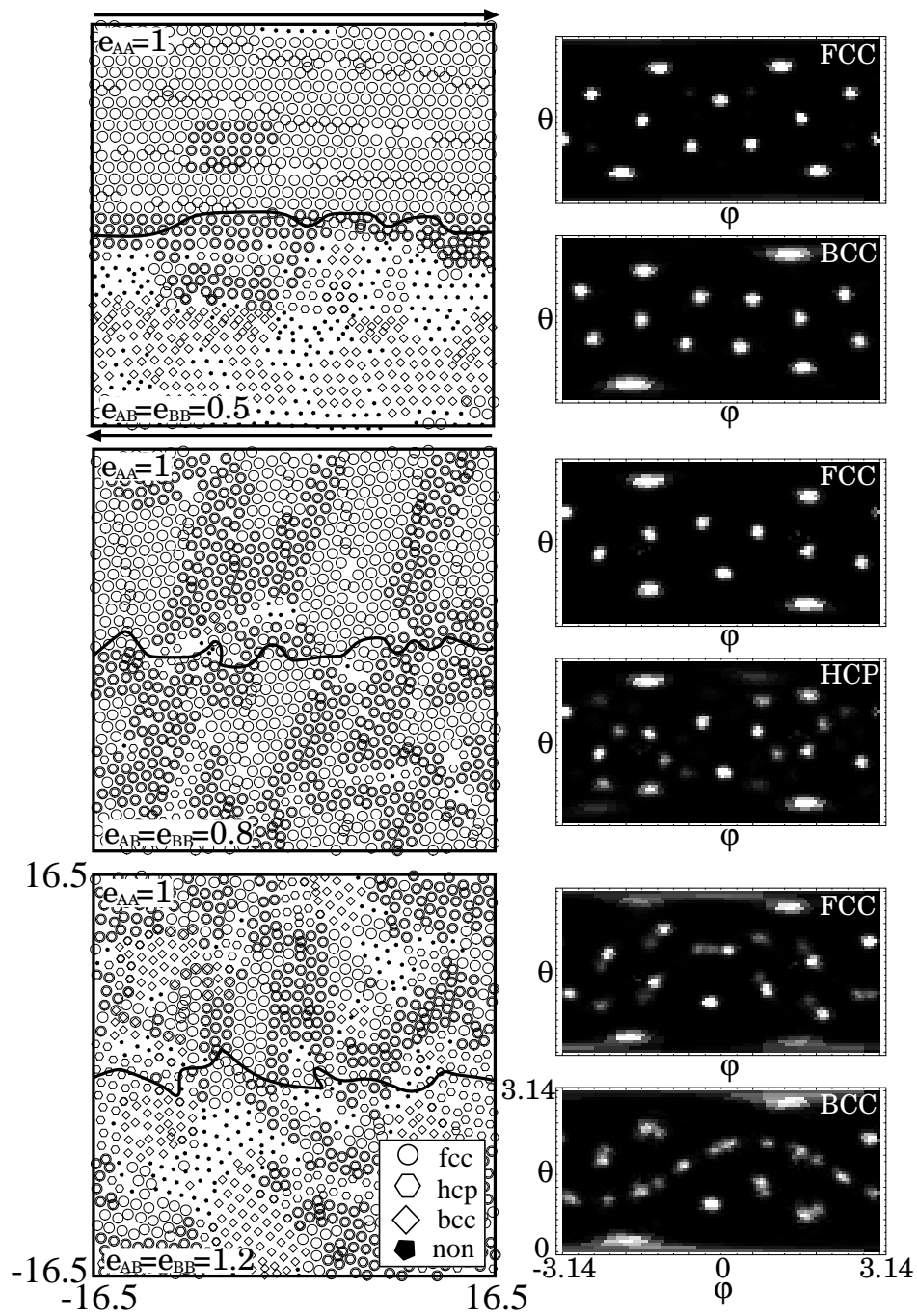
Figure 5.27: Snapshots structure (left) at interface of two materials with different shear moduli at $t/t_{\mathrm{ref}} = 4000$. Snapshots are obtained via NEMD with 43200 particles. Each slice is one length unit wide. The angular distribution (right) of directions to the closest neighbors is also given for dominant structure. All quantities are expressed in LJ units.

Chapter 6

Porous structures

6.1 Simulations of metallic foam wall rupture

Solid metal foams are usually produced by solidification of a liquid metallic foam. The latter is generated by the introduction of gas into a melt analogous to aqueous foams. This is achieved either by direct injection gases (air, nitrogen, argon) into the melt [44, 45, 46] or adding of a blowing agent to the melt [47, 48, 49]. The blowing agent decomposes under the influence of heat and releases gas, which then in return foams the metallic melt. The foaming process is stochastic and controlled only through the composition of the melt and process conditions. Insight into the foaming process is obtained by means of metallography, x-ray tomography, and small-angle neutron scattering [119, 120]. *In situ* observations during foam formation have been carried out using x-ray radioscopy [121]. Experimental investigations show a distribution of oxides throughout the material [122]. The optimization of production techniques until now has based on trail and error. In order to obtain a stable foam stabilizing forces must exist created by added particles or oxide films. If their content is low the resulting foam is not stable and shows significant drainage. Three mechanisms are assumed to play a role when the additional particles care present: i) reduce surface tension of the melt, ii) increase bulk viscosity and prevent flow, iii) create a network of fragments captured between the cells stabilizing the the cell walls [51, 123]. Also detailed analysis of experimental data revealed that there is critical rupture thickness of the cell walls: when a film is stretched below a thickness of about $50\mu m$, rupture occurs [51]. Recent numerical studies with lattice Boltzmann automata have provided a better insight into physics of foaming [52]. These methods allow to study the evolution of the foam. Yet this methods only partially resolves the mechanisms behind coalescence of bubbles in foam. The two bubbles grow together when wall thickness falls below some threshold value. Only with particle models, such as molecular dynamics or smooth particle hydrodynamics (SPH), the mechanisms governing foam stabilization can be numerically explored [40, 41, 42].

The current computer simulations aim at the characterization of the effects of material properties on rupture of foam walls, in order to test of a simple embedded atoms model for metals and to explore its range of application. The current study is restricted to model metal foam wall, where the effect of the characteristics are most transpar-

ent although the choice of parameters does not reflect any particular real experimental situation. The simulations does not include the influence of the blowing agent. The results should most likely help to explain the microscopic behaviors of foam walls during coalescence of two bubbles under microgravity conditions.
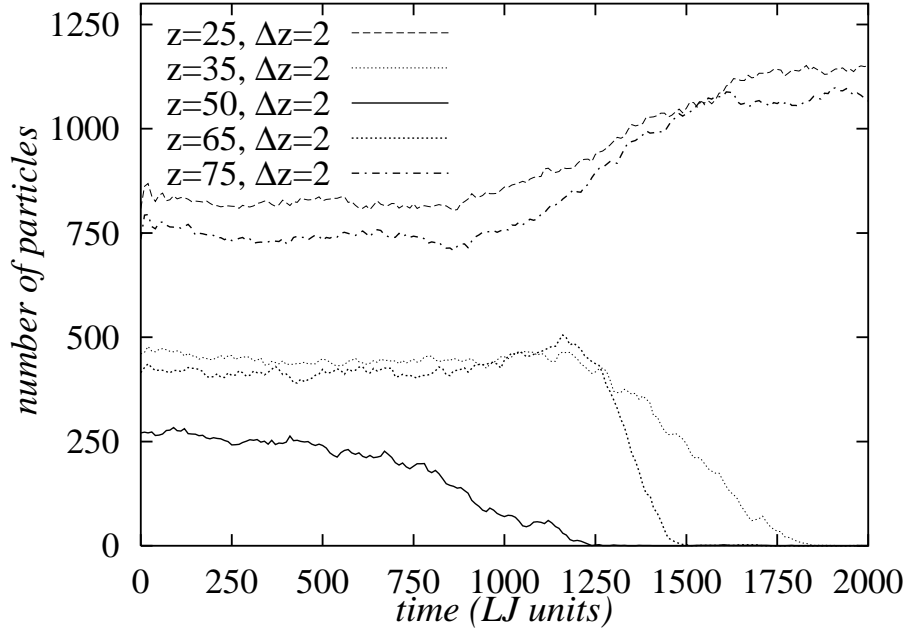

Figure 6.1: Drainage and rupture in the GEAM metal wall at T=0.025. The number of particles within different cross sections of the wall is presented. The GEAM metal is investigated with $F_2 = 1$. and $F_k = 0., k > 4$. Simulations are performed with $N = 58096$ particles for pore (ellipse) axes ratio $a/b = 1.75$. All quantities are expressed in LJ units.

The molecular dynamics simulation method is used to study the evolution of of metallic foam walls. Starting configurations is obtained by rapid cooling of a melted metal from a temperature of approximately twice the melting temperature. The atoms are then removed from the center of the system to create ellipsoidal shaped walls. The system is relaxed for 1000 time units, and after that heated again to a temperature above the melting point ($T_{melt} \approx 0.02$). A cubic simulation box with periodic boundary conditions is used. The dimensions of the simulation box throughout the work are 100x100x12 (width, height, length). In Figure 6.1, the evolution of the number of atoms inside $\Delta z = 2$. wide cross section normal to the foam wall is presented. The snapshots of the same system are given in Fig. 6.2. A GEAM metal is investigated with $F_2 = 1., F_4 = 12.$, and $F_k = 0.$ for $k > 4$, which has the energy pro particle to the vacancy formation energy ratio similar like real metals (cf. Sec. 2.2.1). Simulations are performed with $N = 58096$ particles for the pore (ellipse) axes ratio $a/b = 1.75$. At t=0. the sponge wall is approximately 10 nearest neighbor distances wide. First, the cell wall particles gradually drain towards the base of the wall and the number atoms decreases in the middle cross section of the sponge wall. There is a positive feedback effect: the number of atoms falls faster as the wall becomes thinner and the resistance to its contraction smaller. Due to the accumulation of atoms at the base of the wall

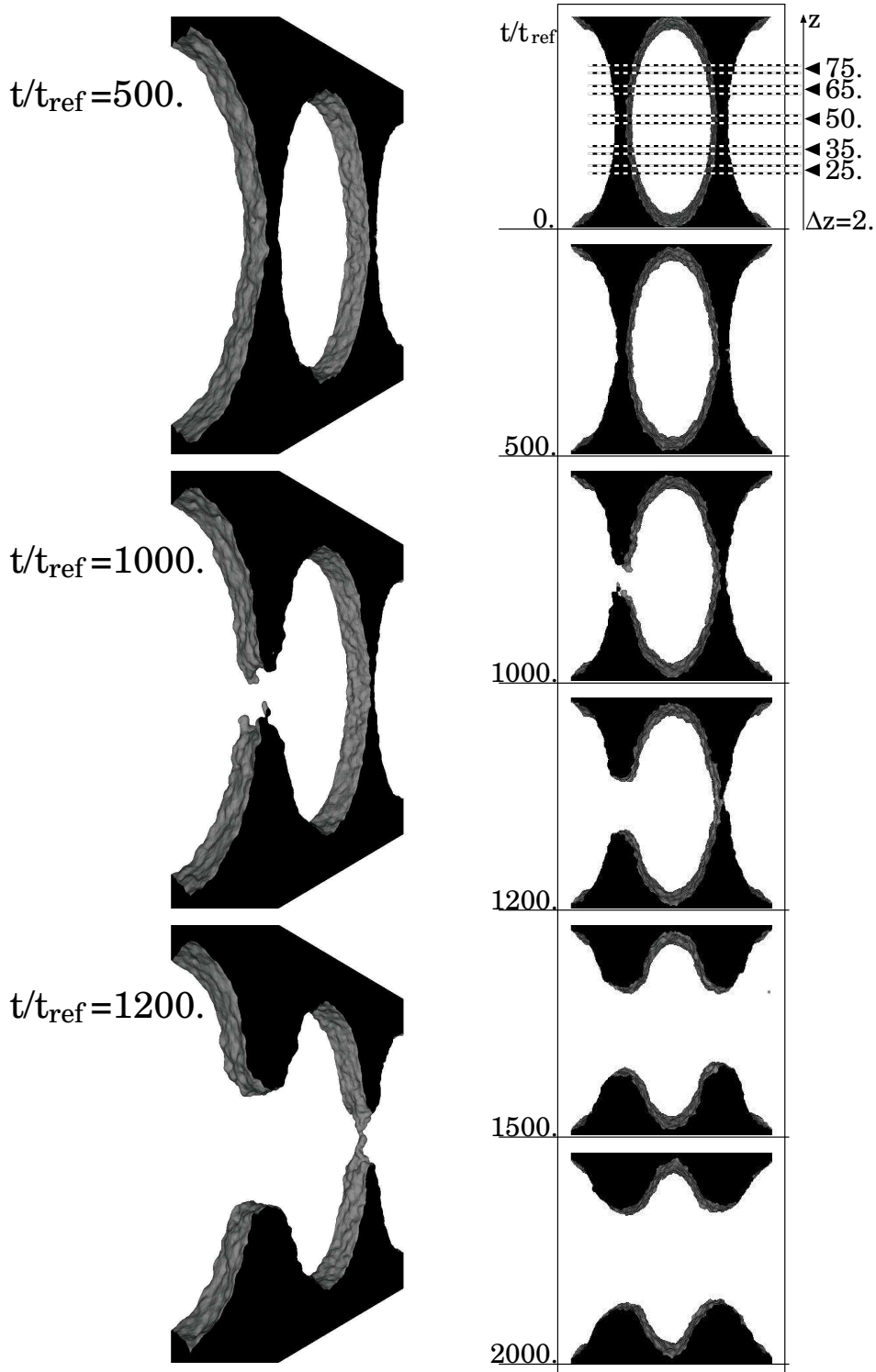Figure 6.2: Evolution of GEAM metal wall, drainage and rupture, at T=0.025 ($N =$ 58096, $a/b = 1.75$). The GEAM metal is investigated with $F_2 = 1.$, $F_4 = 12.$, and $F_k = 0.$ for $k > 4$. Snapshots are taken at $t/t_{ref} = 500, 1000, 1200, 1500,$ and 2000. Time and length scales are expressed in dimensionless LJ units. Black surfaces are cross section of the system with simulation cell.
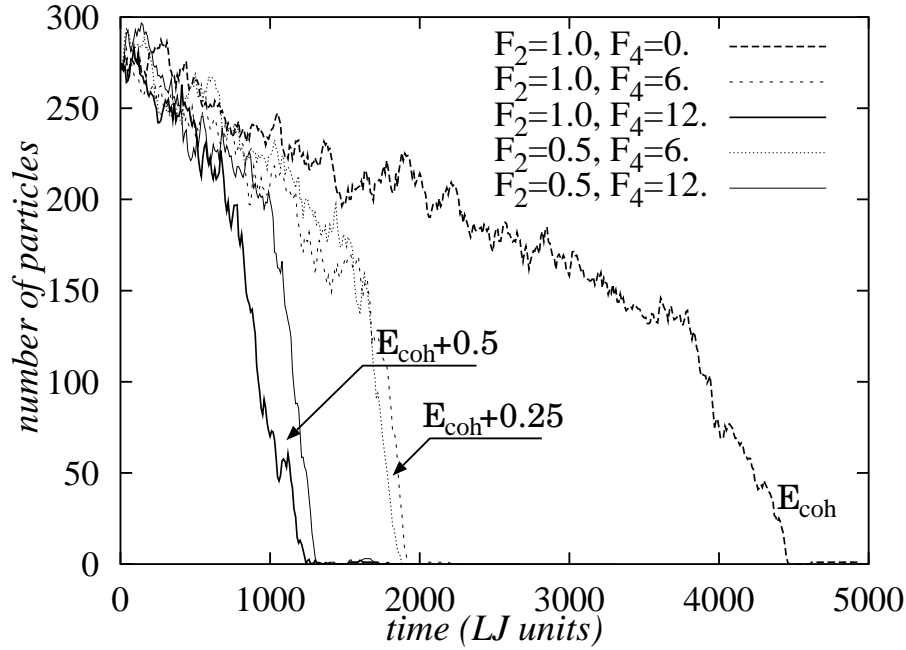
Figure 6.3: Rupture of the GEAM metal wall is investigated for different values of the energy per particle controlled via F_2 and F_4 parameters, while $F_k = 0.$ for $k > 4.$ at $T = 0.025$. For GEAM with $F_2 = 1.$ and $F_k = 0., k > 4$ surface energy is $E_{\text{coh}} = 0.552$. The number of particles within middle cross sections of the wall is presented. Simulations are performed with $N = 58096$ particles. The temperature is T=0.025 and the axes ratio $a/b = 1.75$. All quantities are expressed in LJ units.

number of atoms in lower (upper) cross sections rises. At the moment of cell rupture an avalanche-like contraction of the remaining parts of the wall is observed, since the surface tension tries to eliminate broken cell walls and to redistribute the additional melt (cf. Fig. 6.1 and $T/T_{\text{ref}} = 1500., 2000.$ in Fig. 6.2). When the thickness of the sponge walls is varied via axes ratio a/b. As expected, in the thicker wall there is more material and it needs more time to rupture, cf. Fig. 6.4.

The increase of energy per particle accelerates the rupture of the sponge wall, see Fig. 6.3. For GEAM with $F_2 = 1.$ and $F_k = 0., k > 4$ surface energy is $E_{\text{coh}} = 0.552$. The surface energy calculated for the crystalline state proves to be an unreliable estimate for the surface tension in the sponge wall, see Sec. 2.2.1. The observed influence of temperature is very small (Fig. 6.4). The reason might lie in the large value of the cohesive energy and thickness of the wall: the process was too fast for us to be able to resolve the differences. The modification of EAM potential described in Sec. 2.2.2, allows us to model foam wall with additional particles. The same initial configuration is used like in previous examples where the type of random chosen atoms is changed. A system is studied with $N_A = 58189$ and $N_B = 2900$ particles of type-A and B respectively. The $e_{AA} = e_{BB} = 1.$ are set and strength of two-body interaction particle-metal e_{AB} is varied. The case $e_{AB} = 1.$ corresponds to homogenous GEAM metal and $e_{AB} = 2., 4., 6.$ to two, four and six times stronger two-body interaction between the additional particle and the surrounding metal. The results of MD simulations are presented in Fig. 6.5.
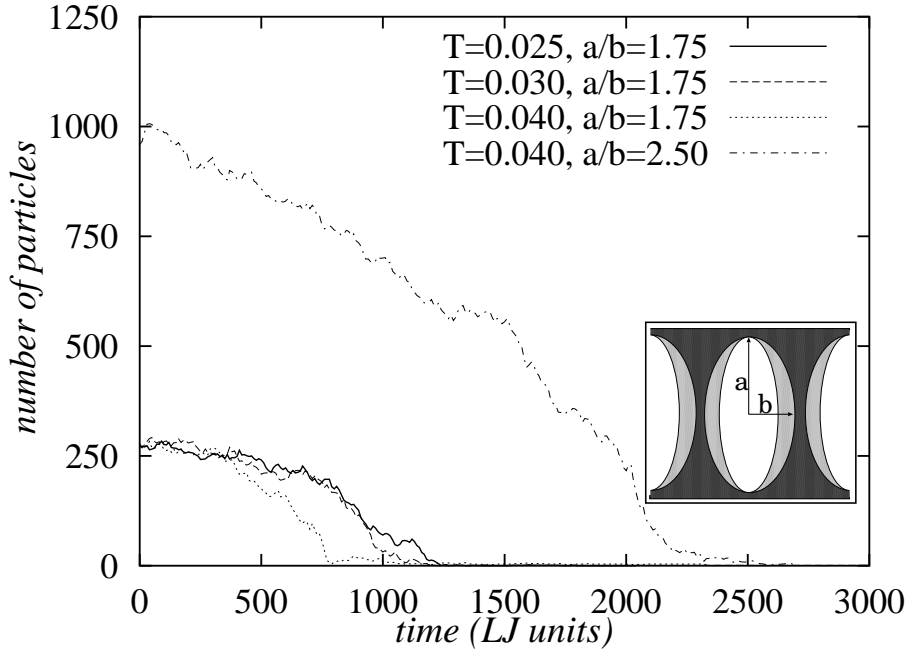
Figure 6.4: Influence of wall thickness and temperature on the drainage and rupture of the GEAM metal wall. The wall thickness is controlled via a/b ratio. Simulations are performed with $N = 58096$ particles. The temperatures are $T = 0.025, 0.03, 0.04$ and the axes ratio $a/b = 1.75, 2.5$. All quantities are expressed in LJ units.

The presence of additional particles slows down the rupture of the sponge wall and the life span of the wall increases with the strength of interaction between particles and metal. The effect increases with increase of e_{AB}.

Due to the generic choice of the model potential, the spatial coordinate of a particle may represent either the position of a "model ion" or the position of a spatially localized number of nuclei. One should note that the thermostat which controls the temperature in case of embedded atom mode, in the generalized case is a source of damping, dissipation of energy in the system (referred to also as viscosity). Temperature can be defined only for the case of embedded atoms, otherwise the parameter T is understood as a control parameter for the damping in the system, similar to artificial viscosity commonly

system (atoms)	r_{ref} (nm)	$E_{\mathrm{ref}}, k_{\mathrm{B}}T$	Γ_{ref} (erg/cm^2)	P_{ref}	t_{ref}
embedded atoms	0.24	3.45eV, 40kK	0.96		0.97×10^{-13}s
(8)	0.48	27.6eV	1.92		1.9×10^{-13}s
embedded (64)	0.96	0.2keV	3.83	40GPa	3.9×10^{-13}s
particles (500)	1.92	1.8keV	7.67		7.8×10^{-13}s
(4000)	3.84	14keV	15.3		0.97×10^{-12}s

Table 6.1: The values of reference units for length (r_{ref}), time (t_{ref}), energy (E_{ref}), surface energy (Γ_{ref}), and pressure and elastic moduli (P_{ref}). The number of atoms inside embedded particle is given in brackets. One should note that the temperature can be only defined for single atoms.
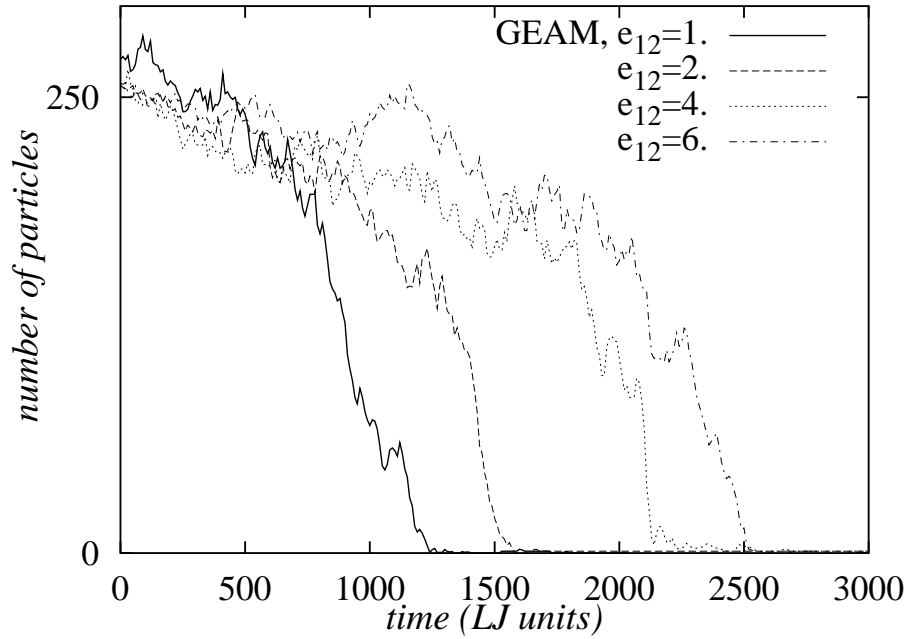
Figure 6.5: Influence of additional particles on rupture of the model metal wall. The GEAM metal is investigated with $F_2 = 1.$, $F_4 = 12.$, and $F_k = 0.$ for $k > 4$. Simulations are performed with with $N_A = 58189$ and $N_B = 2900$ particles of type-A and B respectively. The strength of interaction between aditional particles and metal is controlled via parameter e_{AB}. The temperature is $T = 0.025$ and the axes ratio $a/b = 1.75$. All quantities are expressed in LJ units.

used in mesoscale SPH method [42]. Reference values needed to compare dimensionless model quantities with experimental data are listed in Table 6.1. They are estimated using the procedure explained in Sec. 2.3.

In conclusion, the model metallic foam walls, described above, exhibit several interesting features which are realistic, such as: an increase of energy per particle in the whole system accelerates the rupture of the wall. In contrary, the additional particles bound surrounding metal particles creating a network and slowing drainage. This results in a slowing of the rupture. The evolution of the structure during the breaking is studied in detail. Still, the performed simulations are at nanoscale and direct comparison with the experiments is not possible. Even so, the results show plenty of phenomena which are experimentally observed for metal foams. This work demonstrates that particle mesoscale methods [40, 41, 42] could prove a very powerful tool for understanding processes taking place in foam walls.

6.2 GEAM metallic porous structures

The relation between the geometric microstructure of heterogenous porous media and transport properties of a fluid confined in it is important for a wide range of applications, such as the paper manufacturing, dialysis, osmosis, contaminant transport and geophysics [53, 54, 55, 56, 57]. However, many unsolved problems remain. Especially, an understanding of the relation between pore structure and its transport properties is lacking. An important aspect of research in this area is played by numerical simulation (see Ref.[53, 124]). Usually numerical simulations use models of the porous structures as input which can be roughly divided in two groups: reconstruction models, that attempt to reconstruct a realistic pore structure, and stochastic models, such as Boolean model, Voronoi tessellation and levelled-wave model [125].
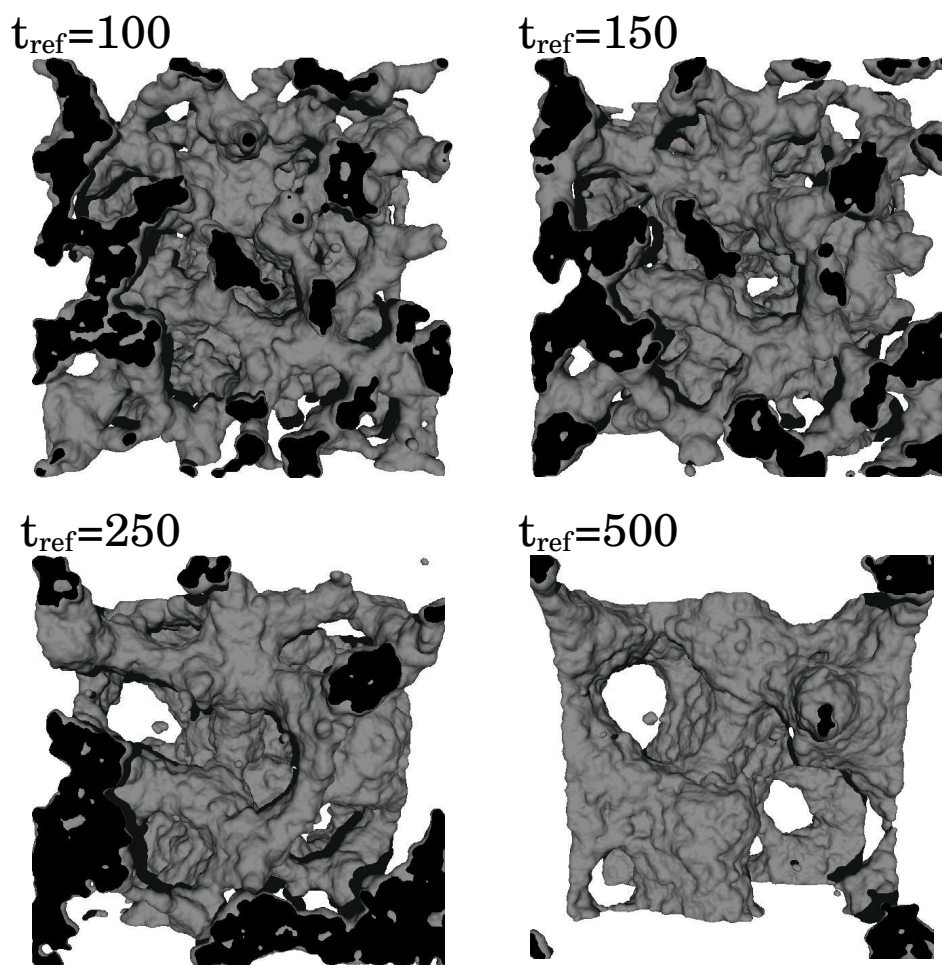
Figure 6.6: Equilibration of a GEAM metal sponge at $T/T_{ref} = 0.04$ ($N = 50000$, $n = 0.25$, $\rho_{des} = 1$, all in reduced units) obtained via MD simulation. Initial configuration is fcc lattice (not shown). Snapshots taken at $t/t_{ref} = 100$, 150, 250 and 500. Black surfaces are cross sections of the system with simulation cell.

In this section, a variation of the GEAM model potential serves to create metallic porous media (sponge): a controlled mismatch is introduced between overall number density n and desired (bulk) embedding density ρ_{des}. If $\rho_{des} > n$ for given particle

density n, after onset of the simulation run each atom tries to obtain the local embedding density – and local number density – equal to desired embedding density. The holes surrounded by metal are created. The surface tension in GEAM is very high compared with Lennard-Jones interaction potential, cf. Ref. [126]. As result sponge walls stay connected while material tries to reduce its surfaces. In this way a set of sponges with continuously decreasing surface, volume, and connectivity is created. The pore structure resembles that of the porous silica glass or the polymer membranes.

Snapshots of GEAM metal sponge at $t/t_{\mathrm{ref}} = 100, 150, 250, 500$ are shown in Fig. 6.6. In the starting configuration (not shown) atoms are placed at the ideal fcc lattice sites. The overall number density is $n = N/V = 0.25$ in reduced units and the desired (bulk) embedding density $\rho_{des} = 1.0$ of the GEAM metal. The temperature is fixed to $T = 0.04$. The generated configurations are stored for later use in the computation of diffusion properties of fluid confined in the pores. The rate of phase separation at onset of simulation is very high and decreases with the time, see Fig. 6.7. This should be explained by increasing of the size of the sponge walls, cf. Fig. 6.4 in previous section. In applications, foams are usually produced with $0.05 - 0.20$ porosity, defined as ratio between volume occupied by sponge walls and total volume occupied by the sponge. In GEAM metal porosity should converge to a ratio between global number density and desired embedding density $n/\rho_{des} = 0.25$. Also volume should converge to $V = nV_0$ and surface to $S = (4\pi)^{1/3}(3nV_0)^{2/3}$. In the current system, the porosity converges to $V/V_0 = 0.3$ after 1500 LJ time units. This is a finite size effect, due to the volume occupied by the particles at the surface of the wall. For the same reason the total volume and surface
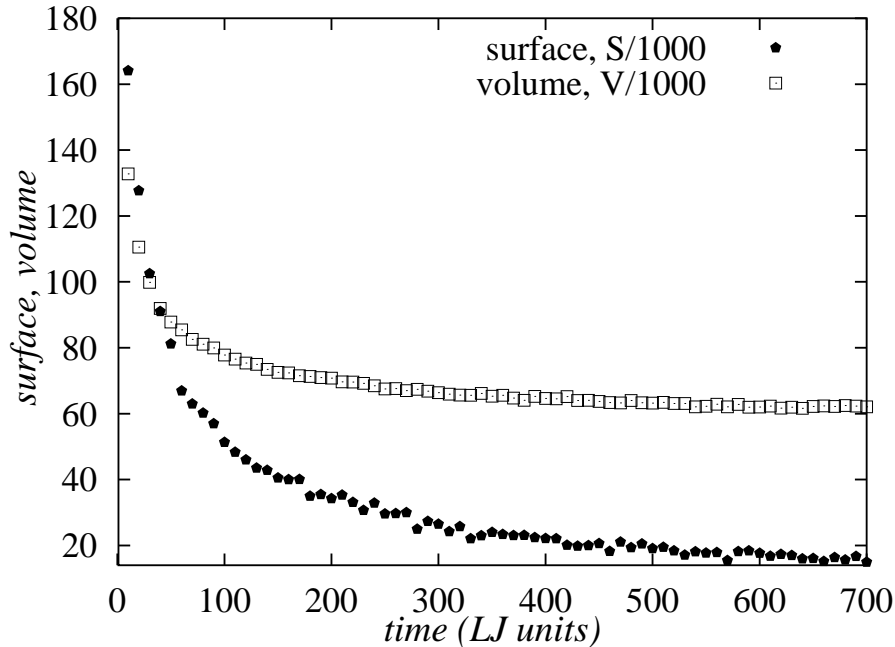

Figure 6.7: Evolution of volume and surface during equilibration of a GEAM metal sponge at $T/T_{ref} = 0.04$ obtained via MD simulation ($N = 50000$, $n = 0.25$, $\rho_{des} = 1$, all in reduced units). Initial configuration is fcc lattice (not shown). Volume and surface of the sponge are calculated via Monte Carlo integration.

converge to $V = 60000$ and $S = 10000$ in reduced units, respectively, cf. Fig. 6.7. The volume of the free space inside the pores is $V_{\text{pore}} = V_0 - V$. However a comparison with systems, which are smaller/larger by a factor $10 - 20$, confirms that the sponge structure is qualitatively independent of the system size above $N \sim 10000$ particles under the current conditions.

● gas particles   ◐ particles with fixed positions
○ sponge wall particles   inside of the sponge
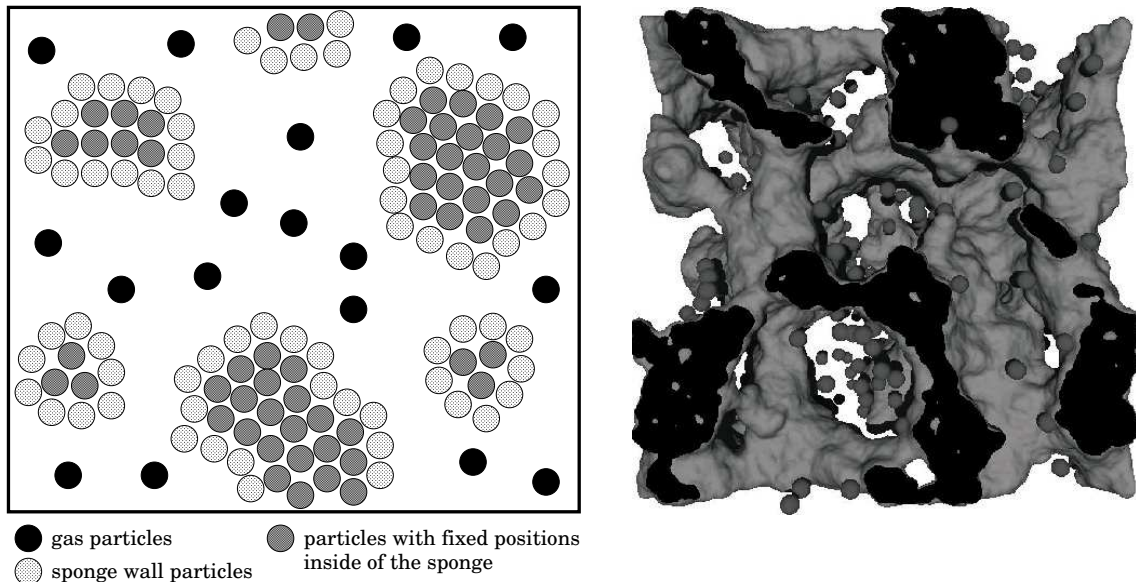
Figure 6.8: Schematic representation of model porous system (left). The thermostat acts only on wall particles (light gray), the gas particles (black) are thermostated indirectly through the walls. Snapshot of the system with $N = 400$ SHRAT particles at $t/t_{\text{ref}} = 900$ (right). The porosity of the sponge is $V/V_0 = 0.35$. Black surfaces are cross sections of the system with simulation cell.

6.2.1 Diffusion of short range attractive particles

The starting configuration is obtained by taking a snapshot of the GEAM sponge at $t/t_{\text{ref}} = 250$ during the relaxation, see Figs. 6.6 and 6.7. The pores of the sponge are then randomly filled with the particles interacting via SHRAT potential (Eq. (2.12). For the choice of parameters $(r_{\text{min}} = 2^{1/6}, r_{\text{cut}} = 1.6)$ made in this work, SHRAT potential resembles the Lennard-Jones (LJ) potential. The trajectories for the SHRAT gas particles and particles at the surfaces of the wall are calculated via molecular dynamics method described in Sec. 3. The positions of particles inside of the sponge are fixed to prevent a change of the topology of the porous media inside simulation box during the simulation. The temperature of the particles at the sponge surface is controlled by rescaling their velocities, see Sec. 3.3, and gas particles are thermostated indirectly through the collisions with the sponge wall particles. This is indicated schematically on the left side of Fig. 6.8 by the presence of a gas (black) particles within the pores. For potential modelling the interaction of gas particles with the pore wall is chosen as

a short range repulsive potential (SHREP):

$$\mathcal{U}_{\rm rep}(r) = \phi_0 r_0^{-4}(r_{\min} - r)^4 \tag{6.1}$$

for $r \le r_{\min}$, and $\mathcal{U}_{\rm rep}(r) = 0$ otherwise. A snapshot of this system is given in Fig. 6.8 (right).

In Fig. 6.9, molecular dynamics results are given at temperature $T/T_{ref} = 0.01$ for a dilute SHRAT gas with $N = 400, 4000$ particles. The system is relaxed for 2000 time units before the data are extracted. A typical way to characterize diffusive transport of a gas in porous media is through diffusion coefficient D. In a system consisting of a single type of particles, one also refers to a self diffusion coefficient. When particles move randomly, the self diffusion coefficient is defined through the mean square displacement using Einstein relation, $\langle \Delta r^2 \rangle = 6Dt$. According to Einstein relation, the increase of the mean square displacement with time has exponent equal unity at times larger then collision time. However, at low temperatures spontaneous condensation of SHRAT particles takes place, and clusters inside the pores are formed. This explains why the diffusion law becomes anomalous, i.e., $\langle \Delta r^2 \rangle \sim t^\alpha$ with exponent $\alpha = 0.93, 0.86$ smaller then unity for systems of $N = 400, 4000$ particles, respectively. In this case, the diffusion constant, $D \sim t^{\alpha-1}$, is time dependent in course of the pore condensation and decreases. The diffusion coefficient as function of time is influenced by the number density of SHRAT particles. At larger densities the clusters of SHRAT particles grow faster resulting in a smaller exponent α. As the number of atoms in cluster increases the exponent α is expected to converge to unity. The free diffusion regime, with exponent α equal unity, is associated with particles diffusing from the surface of the clusters. This crossover is not studied here due to the limited duration of the computer simulations.
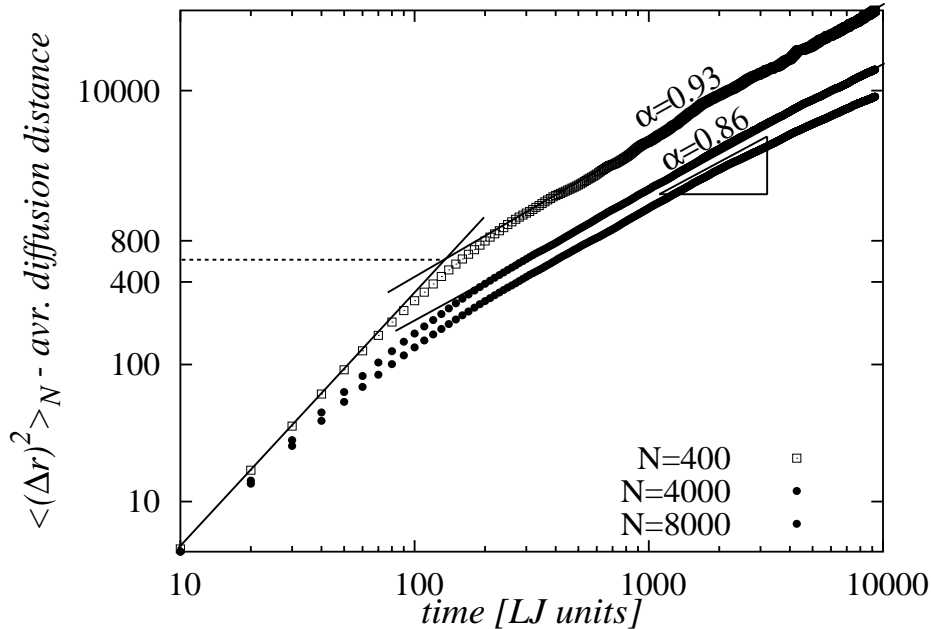
Figure 6.9: Mean square displacement (average diffusion distance) of SHRAT particle gas inside of the GEAM matrix as function of time at temperature $T/T_{ref} = 0.01$ for $N = 400, 4000$ SHRAT particles. All quantities are given in LJ units.
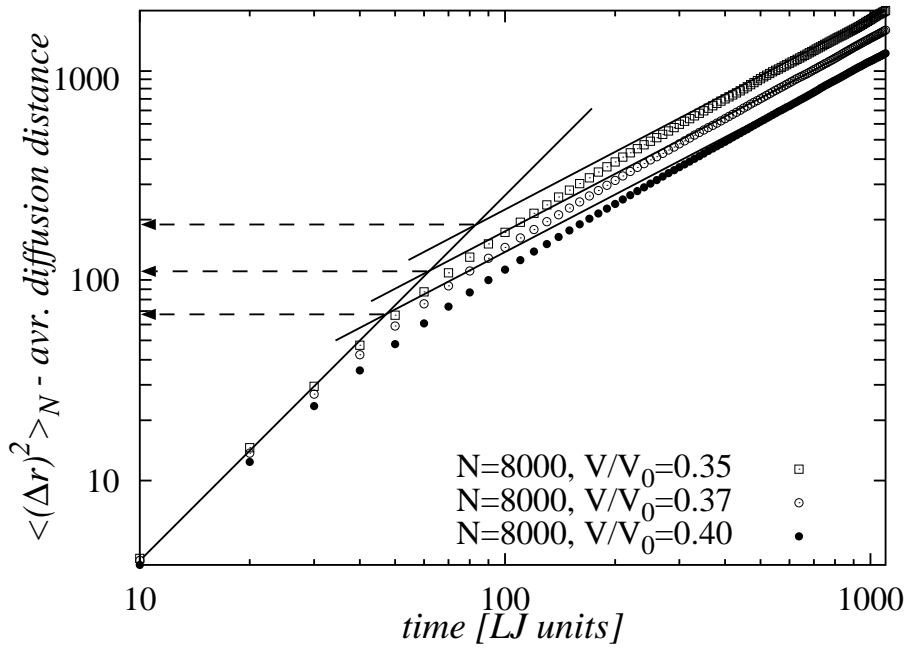
Figure 6.10: Effect of porosity on evolution of the mean square displacement with time of the SHREP gas inside of the GEAM matrix at temperature $T/T_{ref} = 0.015$ with $N = 8000$ SHREP particles. All quantities are given in reduced units. Starting configurations are created by taking snapshots of the GEAM sponge with porosity $V/V_0 = 0.4, 0.37, 0.35$ during relaxation and filling it randomly with SHREP particles.

6.2.2 Diffusion of short range repulsive particles

Using the same porous matrices like in the previous section diffusion of the particles interacting via the short range repulsive (SHREP) potential is studied. The evolution of mean square displacement with time is shown in Fig. 6.10. The system is relaxed typically for 1000 time units in system of $N = 8000$ particles before the data are extracted. In order to discuss the dependence of diffusion coefficient on the pore size and density, the dilute gas of hard spheres is introduced here as reference model. Two cases of this system are analyzed: (i) gas of hard spheres confined within porous media and (ii) unconfined gas of hard spheres. Generally, mean thermal velocity from Maxwell velocity distribution reads $\overline{v} = \sqrt{8k_BT/(m\pi)}$. The collision time or time of free flight is determined by mean free path l of particles between two collisions and mean thermal velocity, $t_{\rm coll} = l/\overline{v}$. The self diffusion coefficient is related to mean velocity and mean free path through $D = (1/3)\overline{v}l$, see Ref. [127].

In the case of an infinitely dilute gas of hard spheres confined within the porous media, the mean free path l equals the typical pore diameter $d_{\rm pore}$. Therefore the explicit form of the diffusion coefficient can be written as

$$D_{\rm pore} = \frac{1}{3}\sqrt{\frac{8k_BT}{m\pi}}d_{\rm pore}. \tag{6.2}$$

N	8000	8000	8000	800
V/V_0	0.4	0.37	0.35	0.35
t_{coll}	50	60	90	100
l	10	12	18	20
D_{pore}	0.63	0.76	1.1	1.3
D	0.21	0.28	0.33	0.75

Table 6.2: The values of porosity (V/V_0), collision time (t_{coll}), collision length (l), and diffusion coefficient (D) for four different systems calculated from MD simulation data using interpolation. The value D_{pore} is obtained under assumption that collision length l equals pore diameter d_{pore} in Eq. (6.2). The simulations are performed with $N_{GEAM} = 50000$ and $N_{SHREP} = 800, 8000$ particles at temperature $T/T_{ref} = 0.015$. All quantities are given in reduced units.

In Table 6.2 are listed the values of the porosity, collision time, mean free path and diffusion coefficient for four systems obtained by interpolation of the MD simulation data, see Fig. 6.10. The mean free path and collision time decrease fast with increasing porosity. The diffusion coefficient is calculated both from Einstein relation and previous considerations for dilute gas confined within the porous media. Already at small number densities of gas particles $n_{\text{SHREP}} = N_{\text{SHREP}}/V_{\text{pore}} = 0.006$, the diffusion coefficient (D) has half of the value calculated in dilute limit (D_{pore}). The reason might lie in the heterogenous structure of the porous media, yet the simulations presented here prove to
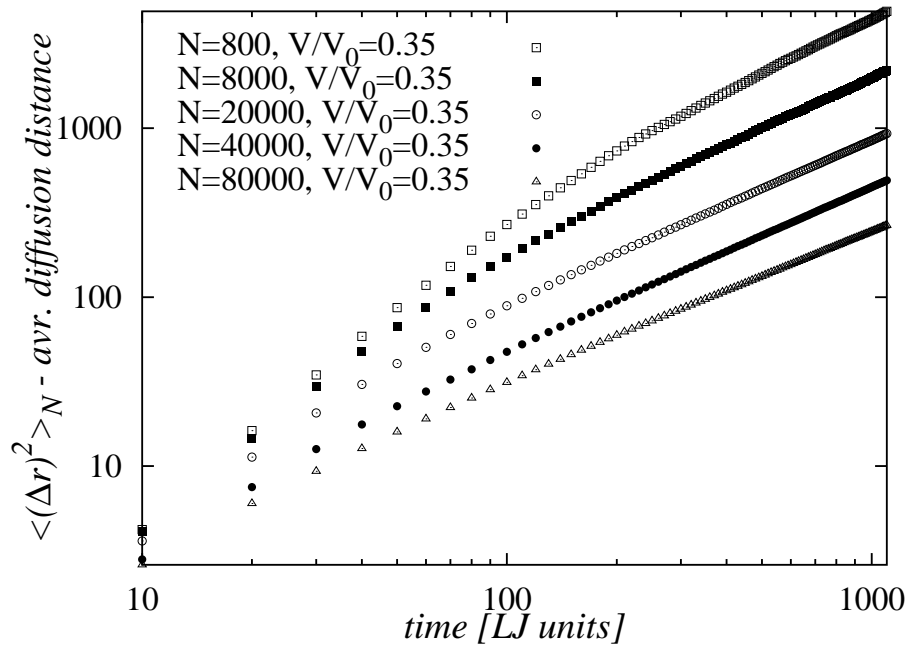
Figure 6.11: Mean square displacement of SHREP gas inside of the GEAM matrix at temperature $T/T_{ref} = 0.015$, for $N_{SHREP} = 800, \ldots, 80000$ SHREP particles. All quantities are given in reduced units. The structure GEAM metal sponge is fixed at $t/t_{ref} = 250$, $n/n_{ref} = 0.25$, $V/V_0 = 0.35$, and $N_{GEAM} = 50000$.

be unable to resolve this. With the increasing number of SHREP particles their collisions become more frequent, and collision time and mean free path become shorter. Also the transition from free flight into diffusion regime becomes smoother, see Fig. 6.11. The diffusion coefficient as function of the number of SHREP particles is given in Fig. 6.12.

In the following, the comparison with the case of the unconfined gas of hard spheres is made. The mean free path l between two collisions of gas particles can be written as $l = (\sqrt{2}n\sigma)^{-1}$ where n is the number density of gas particles. The effective cross section σ is given by $\sigma = \pi r_{\text{eff}}$ with the effective diameter determined by the distance where the repulsive energy of the potential in Eq. (6.1) equals temperature:

$$r_{\text{eff}} = r_{\min} + (r_0 \phi_0^{-1/4})(k_{\text{B}}T)^{1/4}. \tag{6.3}$$

In this way it is obtained

$$D_{\text{free}} = \frac{2}{3\pi^{3/2}} \frac{1}{n r_{\text{eff}}(T)^2} \sqrt{\frac{k_{\text{B}}T}{m}}, \tag{6.4}$$

for the diffusion coefficient of the dilute hard sphere gas. This approximation serves as a reference for the results shown in Fig. 6.12. Although the graph of the hard sphere gas globally has the similar shape it does not fit the simulation results under any condition, cf. Fig. 6.12. The value of the diffusion coefficient of the confined system is finite and always smaller then one of the bulk system.
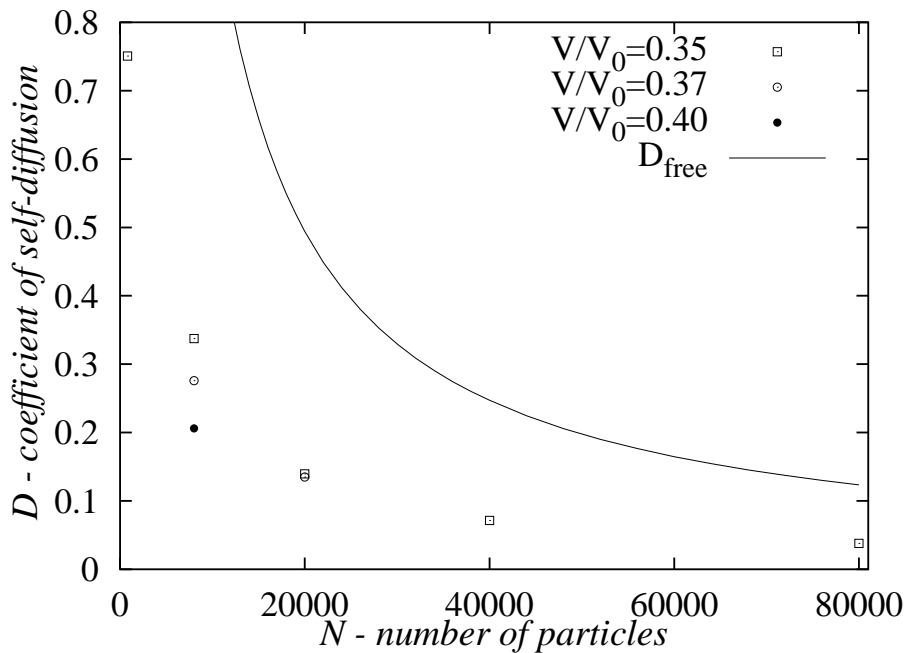
Figure 6.12: Self-diffusion coefficient of short range repulsive particles confined within porous media as function of number of particles. The structure GEAM metal sponge is fixed at $t/t_{ref} = 250$, $n/n_{ref} = 0.25$, $V/V_0 = 0.35$, and $N_{GEAM} = 50000$. The curve represents the expresion for diffusion coefficient of the unconfined dilute hard sphere gas, Eq. (6.4). All quantities are given in reduced units.

Chapter 7

Conclusions

The structural changes and flow properties in several equilibrium and nonequilibrium systems were investigated using a simple embedded atom model potential and molecular dynamics simulations. The focus of the work was on the interplay between intermediate structural changes, mechanical response of the system and material transfer at model metal interfaces under the steady shear flow. Some results were presented for drain in foam walls and transport of gases of short range attractive and repulsive particles through the model porous media.

The particulary simple low degree polynomial embedded atom model potential was introduced in Sec. 2.2, and expressions were derived for the pressure tensor and the elastic modulus tensor (Born-Green and fluctuation contributions). These expressions were applied to fcc, bcc crystal structures, and liquid metals. The general expressions given, however, also apply to other crystal structures such as simple cubic, hcp, or diamond cubic. The low degree polynomial format of the potential yields a simple dependency of the ground state constitutive properties (e.g. cohesive energy, heat of solution, and components of elastic modulus tensor) on model parameters. Thermo-mechanical properties of the model have been calculated using MD simulation. An expression for the "cold" isotropic pressure was adapted to fit the simulation results for a wide range of model parameters at different temperatures and densities. In addition, the bulk modulus has been determined from MD and compared to its counterpart calculated from an approximate expression for the pressure. The analytic formula for the isotropic pressure, Eq. (5.1), could be used as a closure relation (constitutive relation) in the mesoscale simulation techniques [40, 41, 42, 43] discussed in the Introduction. As demonstrated in Sec. 5.4, the isotropic pressure of the system is determined by the equilibrium pressure of the dominant structure when subjected to steady shear. This finding extends the application of the formula, Eq. (5.1), to other systems under steady shear deformation.

In the present work special attention is paid to the response of the system to an imposed shear deformation, switched on and proceeding with a constant shear rate. The studied system shows elastic behavior for the small deformations. Beyond a yield deformation, the system undergoes a transition to a regime of continuous plastic flow. The influence of the temperature on the values for the yield deformation and the relaxation behavior of the accumulated stress has been discussed. The generation of defects, and the local melting of the system after yield prevents stick-slip motion at low shear, as ob-

served earlier for the the pure SHRAT fluid, cf. Ref. [66]. Under steady shear flow solids are very much like structured liquids, however, an attempt to describe flow properties with the viscosity will lead to very high values of the viscosity coefficient. It is observed that shear stress decreases with increasing temperature. The relation between shear stress and temperature has been rarely studied so far, leading to a controversy if shear stress should rise or fall with temperature. The work done on the creep between railway wheels and rails, see Ref. [128], shows a decrease of the creep force with sliding velocity only under the assumption, that the friction coefficient (shear stress) decreases with temperature. A correlation between the resistance to shear and the material strength parameters such as the yield stress was usually assumed [2, 128]. The NEMD simulation results presented here show, that this correlation results from processes taking place on the nanometer scale: the local structure becomes less pronounced with the increase of the temperature and puts less resistance to the shear. The NEMD simulations also show that normal pressure differences vanish within precision of data presented in this work.

Information about the local structure, on the level of an atom and its first neighbors, in systems subjected to shear is obtained via a common neighbors analysis based on planar graphs in Chapter 4. The method resolves the fcc, bcc, hcp and amorphus icosahedral structure. In the steady state particles form 2D layers and the shear direction is parallel to the direction to the first neighbor in these layers. All three crystal structures are observed in the steady state, an icosahedral structure is only observed in an intermediate regime at higher shear rate $\dot{\gamma} = 0.01$. The influence of shear generated defects on the local structure after the onset of shear and in the steady state is discussed. Furthermore, the common neighbor analysis is used here to calculate a nonequilibrium phase diagram, valid for low shear rates. At high temperatures the bcc structure is observed at densities, whereas the fcc structure dominates at lower temperatures. The calculations of the free energy along a Bain transformation path gave an insight into the thermodynamics of the system and led to an interpretation of a nonequilibrium phase diagram. The transition of fcc structure into bcc structure upon the increase of temperature is found to be the result of different vibrational entropies of the two structures. This transformation could take place due to the combined effect of the pressure and temperature in the rail tracks leading to hardening of the material after the rapid cooling.

A rather complex behavior is seen even in the steady shear regime at small time scales. The shear deformation involves motion of these planes. In the steady state regime, defects are created when atoms move oblique to the shear direction to reach some close-by energetically preferred states. These defects potentially block the shear flow and lead to shear banding. While the total amount of crystallinity during the simulation is fairly constant (quantified via common neighbor analysis), the fcc structure partially transforms, as long as defects blocking the flow are present, into the bcc structure. During these processes, transient, grained microstructures are created. Related to the grain formation is the mixing of the material through rotation of the grains before the system re-enters a dynamically equilibrated (stationary) state. The structural information also helps to interpret the observed changes of the pressure tensor. It could be shown, that the isotropic pressure is mainly determined by the (instantaneously)

dominating crystal structure. Normal pressure differences are close to zero during most simulation runs. Nonvanishing normal pressure differences occur if defects (blocking the flow) are created which the system cannot accommodate. The shear stress is found to depend on the modes of collective motion of atoms stacked into hexagonal planes. The NEMD results for shear stress and normal pressure differences were compared with analytic calculations for collectively moving atoms. In situations, where defects are blocking the flow, except within a narrow slit, stick-slip motion under very high effective shear rates is observed. The stick-slip motion observed in this work is relevant at the 'nanoscale'. On the level of several asperities, during a dry solid friction process, stick-slip might become coarse-grained and smooth, or trigger stick-slip on larger scales. Conclusions about these mechanisms are obviously out of reach for the present simulations. However, stick-slip on the nanoscale is accessible when sliding a blunt tip over a substrate. In this application shear deformation is confined within several layers around the interface.

The generic embedded atom model has been further extended to study interfaces between different metals with similar lattice constants. The the dependence of the heat of solution and the local density for a single substitutional impurity on model parameters is illustrated. The mechanism of mixing (or mechanical alloying) are similar for all three versions of interface: homogeneous, with additional embedding interaction and with different shear moduli. Unexpected at first glance, the additional embedding interaction leads to a pronounced increase in the local density. For the same system, penetration of inclusions through the interface and subsequent mechanical alloying has been observed and discussed. Further, gradual alloying at the interface has been traced back to the mismatch (final angle) between the interfacial plane and shear direction. In this early stage of mechanical alloying, an influence of the additional embedding interaction on the shear stress is not detected. The area where two materials are mixed occupies only a small portion of the total volume and thus only slightly influences the pressure tensor components. The low degree polynomial format of GEAM comes together with a simple relationship between the strength of the two body interaction and the shear moduli in the limit of low temperatures, which determine the resistance of the system to the shear deformation. A dependence between ratios of shear moduli, shear stresses and effective shear rates in two materials is found, while the values for moduli, shear stress and shear rates of the pure materials seem to be (at least in this study) uncorrelated. The explanation should be that modes of collective motion of hexagonal layers are coupled across the material interface.

Interfaces between metals with different lattice constants where potential incommensurabilities increase the number of dislocation types remain to be studied.

The features observed in this work should be generic to high-speed friction at the metal-metal interface. Except for very finely polished surfaces, mesoscale inhomogeneities and inclusions at mesoscale are known to play an important role. In this work, the plastic yield and friction stress have been analyzed within asperities on the nanometer-scale. Local densities, temperatures, and shear rates inside the asperity are input parameters for the NEMD simulations. The friction process itself is seen as a combined effect of processes on a micro-scale (size of asperities) and a nano-scale. The

meso-scale methods [40, 41, 42, 43] are expected to overcome the gap between the micrometer scale and the nanometer scale. These methods need a phenomenological model that describes the behavior of the pressure tensor components under deformation. The results presented in this work may serve as motivation for new models that incorporate structural changes and their effect on the pressure tensor in a metal subject to shear deformation and flow.

Last but not least, the embedded atom method was adapted to study porous metallic structures. The evolution of the structure during the rupture of the metallic foam wall was studied in detail. The influence of cohesive and surface energies and additional particles was analyzed. It was found, that an increase of the energy per particle in the whole system accelerates the rupture of the wall, whereas the additional particles bound surrounding metal particles, creating a network and slowing drainage. This results in a slowing of the rupture. The performed simulations were at nanoscale, still the simulation results showed a number of experimentally observed phenomena. Under the appropriate choice of simulation parameters (controlled mismatch between desired embedding density and number density), the model yields porous structures that resemble porous glasses or the porous membranes. The pores were filled with the gases of short range attractive (SHRAT) and repulsive particles (SHREP). Spontaneous condensation of SHRAT particles is observed. Two hard sphere systems were used as reference system in order to discuss the influence of porosity and pore topology on diffusion of SHREP particles. Much of the earlier work on the simulation of fluids in the pores employed slit or cylindrical pore models and solid surface was treated either as smooth, structureless or idealized structured wall [129, 130, 131]. Yet, in addition to the pore shape and size, there are other factors which influence transport of fluid through the porous media, such as macroscopic structure and topology of the pore space. There is still no agreement which geometrical measures are needed to completely characterize the transport through the porous media. One of the structural measures of choice may be the average mean curvature and connectivity obtained via Minkowski functionals [125]. The present work, should serve as a starting point for further investigations of transport in EAM porous media.

Appendix A

Common neighbor analysis code

PROGRAM SUMMARY

Title of program: RLSCODE

Catalogue number: ADPZ

Program obtainable from: CPC Program Library, Queen's University of Belfast, N. Ireland

URL: http://cpc.cs.qub.ac.uk/summaries/ADPZ

Licensing provisions: Persons requesting the program must sign the standard CPC-non-profit use license (see license agreement printed in every issue)

Computer for which the program is designed and others on which it has been tested: Alpha-Workstation, Silicon Graphics, Sun, Linux-PC, Windows-PC, MacIntosh

Operating systems or monitors under which the program has been tested: DEC-Unix, Irix, Solaris, Linux, Windows 98

Program language used: Fortran, Mathematica$^{\text{TM}}$

Memory required to execute with typical data: 10 MBytes

Restrictions on the complexity of the problem
The machine must provide the necessary main memory which increases roughly linearly with the number of particles.

No. of lines in distributed program: 2224
Number of lines in distributed program and number of fields in distributed test data is summarized in Table A.1.

Typical running time
A typical running time is less then 20 seconds for 10000 particles on a 600 MHz Pentium processor.

Keywords: Structure recognition, algorithm, configuration analysis, metal

code file name	lines	content
structure.f	356	main program
inc.order	2224	contains all subroutines

configuration file name	particles #	content
fcckembed.temp=0.00500..0.06440	10976	configurations, melting of fcc
bcckembed.temp=0.00500..0.06440	11664	configurations, melting of bcc
output.shearT=0.008	17576	system under shear flow

Table A.1: Summary of source files of the RLSCODE package.

Nature of physical problem
The nature of the problem is to provide a quantitative measure for the local order in non-ideal crystalline configurations. This measure will be necessarily heuristic in nature and not unique. Configurations are specified by collection of particle position in 3D. The program should return the type of local structure (face centered cubic etc.) for each atom of the system.

Method of solution
The method is based on a suitable definition for "neighboring atoms". The corresponding neighbor list, together with information about correlations between neighbors, is used to uniquely recognize a number of representative crystal structures. The criteria for the recognition of different crystal structures is formulated using graphs.

The Program
The code RLSCODE makes use of the standard Voronoi construction [87] to determine relevant neighbors. The minimum image convention and a cutoff, the distance beyond which atoms are assumed not to be neighbors are used. These measures can cause unreliable results for small and/or random systems, if the cutoff is chosen without care. To avoid that atoms from second coordination shell of fcc and hcp structures enter analysis, and to ensure that atoms from the (overlapping) first and second coordination shells of bcc structures enter, a preselection is made by taking cutoff radius to be minimum of the global pair correlation function between the shell containing "relevant neighbors" and the subsequent one. The first step of the analysis is therefore to extract the pair correlation function, the position of its first maximum, as well as the first relevant minimum, (procedure CUTOFFRAD, TableA.2), and to extract from the list of potential neighbors a set of relevant neighbors by the Voronoi analysis (NEIGHBLST, Table A.2). Subroutine NEIGHBLST represents the standard Voronoi analysis. This routine takes in a configuration in a cuboid with periodic boundary conditions and for each atom obtains the information about relevant neighbors. Using cutoff radius subroutine NEIGHBLST eliminates atoms which are neighbors only in one point of space (relevant for perfect lattices). For bcc lattice the subroutine returns 6 closest atoms more than it would be expected from coordination number. The information about relevant neighbors is stored in NABLST - a two dimensional matrix containing the list of indices of relevant neighbors and an array NNAB which contains the number of relevant neighbors for each atom.

name of subroutine	arguments	action, output
ORDER_START	—	opens *BCC.DM*, *FCC.DM*, *HEX.DM*, *ALL.DM* and *CRS.nb* files
ORDER_STOP	—	closing the **.DM* and *CRS.nb* files.
CUTOFFRAD	N,MX,MY,MZ,X,CL	Function determines r_{cut} (RCUT)
NEIGHBLST	N,RCUT,MX,MY,MZ,X,CL, NNAB,NABLST	Voronoi analysis, which creates neighbor list. Output is stored in NNAB,NABLST variables.
STRUCTLST	N,NABLST,NNAB, CELLTYPE	Structures analysis. CELLTYPE is output.
STRUCTOUT	RTIME,N,X,CL,CELLTYPE NNAB,NABLST,PL	Amounts of different structures and profile are sent on standard output. (axis: PL$\in \{1:x, 2:y, 3:z\}$)
DIRECTOUT	RTIME,N,X,CL,CELLTYPE NNAB,NABLST,NM	calculates angular distributions of neighbors and stores it to **.DM*.
CRSSCTOUT	RTIME,N,X,CL,CELLTYPE, NNAB,NABLST,RSTART, REND,PL	makes cross section of the system and stores it to *CRS.nb*.
PRESSURE	N,MX,MY,MZ,X,CL	Function calculates potential part of pressure.

Table A.2: Table of the main RLSCODE subroutines, their variables and actions. Few more subroutines existing in code are used internally and are not included here.

parameter	type	limitations	meaning
——————— input parameters ———————			
N	integer	memory	total number of particles
X(#1,#2)	float	memory	coordinates #2=(1:x,2:y,3:z)
			for particle number #1=1,..,N
CL(1-3)	float	> 0	cell dimensions (reduced units)
PL	integer	$\in \{1, 2, 3\}$	axis normal to cross section
			and axis of profile (1:x,2:y,3:z)
NM	logical	.true./.false.	.true. if neighbor angular
			distribution is to be normalized
RSTART	float	$|..| < \mathsf{CL(PL)}/2$	start of cross section interval
REND	float	$|..| < \mathsf{CL(PL)}/2$	end of cross section interval
RTIME	float	no	time parameter for animated output
——————— output variables ———————			
RCUT	float	> 0	cut-off distance r_{cut}
MX,MY,MZ	float	> 3,	number of cells in x, y, z-direction,
		$< \mathsf{CL/RCUT}$	implemented value: $\mathsf{CL/RCUT}/2$
NNAB(#1)	integer	memory	number of neighbors for particle #1
NABLST(#1,#2) ..	integer	memory	particle number of #2'th neighbor
			of particle number #1
CELLTYPE(#1,#2)	logical	.true./.false.	.true. if particle #2 has lattice type
			#1$\in \{$fcc(1),hcp(2),bcc(3),ico(4)$\}$

Table A.3: Summary of input and output variables used by subroutines.

The subroutine STRUCTLST performs the analysis of neighbor displacements and returns a matrix with $4\,N$ elements: CELLTYPE. The information about structure that surrounds each of the atoms is stored in a four dimensional field of logical type. The field value is "true" for an atom if it is found to belong to one of the following structures 1:fcc, 2:hcp, 3:bcc and 4:ico. For any atom only one of these field values can carry the "true" bit. If an atom belongs to none of the four structures all fields are "false".

The information obtained by subroutines NEIGHBLST and STRUCTLST are treated and visualized by subroutines STRUCTOUT, DIRECTOUT and CRSSCTOUT. The relative amount of space occupied by fcc, hex, and bcc structure, as well as their combined amount and profiles are calculated by subroutine STRUCTOUT. Output of the latter procedure is directed to standard display. The subroutine DIRECTOUT calculates angular distribution functions of the relevant neighbors for the whole system and each of the crystal structures separately. The output is saved to four files ALL.DM, FCC.DM, HEX.DM, BCC.DM respectively for all atoms and atoms only surrounded with fcc, bcc and hcp structure. Cross sections of the system in three orthogonal planes are visualized with the subroutine CRSSCTOUT. The output is stored in CRS.nb file. The output of the subroutines DIRECTOUT and CRSSCTOUT is in Mathematica$^{\mathrm{TM}}$ format, see Table A.4.

Subroutines are summarized in Table A.2 and their parameters are collected in Table A.3. The input data needed to evaluate the local structure consists of coordinates

file name		content	call
ALL.DM		neighbors of all atoms	ALLN[⟨time parameter value⟩]
FCC.DM		neighbors of fcc atoms	FCCN[⟨time parameter value⟩]
HEX.DM	in Mathematica™ format	neighbors of hcp atoms	HEXN[⟨time parameter value⟩]
BCC.DM		neighbors of bcc atoms	BCCN[⟨time parameter value⟩]
CRS.nb		cross sections	CRSxxx[⟨time parameter value⟩, ⟨plane⟩] where xxx ∈ {FCC,BCC,HEX,ICO,NON}

Table A.4: Summary of files being produced by RLSCODE run. Subroutine CREATE-OUT creates angular distributions of directions to closest neighbors and stores them to files *ALL.DM*, *FCC.DM*, *HEX.DM*, and *BCC.DM*. File *CRS.nb* is created by procedure CRSSCTOUT. Indices are the time parameter, also used for creating animations, and the plane of the cross section (1:x, 2:y, and 3:z). The last column lists the appropriate Mathematica™ calls.

of particles, dimensions of simulation box and a free (time) parameter potentially used for animations, cf. Table A.3.

The output of the subroutine STRUCTLST looks like:

```
...
  AVERAGE COORDINATION NUMBER =   12.45756
NUMBER OF ATOMS WITH    8 NEIGHBOURS     1
NUMBER OF ATOMS WITH    9 NEIGHBOURS     8
NUMBER OF ATOMS WITH   10 NEIGHBOURS    85
NUMBER OF ATOMS WITH   11 NEIGHBOURS   852
NUMBER OF ATOMS WITH   12 NEIGHBOURS  9448
NUMBER OF ATOMS WITH   13 NEIGHBOURS  5274
NUMBER OF ATOMS WITH   14 NEIGHBOURS  1906
NUMBER OF ATOMS WITH   15 NEIGHBOURS     2
NUMBER OF ATOMS WITH   16 NEIGHBOURS     0
NUMBER OF ATOMS WITH   17 NEIGHBOURS     0
2-axis disc. DENS HEX  DENS FCC  DENS BCC   DENS ICO  DENS 1CRY DENS
2CRY  [tLJ=2000.00]
   0.12431   0.54645   0.53005   0.31694   0.00000   0.95082   0.77596
   0.37294   0.33526   0.54335   0.36416   0.00000   0.90173   0.63584
   0.62157   0.35111   0.46222   0.35111   0.00000   0.89778   0.59556
   0.87020   0.58015   0.55725   0.06870   0.00000   0.87786   0.83969
   ...
  19.76601   0.30000   0.50455   0.30909   0.00000   0.86364   0.63636
  20.01464   0.14365   0.45304   0.50276   0.00000   0.93370   0.50276
  20.26327   0.28889   0.47222   0.52778   0.00000   0.91111   0.51111
  20.51190   0.45578   0.50000   0.27551   0.00000   0.88435   0.69048
show data about crystal structure...
        FCCnum    =    2000.0000000000                2998
        FCCvol    =    2000.0000000000        0.5454597473
        HEXnum    =    2000.0000000000                2695
        HEXvol    =    2000.0000000000        0.5134842992
        BCCnum    =    2000.0000000000                 923
        BCCvol    =    2000.0000000000        0.1954938620
        ICOnum    =    2000.0000000000                   0
        ICOvol    =    2000.0000000000        0.0000000000
        crystal   =    2000.0000000000        0.8933204412
```

error message	stop	subroutine	meaning/usual reason
change N	yes	main prog.	the number of particles is different from expected
increase MX,MY,MZ or MAXB	yes	CUTOFFRAD	the number of cells, system is
	yes	NEIGHBLST	divided in, is too small
decrease MX,MY,MZ	yes	CUTOFFRAD	the number of cells, system is divided in, is too large
INCREASE IMPROFILE	yes	STRUCTOUT	profile resolution too small

warning message	stop	subroutine	meaning/usual reason
LESS THAN 4 POINTS GIVEN TO WORK	no	NEIGHBLST	free volume, missing atom
TOO MANY VERTICES	no	WORK	free volume, missing atom
LESS THAN 4 VERTICES FOUND IN WORK	no	WORK	free volume, missing atom
NONINTEGER NUMBER OF EDGES	no	WORK	free volume, missing atom
**** EULER ERROR: DEGENERACY ? ****	no	WORK	free volume, missing atom

Table A.5: Summary of error and warning messages and possible causes.

Bibliography

[1] B. N. J. Persson, *Sliding Friction*, 2nd ed. (Springer, Berlin, 2002).

[2] F. P. Bowden and D. Tabor, *The friction and lubrication of solids*, 2nd Ed. (Clarendon Press, Oxford, 1954).

[3] B. N. J. Persson, J. Chem. Phys. **115**, 3840 (2001); B. N. J. Persson, F. Bucher, and B. Chiaia, Phys. Rev. B **65**, 184106 (2002).

[4] V. D. Scott and T. Wilman, Proc. R. Soc. **247**, 353 (1958).

[5] Z. N. Farhat, Wear **250**, 401 (2001).

[6] J. P. Hirth and D. A. Rigney, in *Dislocations in Solids*, edited by F. R. Nabarro (North-Holland, Amsterdam, 1983), Vol. 6, p. 10.

[7] D. R. Wheeler and D. H. Buckley, Wear **33**, 65 (1975).

[8] J.-P. Poirier, *Creep of Crystals* (Cambridge University Press, Cambridge, 1985)

[9] B. L. Holian, A. F. Voter, N. J. Wagner, R. J. Ravelo, S. P. Chen, W. G. Hoover, C. G. Hoover, J. E. Hammerberg, and T. D. Dontje, Phys. Rev. A **43**, 2655 (1991).

[10] K. Kadau, T. C. Germann, P. S. Lomdahl, and B. L. Holian, Science **296**, 1681 (2002).

[11] D. Kuhlmann-Wilsdorf, Wear **200**, 8 (1996).

[12] N. S. Liou, M. Okada, M. A. Irfan, and V. Prakash, Opt. Laser. Eng. **40**, 393 (2003).

[13] W. R. Patterson and I. G. Greenfield, Acta Metall. **19**, 123 (1971).

[14] W. Loose and S. Hess, Rheol. Acta **28**, 91 (1989).

[15] B. J. Ackerson, J. B. Hayter, N. A. Clark, and L. Cotter, J. Chem. Phys. **84**, 2344 (1986); B. J. Ackerson and P. N. Pusey, Phys. Rev. Lett. **61**, 1033 (1988); B. J. Ackerson, J. Rheol. **34**, 553 (1990).

[16] M. J. Stevens, M. O. Robbins, and J. F. Belak, Phys. Rev. Lett. **66**, 3004 (1991); M. J. Stevens and M. O. Robbins, Phys. Rev. E **48**, 3778 (1993).

[17] P. J. Craievich, M. Weinert, J. M. Sanchez, and R. E Watson, Phys. Rev. Lett. **72**, 3076 (1994).

[18] A. Chang, C. Colinet, M. Hillert, Z. Moser, J. M. Sanchez, N. Saunders, R. E Watson, and A. Kussmaul, Calphad:Comput. Coupling Phase Diagrams Thermochem. **19**, 481 (1995).

[19] P. J. Craievich, J. M. Sanchez, R. E Watson, and M. Weinert, Phys. Rev. B **55**, 787 (1997).

[20] U. Pinsook, Phys. Rev. B **66**, 024109 (2002).

[21] J. R. Morris and K. M. Ho, Phys. Rev. Lett. **74**, 940 (1995).

[22] K. Kadau, *Atomistic study of structural phase transitions in bulk, nano-particles, and thin films*, (Ph.D. thesis, Duisburg, Germany, 2001).

[23] C. M. Mate, in *Handbook of Micro/Nano Tribology*, edited by B. Bhushan, (CRC Press, Boca Raton, 1995) p. 167.

[24] *Nanoscience: Friction and Rheology on the Nanometer Scale*, edited by E. Meyer, T. Gyalog, R. M. Overney, and K. Fransfeld, (World Scientific, Singapore, 1998).

[25] M. R. Sørensen, K. W. Jacobsen, and P. Stoltze, Phys. Rev. B **53**, 2101 (1996).

[26] O. M. Braun and M. Peyrard, Phys. Rev. E **63**, 046110 (2001).

[27] M. H. Müser and M. O. Robbins, Phys. Rev. B **61**, 2335 (2000); M. H. Müser, L. Wenning, and M. O. Robbins, Phys. Rev. Lett. **86**, 1295 (2001).

[28] E. D. Smith, M. O. Robbins, and M. Cieplak, Phys. Rev. B **54**, 8252 (1996).

[29] B. N. J. Persson, Phys. Rev. B **48**, 18140 (1993).

[30] A. Buldum and S. Ciraci, Phys. Rev. B **55**, 12892 (1997).

[31] A. Buldum and S. Ciraci, Phys. Rev. B **60**, 1982 (1999).

[32] J.E. Hammerberg, B.L. Holian, J. Roder, A.R. Bishop, and S.J. Zhou, Physica D **123**, 330 (1998).

[33] H. V. Swygenhoven, P. M. Derlet, and A. G. Frøseth, Nature Mater. **3**, 399 (2004).

[34] E. B. Tadmor and S. Hai, J. Mech. Phys. Solids **51**, 765 (2003).

[35] H. V. Swygenhoven and P. M. Derlet, Phys. Rev. B **64**, 224105 (2001).

[36] M. R. Schiøtz, T. Vegge, F. D. Di Tolla, and K. W. Jacobsen, Phys. Rev. B **60**, 11971 (1999).

[37] A. Böhmer and T. Klimpel, Wear **253**, 150 (2002).

[38] F. Bucher, K. Knothe, and A. Theiler, Wear **253**, 204 (2002).

[39] M. Ertz and K. Knothe, Wear **253**, 498 (2002).

[40] J. J. Monaghan, Annu. Rev. Astron. Astrophy. **30**, 543 (1992).

[41] L. D. Libersky, A. G. Petschek, T. C. Carney, J. R. Hipp and F. A. Allahdadi, J. Comput. Phys. **109**, 67 (1993).

[42] M. Ellero, S. Hess, and M. Kröger, J. Non-Newtonian Fluid Mech. **105**, 35 (2002).

[43] B. I. M. ten Bosch, J. Non-Newtonian Fluid Mech. **83**, 231 (1999).

[44] J. Wood, in *Proc. Fraunhofer USA Symposium on Metal Foams, Stanton, USA*, edited by J. Banhart and H. Eifert, (MIT Press-Verlag, Bremen, 1998).

[45] P. Åsholt, in *Proc. Metfoam'99, Bremen, Germany*, edited by J. Banhart, M. F. Ashby, and N. A. Fleck, (MIT Press-Verlag, Bremen, 1998).

[46] T. Miyoshi, in *Proc. Metfoam'99, Bremen, Germany*, edited by J. Banhart, M. F. Ashby, and N. A. Fleck, (MIT Press-Verlag, Bremen, 1998).

[47] F. Baumgärtner, I. Duarte, and J. Banhart, Adv. Eng. Mater. **2**, 168 (2000).

[48] I. Duarte and J. Banhart, Acta Mater. **48**, 2349 (2000).

[49] J. Banhart and J. Baummeister, J. Mater. Sci. **33**, 1431 (1998).

[50] J. Banhart, Prog. Mat. Sci **46**, 559 (2001).

[51] Th. Wübben, H. Stanzik, J. Banhart, and S. Odenbach, J. Phys.:Condens. Matter **15**, 427 (2003).

[52] C. Körner, M. Thies, and R. Singer, Adv. Eng. Mater. **4**, 765 (2002).

[53] C. Manwart, U. Aaltosalmi, A. Koponen, R. Hilfer, and J. Timonen, Phys. Rev. E **66**, 016702 (2002).

[54] R. Helmig, *Multipase flow and Transport Processes in the Subsurfaces*, (Springer, Berlin, 1997).

[55] P. R. King, S. V. Buldyrev, N. V. Dokholyan, S. Havlin, Y. Lee, G. Paul, H. E. Stanley, Physica A **274**, 60 (1999).

[56] K. Mecke and D. Stoyan, *Statistical Physics and Spatial Physics*, (Springer, Berlin, 2000).

[57] S. G. J. M. Kluijtmans, E. H. A. de Hoog, and A. P. Philipse, J. Chem. Phys. **108**, 7469 (1998).

[58] M. A. Knackstedt, B. W. Ninham, and M. Monduzzi, Phys. Rev. Lett. **75**, 653 (1995).

[59] M. S. Daw and M. I. Baskes, Phys. Rev. Lett. **50**, 1285 (1983); Phys. Rev. B **29**, 6443 (1984).

[60] R. A.Johnson, Phys. Rev. B **37**, 3924 (1988); R. A. Johnson, Phys. Rev. B **37**, 6121 (1988); R. A. Johnson, Phys. Rev. B **39**, 12554 (1989).

[61] F. J. Cherne, M. I. Baskes, and P. A. Deymier, Phys. Rev. B **65**, 024209 (2001).

[62] S. Hess, M. Kröger, and W. G. Hoover, Physica A **239**, 449 (1997).

[63] M. Born, J. Chem. Phys. **7**, 591 (1939); Proc. Cambridge Philos. Soc. **36**, 160 (1940); H. S. Green, *The Molecular Theory of Fluids* (North-Holland, Amsterdam, 1952); M. S. Green, J. Chem. Phys. **22**, 398 (1954).

[64] L. A. Shuvalov, A. A. Urusovskaya, I. S. Zheludev, A. V. Zalessky, S. A. Semiletov, B. N. Grechushnikov, I. G. Chistyakov, and S. A. Pikin, *Modern Crystallography IV* (Springer, Heidelberg, 1998), pp. 51-85.

[65] R. A. Johnson in *Many-Atom Interactions in Solids*, Springer Proceedings in Physics Vol. 48 (Springer, Berlin 1990), pp. 85-102.

[66] S. Hess and M. Kröger, Phys. Rev. E **64**, 011201 (2001).

[67] W. G. Hoover and S. Hess, Physica A **267**, 98 (1999).

[68] M. Kröger and S. Hess, Z. Angew. Math. Mech. **90**, Suppl. 1, 48 (2000).

[69] Y. R. Wang and D. B. Boercker, J. Appl. Phys. **78**, 122 (1995).

[70] M. S. Daw, Phys. Rev. B **39**, 7441 (1989).

[71] K. Fuchs, Proc. R. Soc. London, Ser. A **153**, 622 (1936).

[72] *American Institute of Physics Handbook*, edited by D.E. Gray, 3rd ed. (McGraw-Hill, New York, 1972).

[73] C. Zener, Phys. Rev. **71**, 846 (1947).

[74] C. Kittel, *Introduction to Solid State Physics*, 2nd Ed. (John Wiley&Sons, New York, 1976).

[75] W. G. Burgers, Physica **1**, 561 (1935).

[76] R. W. Wentzcovitch and H. Krakauer, Phys. Rev. B **42**, 4563 (1990).

[77] J. A. Zimmerman, H. J. Gao, and F. F. Abraham, Modell. Simul. Mat. Sci. Eng. **8**, 103 (2000).

[78] N. Bernstein and E. B. Tadmor, Phys. Rev. B **69**, 094116 (2004).

[79] K. Carling, G. Wahnström, T. R. Mattsson, A. E. Mattsson, N. Sandberg, and G. Grimvall, Phys. Rev. Lett. **85**, 3862 (2000).

[80] T. R. Mattsson and A. E. Mattsson, Phys. Rev. B **66**, 214110 (2002).

[81] J. Wang, S. Yip, S. R. Phillpot, and D. Wolf, Phys. Rev. Lett. **71**, 4182 (1993).

[82] R. Hultgren, P. D. Desai, D. T. Hawkins, M. Gleiser, and K. K. Kelley, *Values of the Thermodynamic Properties of Binary Alloys* (American Society for Metals, Metals Park, OH, 1973).

[83] S. Hess and W. Loose, Physica A **162**, 138 (1989).

[84] W. G. Hoover, Annu. Rev. Phys. Chem. **34**, 103 (2983); D. J. Evans and G. P. Morriss, Comput. Phys. Rep. **1**, 287 (1984); D. J. Evans and W. G. Hoover, Annu. Rev. Fluid. Mech. **18**, 243 (1986).

[85] D. J. Evans and G. P. Morriss, *Statistical Mechanics of Non-equilibrium Liquids* (Academic Press, London, 1990).

[86] W. G. Hoover, Physica A **194**, 450 (1993).

[87] M. P. Allen and D. J. Tildesley, *Computer Simulation of Liquids* (Clarendon, Oxford, 1987).

[88] L. Verlet, Phys.Rev. **159**, 98 (1967); L. Verlet, Phys.Rev. **165**, 201 (1967).

[89] A. W. Lees and S. F. Edwards, J. Phys. Chem. **5**, 1921 (1972).

[90] S. Nose, Prog. Theo. Phys. Supp. **103**, 1 (1991)

[91] D. J. Evans, and G. P. Morriss, Phys. Lett. **98A**, 433 (1983).

[92] L. V. Woodcock, Chem. Phys. Lett. **10**, 257 (1971).

[93] H. C. Andersen, as comment in H. C. Andersen et. al., Rapport d'activite scientifique du CECAM (Université Paris Sud, 1984).

[94] D. J. Evans, and G. P. Morriss, Phys. Rev. Lett. **56**, 2172 (1986).

[95] D. J. Evans, and G. P. Morriss, Phys. Rev. A **30**, 1528 (1984).

[96] W. Loose and S. Hess, in *Microscopic Simulations of Complex Flows*, edited by M. Mareschal, (Plenum Press, New York, 1990).

[97] M. F. Horstemeyer, M. I. Baskes, and S. J. Plimpton, Acta Mater. **49**, 4363 (2001).

[98] J. F. Archard, Wear **2**, 438 (1958).

[99] G. J. Moyar and D. H. Stone, Wear **144**, 117 (1991).

[100] M. R. Johnson, R. E. Welch, and K. S. Yeung, J. Eng. Ind. **99**, 18 (1977).

[101] P. Entel, R. Meyer, and K. Kadau, Philos. Mag. B **80**, 183 (2000).

[102] B.J. Ackerson and W. Loose, J. Chem. Phys. **101** (1994) 7211.

[103] A.Z. Patashinski, A.C. Mitus, and M.A. Ratner MA, Phys. Rep. **288**, 409 (1997).

[104] A.C. Mitus, F. Smolej, H. Hahn, and A.Z. Patashinski Europhys. Lett. **32**, 777 (1995).

[105] J. Barker, M. Hoare, and J. Finney, Nature **257**, 120 (1975).

[106] J.J. Erpenbeck, Phys. Rev. Lett. **52**, 1333 (1984).

[107] B.J. Ackerson, J.B. Hayter, N.A. Clark, and L. Cotter, J. Chem. Phys. **84**, 2344 (1986).

[108] B.J. Ackerson and P.N. Pusey, Phys. Rev. Lett. **61**, 1033 (1988).

[109] B.J. Ackerson, J. Rheol. **34**, 553 (1990).

[110] R.L. Hoffman, Trans. Sot. Rheol. **16**, 155 (1972); J. Coll. Interf. Sci. **46**, 491 (1974).

[111] H.M. Laun, R. Bung, S. Hess, W. Loose, O. Hess, K. Hahn, E. Hädicke, R. Hingmann. F. Schmidt, and P. Lindner. J. Rheol. **36**, 743 (1992).

[112] S. Ashdown, I. Markovic, R.H. Ottewill, P. Lindner, R.C. Oberthür, and A.R. Rennie, Langmuir **6**, 303 (1990).

[113] L.B. Chen, C.F. Zukoski, B.J. Ackerson, H.J.M. Hanley, G.C. Straty, J. Barker, and G.J. Glinka, Phys. Rev. Lett. **69**, 688 (1992).

[114] L. Euler, in: *Series prima. Opera mathematica*, H.-C. Im Hof, ed. (Birkhäuser, Basel, 1998).

[115] D. Tabor, *Gases, Liquids and Solids*, 3nd ed. (Cambridge University Press, Cambridge, 1993).

[116] P. A. Thompson and M. O. Robbins, Phys. Rev. A **41**, 6830 (1990).

[117] M. Kröger, Phys. Rep. **390**, 453 (2004).

[118] M. I. Baskes, Phys. Rev. Lett. **83**, 2592 (1999).

[119] O. B. Olurin, M. Arnold, C. Körner, and R. F. Singer, Mater. Sci. Eng. A, **328**, 334 (2002).

[120] J. Banhart, D. Bellmann, and H. Clemens, Acta Mater. **49**, 3409 (2001).

[121] J. Banhart, H. Stanzik, L. Helfen, and T.Baumbach, Appl. Phys. Lett. **78**, 1152 (2001).

[122] T. Miyoshi, I. Itoh, S. Akiyama, and A. Kitahara, in *Metal foams and porous metal structures*, edited by J. Banhart, M. F. Ashby, and N. A. Fleck, (MIT Press-Verlag, Bremen, 1999).

[123] C. Körner, M. Thies, M. Arnold, and R. Singer, in *Metal foams and porous metal structures*, edited by J. Banhart, M. F. Ashby, and N. A. Fleck, (MIT Press-Verlag, Bremen, 1999).

[124] J. M. D. MacElroy and K. Raghavan, J. Chem. Phys. **93**, 2068 (1990).

[125] K. Mecke and D. Stoyan, *Morphology of Condended Matter*, (Springer, Berlin, 2002).

[126] J. F. M. Lodge and D. M. Heyes, J. Chem. Phys. **109**, 7567 (1998).

[127] A. Isihara, *Statistical Physics*, (Academic Press, New York, 1971).

[128] M. Ertz, in *Proceedings of the 8th Mini Conference Vehicle System Dynamics, Identification and Anomalies (VSDIA)*, (Budapest, Hungary, 2002).

[129] B. Bandow, S. Hess, and M. Kröger, Physica A **337**, 443 (2004).

[130] N. B. Wilding and M. Schön, Phys. Rev. E **60**, 1081 (1999)

[131] M. Schön, J. H. Cushman, D. J. Diestler, and C. L. Rhykerd Jr., J. Chem. Phys. **88**, 1394 (1988); D. J. Diestler, M. Schön, A. W. Hertzner, and J. H. Cushman, J. Chem. Phys. **95**, 5432 (1991).

Publications from parts of this work

[1] I. Stanković, M. Kröger, and S. Hess,
Recognition and analysis of local structure in polycrystalline configurations,
Comput. Phys. Commun. **145**, 371 (2002).

[2] M. Kröger, I. Stanković, and S. Hess,
Towards multiscale modeling of metals via embedded particle computer simulations, Multiscale Model. Simul. **1**, 25 (2003).

[3] I. Stanković, M. Kröger, and S. Hess,
Thermo-mechanical and structural properties of a low degree polynomial embedded atom model metal, Proceedings of 5th General Conference of Balkan Physical Union (Vrnjačka Banja, 2003), 1301-1306.

[4] I. Stanković, S. Hess, and M. Kröger,
Structural changes and viscoplastic behavior of a generic embedded atom model metal in steady shear flow, Phys. Rev. E **69**, 021509 (2004).

[5] I. Stanković, S. Hess, and M. Kröger,
Microscopic structure, dynamics and wear at metal-metal interfaces in sliding contact, to appear in Phys. Rev. E (2004).

Curriculum vitae

Igor Stanković
Karadjordjeva 69,
11000 Belgrade,
Serbia and Montenegro

May 2004.

email: igorst@writeme.com

Date of birth:	02.09.1976
Place of birth:	Bijeljina, Bosnia and Herzegovina
Citizenships:	Serbia and Montenegro,
	Bosnia and Herzegovina

High school Education:

1990-1992	Grammar School Filip Višnjić, Bijeljina
1992-1994	Mathematical Grammar School, Belgrade
1991-1995	participated in programs of Petnica Science Center, institution of out-of-school education

Undergraduate Studies:

1994-1999	Studies at Department of Physical Electronics, Faculty of Electrical Engineering, Belgrade University (overall average grade: 9.1)
07/1999	the final diploma exam (Dipl.Ing. degree, grade: 10)
04/2003	Physics diploma, Technical University Berlin (Dipl.-Phys. degree, grade: very good)

Awards:

1993	October prize of Belgrade municipality for research project
1999	award Best Student at Department of Physical Electronics in 1999

Employment history:

12/1999-12/2001	assistant researcher, Institute of Theoretical Physics, TU Berlin, Special research area (DFG Sfb) 605, *Elementary friction processes*
01/2002-today	assistant researcher, Institute of Theoretical Physics, TU Berlin, Special research area (DFG Sfb) 448, *Mesoscopically structured composite systems*